
Improved understanding of wind turbine dynamics by enhancing the coupling of atmospheric simulations to an aeroelastic model

Von der Fakultät für Mathematik und Naturwissenschaften
der Carl von Ossietzky Universität Oldenburg
zur Erlangung des Grades und Titels eines
DOKTORS DER NATURWISSENSCHAFTEN (DR. RER. NAT.)
angenommene Dissertation

von

Sonja Steinbrück

geboren am 13.05.1986 in Bielefeld





Gutachterin: Prof. Dr. Kerstin Avila

Zweitgutachter: Prof. Dr. Richard Stevens

Tag der Disputation: 08.12.2025

Abstract

Optimizing the power generation of wind turbines requires considering various aspects, including turbine design, wind farm layout and more. An improved understanding of the interactions between wind turbines and the atmospheric boundary layer is an essential prerequisite for such optimizations. A central challenge in this context is the coupling of different spatial scales—ranging from wind fields spanning hundreds of kilometers to centimeter scales relevant to turbine dynamics. A promising approach to address this challenge is the coupling of multiple models to integrate these spatial scales effectively.

In the first part of this thesis, the PALM-FAST model chain—integrating the aeroelastic code FAST (Fatigue, Aerodynamics, Structures, and Turbulence) with the large-eddy simulation tool PALM (Parallelised Large-Eddy Simulation Model)—was further developed, enhanced and tested using the generic NREL 5 MW turbine and the eno114 3.5 MW turbine. The results show a high level of agreement with literature values and measurement data. Additionally, the developed coupling offers significant time savings compared to conventional actuator line models (ALM)—up to 89% in one tested case—while still providing detailed turbine data. To reduce errors caused by the necessary distribution of forces across the numerical grid in atmospheric simulations, two coupling variants were developed within this thesis.

In the first variant of the PALM-FAST coupling, the issue was addressed by combining wind speeds from the free inflow with an induction model, which is implemented in FAST. This method proved to be efficient and practical for standardized scenarios. The second variant includes a correction of wind speeds directly at the rotor blade. This second advanced variant offers broader applicability, particularly in more complex scenarios. A model-to-model comparison of a wind turbine operating in the wake of another turbine demonstrated very good results, highlighting the accuracy and applicability of the coupling developed in this work.

One specific application investigated in this thesis is the influence of coastal conditions on the downstream offshore flow. Since wind farms are often installed near coastlines, the flow conditions over coastal regions significantly impact downstream wind conditions and consequently, can influence wind turbines and wind farms situated in the affected region. As part of this thesis, idealized coastal transitions were analyzed using large-eddy simulations (LES) to study the resulting flow changes. The findings reveal that surface conditions, such as roughness and temperature, can create significant lateral gradients in the wind field that persist over several kilometers. In particular, a combination of warm, smooth surfaces and cool, rough surfaces leads to pronounced flow heterogeneities that strongly influence boundary layer dynamics. These heterogeneities generate circulations that vertically transport flow properties, thereby impacting turbine performance and loads.

The coupling of PALM with FAST, developed in this thesis, enables a detailed investigation of these effects. Turbine data, such as power generation and blade loads, are analyzed in turbulence-

resolved flow fields, providing valuable insights into turbine behavior downstream of heterogeneities. The results of this work further demonstrate that variations in turbulence intensity (TI) and vertical wind velocity, even over small spatial scales, can have significant effects on turbine performance and loads. The PALM-FAST model presented here thus provides a powerful foundation for optimizing wind farm design and operation, particularly in complex and heterogeneous flow fields.

Kurzfassung

Die Optimierung der Energieerzeugung von Windturbinen erfordert die Berücksichtigung verschiedener Aspekte, darunter das Design der Turbine, die Anordnung von Windparks und mehr. Ein verbessertes Verständnis der Wechselwirkungen zwischen Windturbinen und der atmosphärischen Grenzschicht ist eine wesentliche Voraussetzung für solche Optimierungen. Dabei stellt die Herausforderung der Kopplung unterschiedlicher Längenskalen – von Windfeldern, die Hunderte von Kilometern umfassen, bis hin zu Zentimeterbereichen, die für die Dynamik der Turbinen relevant sind – eine zentrale Fragestellung dar. Ein vielversprechender Ansatz zur Bewältigung dieser Herausforderung ist die Kopplung mehrerer Modelle, um die Längenskalen zu kombinieren.

Im ersten Teil dieser Arbeit wurde die PALM-FAST-Modellkette – welche den aeroelastischen Code FAST (Fatigue, Aerodynamics, Structures, and Turbulence) mit dem Large-Eddy-Simulationsmodell PALM (Parallelised Large-Eddy Simulation Model) integriert – weiterentwickelt, verbessert und mit der generischen NREL 5 MW-Turbine sowie der eno114 3,5 MW-Turbine getestet. Die Ergebnisse zeigen eine hohe Übereinstimmung mit Literaturwerten und Messdaten. Dabei bietet die entwickelte Kopplung im Vergleich zu herkömmlichen Aktuatorlinienmodellen (ALM) eine enorme Zeitersparnis (89% in einem getesteten Fall), ohne auf detaillierte Turbinendaten zu verzichten. Um Fehler zu reduzieren, die durch die notwendige Verteilung der Kräfte auf das numerische Gitter in atmosphärischen Simulationen entstehen, wurden im Rahmen dieser Thesis zwei Varianten der Kopplung entwickelt.

In der ersten Variante der PALM-FAST-Kopplung wurde das Problem durch die Kombination von Windgeschwindigkeiten aus der freien Einströmung mit einem Induktionsmodell umgangen, das in FAST implementiert ist. Diese Methode erwies sich als effizient und praktikabel für standardisierte Szenarien. Die zweite Variante der Kopplung umfasst hingegen eine Korrektur der Windgeschwindigkeiten direkt am Rotorblatt. Diese zweite, weiterentwickelte Variante bietet breitere Anwendungsmöglichkeiten, insbesondere in komplexeren Szenarien. Ein Modell-zu-Modell-Vergleich einer Windturbine im Nachlauf einer weiteren Windturbine zeigte im Rahmen dieser Arbeit sehr gute Ergebnisse und unterstreicht die Genauigkeit und Anwendbarkeit der entwickelten Kopplung.

Ein spezifischer Anwendungsfall, der in dieser Arbeit untersucht wird, ist der Einfluss von Küstenbedingungen auf die stromabwärts gelegene Offshore-Strömung. Da Windparks oft in der Nähe von Küstenlinien errichtet werden, beeinflussen die Strömungsbedingungen über den Küstengebieten die Windverhältnisse stromabwärts und können folglich Windturbinen und Windparks in der betroffenen Region beeinflussen. Im Rahmen dieser Thesis werden durch Large-Eddy-Simulationen (LES) idealisierte Küstenübergänge untersucht, um die resultierenden Strömungsänderungen zu analysieren. Die Ergebnisse zeigen, dass Oberflächenbedingungen wie Rauigkeit und Temperatur signifikante laterale Gradienten im Windfeld erzeugen können, die über Distanzen von mehreren Kilometern hinweg bestehen bleiben. Insbesondere eine Kombination aus warmen, glatten und kühlen, rauen

Oberflächen führt zu ausgeprägten Strömungsheterogenitäten, die die Dynamik der Grenzschicht stark beeinflussen. Diese Heterogenitäten verursachen Zirkulationen, die Strömungseigenschaften vertikal transportieren und dadurch die Turbinenleistung und -lasten beeinflussen.

Durch die in dieser Thesis entwickelte Kopplung von PALM mit FAST können diese Effekte detailliert untersucht werden. Turbinendaten wie Energieerzeugung und Blattlasten werden in turbulenz aufgelösten Strömungen analysiert, was wertvolle Einblicke in das Verhalten von Turbinen stromabwärts von Heterogenitäten liefert. Die Ergebnisse dieser Arbeit zeigen zudem, dass Variationen in der Turbulenzintensität (TI) und der vertikalen Windgeschwindigkeit selbst auf kleinem Raum erhebliche Auswirkungen auf die Leistung und Lasten der Turbinen haben können. Das hier vorgestellte gekoppelte PALM-FAST Modell bietet somit eine leistungsstarke Grundlage für die Optimierung des Designs und der Steuerung von Windparks, insbesondere in komplexen und heterogenen Strömungsfeldern.

Contents

List of Figures	ix
List of Tables	xv
List of Abbreviations and Symbols	xvii
1 Introduction	1
1.1 Impact of atmospheric flow conditions on wind turbines	5
1.2 Wind turbine parametrization - Actuator sector models for wind turbines	6
1.3 Effect of upstream heterogenities on the downstream offshore flow	10
1.4 Objectives and structure of the thesis	13
2 Foundational methods and models	15
2.1 PALM	15
2.1.1 Governing equations and numerical methods in PALM	15
2.1.2 Wind turbine parameterizations	20
2.2 FAST v8	25
2.2.1 Blade element momentum theory	26
2.3 Near wake correction	30
3 Newly developed method: PALM-FAST coupling	35
4 Validation of a coupled atmospheric–aeroelastic model system for wind turbine power and load calculations	37
4.1 Methodology: the PALM–FAST coupling	38
4.2 Validation	40
4.2.1 Evaluation of the coupling on the basis of the generic NREL 5 MW turbine	40
4.2.2 Validation of the coupling with the eno114 3.5 MW turbine	43
4.3 Conclusion	58
A.1 Blade elements in the NREL 5 MW turbine laminar case	61
A.2 Spectra of the loads for the neutral case	62
A.3 Wind profile comparison for the stable case	63
5 Improved coupling between an atmospheric LES and an aeroelastic code for the simulation of wind turbines in turbulent flows	65
5.1 Methodology: Extension of the PALM-FAST coupling to include NWC	66

5.2	Investigation of the NWC method in ALM and ASM	70
5.2.1	Model verification in laminar flow	70
5.2.2	Model verification in turbulent flow	73
5.2.3	Verification of the ASM-SL NWC in the wake of another turbine	74
5.3	Validation with measurement data of a single eno114 3.5 MW turbine	76
5.4	Conclusions	78
A.1	Investigation of the effect of the blade resolution of the NREL 5 MW turbine	81
A.2	Power output of FAST depending on the blade resolution of the NREL 5 MW turbine	84
6	Structures in flows downstream of surface heterogeneities and their effect on wind turbines	85
6.1	Numerical Setup and Methodology for Turbine Calculations	85
6.1.1	LES Model PALM General Setup	86
6.1.2	Turbine simulations – PALM-FAST coupling	88
6.2	Downstream Effects of Systematic Heterogeneity Variations	89
6.2.1	Results	89
6.2.2	Closer look at 128wc and 640wc	97
6.3	Turbine power output and loads in flows downstream of inhomogeneous surfaces	102
6.3.1	Description of the simulations performed	102
6.3.2	Results	107
6.4	Discussion	109
6.5	Conclusions	110
A.1	Stripes downstream of inhomogeneous surfaces - additional results	113
A.1.1	Statistics of wind speed along y with distance to coastline	114
A.2	Closer look at 128wc and 640wc - additional results	115
A.3	Turbine loads spectra	116
7	Conclusions and Outlook	117
7.1	Conclusions	117
7.2	Outlook	119
	Bibliography	121
	Publication list	131
	Acknowledgements	133
	Curriculum Vitae	135

List of Figures

1.1	Expected Development of Offshore Wind Energy Capacity in Germany. Source: WindGuard [2025a]	2
1.2	Schematic representing the scales and their corresponding temporal and spatial resolution.	3
1.3	Various approaches to represent the effects of wind turbines in numerical simulations: (a) ADM-R, (b) ALM and (c) ASM.	6
2.1	Schematic of the ADM-R wind turbine parameterization. The rotor disc is divided into ring segments, with each segment calculating the respective shares of the lift and drag forces individually, as shown by the arrows.	21
2.2	Schematic of the ALM wind turbine parameterization. The rotor blades are divided into segments, for each segment the respective lift and drag forces are being calculated individually, as shown by the arrows.	22
2.3	Schematic of the forces, velocities and angles at a blade element of a wind turbine, based on Troldborg [2008]	23
2.4	Schematic of the ASM wind turbine parameterization. The sector represents the area the rotor blades swipe within the LES time step. Different approaches for the calculation of the forces is possible. This schematic depicts one method, where the sector is subdivided into lines, allowing for the individual calculation of lift and drag forces for each segment, as indicated by the arrows.	25
2.5	Schematic of the annular ring segments at distance r to the nacelle and width dr , based on Moriarty and Hansen [2005]	26
2.6	Flow chart of the iterative BEM process as implemented in AeroDyn.	30
2.7	Schematic of the trailing vortices at a planar wing, based on Dag [2017] . N denotes the total number of actuator line points and Γ the strength of the vortices.	32
2.8	Flow chart of the iterative process of the NWC as described by Meyer Forsting et al. [2019]	34
3.1	Overview of the PALM-FAST coupling methods. The options for wind speed sampling and corrections are written in color, blue representing the ASM SWIRL option and green the ASM NWC.	36
4.1	Schematic of the operation mode of the PALM-FAST ASM coupling. (a) Schematic of the PALM and FAST time stepping. (b) Schematic of one circle segment of the ASM. The values of the bold central line are used for the projection of the forces into the flow. Here, y and z denote the rotor plane and x the streamwise direction.	39

4.2	Comparison of different simulation methods for the generator power of the 5 MW NREL turbine in a laminar flow with 8 m s^{-1} wind speed.	43
4.3	Comparison of different simulation methods for the generator power of the 5 MW NREL turbine in a turbulent flow at about 7.4 m s^{-1} wind speed at hub height. . . .	44
4.4	Comparison of different simulation methods for the generator power of the eno114 3.5 MW turbine in a laminar case with a wind speed of 8 m s^{-1} , normalised by the respective value of the eno114 3.5 MW energy power curve at 8 m s^{-1}	44
4.5	Schematic of the measurement site in Brusow. The remaining wind directions in the measurement data, after filtering, are indicated in red; D is the turbine diameter, here $D = 114.9 \text{ m}$	45
4.6	Roughness length distribution for varying wind directions for the measurement period. Two methods of averaging the roughness length values gained by Eq. (4.2) were used; here z_0 denotes the roughness length determined from 30 min eddy-covariance data, and j denotes the 15° wind direction bins: (1) averaging $z_{0,j}$ per 15° bins (blue) and (2) averaging using $\ln z_{0,j} = \frac{\langle u_* \ln(z_{0,j}) \rangle}{\langle u_* \rangle}$ per 15° bins (red), where the angle brackets $\langle \dots \rangle$ denote the average over values within the 15° bins.	46
4.7	Power data determined from the measurement data for May/June 2017, normalised by the corresponding power of the eno114 3.5 MW power curve determined by FAST in laminar conditions, for different stabilities (determined from eddy-covariance data).	47
4.8	Standard deviation for 10 min intervals of the measured turbine power output, calculated according to $\sigma_{P_{10}} = \sqrt{\frac{1}{N_{\text{meas}}-1} \sum_{k=1}^{N_{\text{meas}}} P(t_k) - P_{10} ^2}$, where $P(t_k)$ denotes the power data measured in 50 Hz, P_{10} the 10 min average and N_{meas} the number of measurements within the 10 min interval, normalised by the maximum 10 min standard deviation of the power, for May/June 2017, and sorted and averaged according to stability (determined from eddy-covariance data) and wind speed.	48
4.9	Turbulence intensity $\text{TI}_{92 \text{ m}}$ of the measurement data (green) in comparison to the resulting $\text{TI}_{92 \text{ m}}$ of the precursor runs sorted in neutral and stable (red – neutral; blue – stable).	50
4.10	Shear of the measurement data (green) in comparison to the resulting shear of the precursor runs sorted in neutral and stable (red – neutral; blue – stable).	50
4.11	(a) Power curve, normalised by maximum 10 min power, determined from measurement data including standard deviation in comparison to the results of the simulation (marked by \times). (b) Enlargement of panel (a) . The standard deviation is plotted again in Fig. 4.12.	51
4.12	Normalised standard deviation of the power with respect to the wind speed determined from measurement data in comparison to the simulation results (\times). Sorted into stability by eddy-covariance data, TI and shear determined from the met mast data.	52
4.13	Standard deviation of the power with respect to the TI determined from measurement data (green – all wind speeds; blue and red asterisks – stable and neutral measurements at wind speeds of $8\text{--}9 \text{ m s}^{-1}$) in comparison to the simulation results (\times).	52

4.14	Blade root bending moment (a) out of plane M_y^b and (b) in plane M_x^b with respect to wind speed in comparison to the simulation results; averaged 10 min values were sorted by stability, averaged according to wind speed and normalised with the maximum measured moment.	53
4.15	Spectrum of the blade root bending moment (a) out of plane M_y^b and (b) in plane M_x^b in comparison to the simulation results (stable). The data are normalised by the maximum value of the blade root bending moments.	54
4.16	Spectrum of the tower top bending moment in (a) the fore-to-aft direction M_y^{tt} and (b) the side-to-side direction M_x^{tt} ; comparison of the measurement data to the simulation results (stable). The data are normalised by the maximum value of the tower top bending moments, and the frequency is normalised by the rotor speed.	55
4.17	Spectrum of the tower moments: (a) the tower base bending in the fore-to-aft direction M_y^{tb} , (b) the tower base bending in the side-to-side direction M_x^{tb} and (c) the tower top torsion M_z^{tt} ; comparison of the measurement data to the simulation results (stable). The data are normalised by the maximum value of the tower base and tower top torsion moment, and the frequency is normalised by the rotor speed.	56
4.18	Comparison of the (a) blade root bending moments out of plane M_y^b and (b) tower top fore-aft bending moment M_y^{tt} for the stable and neutral simulation. The data are normalised by the maximum value of the blade root bending and tower top bending moments, and the frequency is normalised by the rotor speed.	56
4.19	Power output normalised by the maximum measured power, plotted with respect to the rotor speed, and normalised with the maximum measured rotor speed with an added offset for the measurement data in comparison to the simulation data.	57
4.20	Relation between the rotor speed Ω , normalised with the maximum measured rotor speed with an added offset, with respect to the wind speed determined using the measurement data in comparison to the simulation data (\times).	58
21	Dynamic pressure (a) and angle of attack (b) along the blade nodes in the laminar case of the NREL 5 MW turbine.	61
22	Lift (a) and drag (b) coefficient along the blade nodes in the laminar case of the NREL 5 MW turbine.	61
23	Spectrum of the blade root bending moment (a) out of plane M_y^b and (b) in plane M_x^b in comparison to the simulation results (neutral). The data are normalised by the maximum value of the blade root bending moments, and the frequency is normalised by the rotor speed.	62
24	Spectrum of the tower top bending moment in (a) the fore-to-aft direction M_y^{tt} and (b) the side-to-side direction M_x^{tt} ; comparison of the measurement data to the simulation results (neutral). The data are normalised by the maximum value of the tower base bending moments, and the frequency is normalised by the rotor speed.	62
25	Spectrum of the tower moments: (a) the tower base bending moment in the fore-to-aft direction M_y^{tb} , (b) the tower base bending moment in the side-to-side direction M_x^{tb} and (c) the tower top torsion moment M_z^{tt} ; comparison of the measurement data to the simulation results (neutral). The data are normalised by the maximum value of the tower top torsion moment, and the frequency is normalised by the rotor speed.	63

26	Wind profiles, calculated by the shear and wind speed, of the measurement interval and the simulation data used in the comparison of the loads for the stable case. The black lines indicate the rotor area, and the dashed line indicates the hub height. . . .	64
5.1	Schematic of the operation mode of the proposed coupling ASM-SL, the red fields show the points of change in comparison to ASM SWIRL, see also table 5.1 for explanation of the methods.	68
5.2	Schematic of the two working principles of the described sector methods. (a) ASM-CL: Wind speeds U are taken at every blade position within the frozen wind field. The varying colours of $U_{n,m}$ represent different wind speeds, with reddish colours indicating a stronger influence from the previous time step and blue indicating a greater distance and therefore less influence from the previous time step. The previous PALM time step (= sector) is indicated in light red. (b) ASM-SL: Wind speeds U_n are taken at the first blade position with respect to the previous sector (light red) and used for all blade positions in the current sector.	69
5.3	Comparison of ALM, ALM with NWC and ASM with NWC for the power output of the 5 MW NREL turbine in laminar conditions with 8 ms^{-1}	71
5.4	Comparison of (a) the angle of attack (b) the normal force along the blade normalized by the blade element width (c) the tangential force along the blade normalized by the blade element width and (d) the lift coefficient, averaged from 200 s until the end of the simulations, for an ALM without any correction, FAST, ALM with NWC and the ASM-SL with NWC.	72
5.5	Wind speed difference between ASM-SL with and without NWC, averaged from 200 s until the end of the simulations.	73
5.6	Comparison of different model variations for the power output of the 5 MW NREL turbine in turbulent conditions.	74
5.7	Comparison of power output for a wake situation with (a) a distance of $4D$ and (b) a distance of $8D$, the solid lines show the result of the upstream turbine T1, the dashed lines the downstream turbine T2. Additionally to the results of the sector models, results of a FAST simulation for T2 using an inflow field generated from the PALM wind field is shown in black.	75
5.8	Comparison of the statistics of the normalized power time series of ASM SWIRL, ASM-SL NWC and PALM wnd for the turbine spacing of (a) $4D$ and (b) $8D$. Shown is the median and spread of the values of the above mentioned simulations.	76
5.9	Extract of the power curve, normalised by the maximum 10 min power, determined from the measurement data, divided into stable (st) and neutral (ne) conditions. Comparison of the measurement data, the simulation data of ASM SWIRL and the new version ASM-SL NWC. The measurement and ASM SWIRL data are sourced from Krüger et al. [2022].	77

5.10	Spectrum of (a) the blade root bending moment out-of-plane M_y^b and (b) the blade root bending moment in-plane M_x^b . Comparison of measurement data and simulations of the models ASM SWIRL and ASM-SL NWC. The data are normalised by the maximum value of the blade root bending moment. The frequency is normalised by the rotor speed. The measurement and ASM SWIRL data are sourced from Krüger et al. [2022]	78
11	Comparison of (a) the angle of attack (b) the normal force along the blade normalized by the blade element width (c) the tangential force along the blade normalized by the blade element width and (d) the lift coefficient, averaged from 200s until the end of the simulations, for FAST and the ALM NWC with the blade resolutions of 17, 19 and 62 nodes.	82
12	Comparison of (a) the dynamic pressure and (b) the drag coefficient, averaged from 200s until the end of the simulations, for ALM, FAST and the ALM NWC with the blade resolutions of 17, 19 and 62 nodes, as well as ASM-SL NWC.	82
13	Power time series of the FAST stand-alone simulations with steady wind inflow conditions for the blade resolutions of 62, 17 and 19 nodes per blade.	84
6.1	Setup of the model domain having idealized surface heterogeneities. The inflow area A0 has the roughness length $z_0 = 0.1$ m, the area behind the heterogeneity patches A3 has the roughness length $z_0 = 0.0002$ m. The roughness length and surface temperature vary in the areas A1 and A2.	87
6.2	1-hour averaged wind speed and wind speed components v and w at a height of $z = 145$ m, perpendicular to the main flow direction, taken at various positions behind the coastline for the cases 128b and 640b, containing roughness changes but no temperature gradients.	92
6.3	1-hour averaged wind speed and wind speed components v and w at a height of $z = 145$ m, perpendicular to the main flow direction, taken at various positions behind the coastline for the cases 32wc, 128wc and 640wc, containing roughness changes and temperature changes.	93
6.4	1-hour averaged wind speed and wind speed components v and w at a height of $z = 145$ m, perpendicular to the main flow direction, taken at various positions behind the coastline for the cases 128cw and 640cw, containing roughness changes and temperature changes.	94
6.5	1-hour averaged wind speed and wind speed components v and w at a height of $z = 145$ m, perpendicular to the main flow direction, taken at various positions behind the coastline for the cases 640b, 640wc, 640cw and 640wcT, containing roughness changes and temperature changes. For better visibility the cases 640b and 640wcT are omitted in the plot of the vertical wind speed component w	95
6.6	Cross-section in the yz -plane, in 10 km distance to the coastline, illustrating the horizontal wind speed component u in color, with vectors representing the vertical component w . Data is averaged over a 1-hour period.	96

6.7	Cross-section in the yz -plane, in 10 km distance to the coastline, illustrating the horizontal wind speed component u in color, with streamlines representing the components v and w . Data is averaged over a 1-hour period and the inflow components of v and w are subtracted for each height level. (a) for the case 128wc and (b) for 640wc.	98
6.8	Cross-section in the yz -plane, in 10 km distance to the coastline, illustrating the turbulence intensity TI. Data is averaged over a 1-hour period. (a) for the case 128wc and (b) for 640wc.	99
6.9	Cross-section in the yz -plane in streamwise direction for the cases (a) 128wc and (b) 640wc at subsequent x -positions downstream of the coastline, illustrating the horizontal wind speed component u in color, with vectors representing the vertical component w . Data is averaged over a 1-hour period.	100
6.10	Cross-section in the yz -plane in streamwise direction for the cases (a) 128wc and (b) 640wc at subsequent x -positions downstream of the coastline, illustrating the potential temperature θ in color, with vectors representing the horizontal component v . Data is averaged over a 1-hour period and the inflow v component is subtracted for each height level.	101
6.11	Cross-section in the yz -plane for the cases (a) 128wc5K and (b) 640wc5K at subsequent x -positions downstream of the coastline, illustrating the horizontal wind speed component u in color, with vectors representing the vertical component w . Data is averaged over a 1-hour period.	104
6.12	Average wind speed at a height of $z = 145$ m, perpendicular to the main flow direction, taken at various positions behind the coastline for the cases (a) 128wc and 128wc5K and (b) 640wc and 640wc5K. The data are averaged over a duration of 1 h.	105
6.13	Cross-section in the xy -plane for the case 640wc and 640wc5K. Data is averaged over a 1-hour period.	106
6.14	Wind speed U and vertical wind speed component w along y at a distance of 20 km downstream of the coastline at 145 m height for the cases (a) 128wc5K and (b) 640wc5K. The dashed vertical lines show the proposed turbine positions.	106
6.15	Power time series of turbines at y positions (a) $y = 2400$ m, $y = 5900$ m and $y = 8900$ m in the case 128wc5K and (b) $y = 3150$ m and $y = 8700$ m in the case 640wc5K.	108
16	Positions of the maxima in wind speed at 145 m height along y -direction and their lateral movement with distance to the coastline.	113
17	TI along y at hubheight 145 m, in 10 km distance to the coastline. Data is averaged over a 1-hour period. (a) for the case 128wc and (b) for 640wc.	115
18	Spectra of the blade root in-plane M_x and out-of-plane M_y bending moments in the case 128wc5K.	116
19	Spectra of the blade root in-plane M_x and out-of-plane M_y bending moments in the case 640wc5K.	116

List of Tables

4.1	Overview of the turbine models that were used in the comparisons. The new enhanced coupling method is ASM, the respective time steps in PALM and FAST are denoted as Δt_P and Δt_F respectively, and the inflow wind speed is denoted as U . The coupled model that is the focus of this paper is highlighted in bold.	41
4.2	Classification of atmospheric stability according to Obukhov length L , based on Peña et al. [2008]. The distribution of the atmospheric stability in the measured data can be seen in Figs. 4.9 and 4.10.	47
4.3	Set-up of the precursor simulations: size of the model domain in the streamwise x , spanwise y and vertical z direction; grid size Δ ; cooling rate $\Delta\Theta/\Delta t$; geostrophic wind speed components at the surface in the x and y direction u_g and v_g ; and total simulated time t_{end}	48
4.4	Resulting flow parameters after reaching a stationary state in the precursor simulations, averaged over 3600 s: the magnitude of the wind speed at hub height averaged over the model domain $U_{92\text{ m}}$, turbulence intensity calculated at one position in 92 m height $\text{TI}_{92\text{ m}}$, shear parameter α (based on the power law $u_2 = u_1 \left(\frac{z_2}{z_1}\right)^\alpha$ for the relation of wind speeds at different heights), Obukhov length L in a height of 2.3 m and boundary layer height z_i	49
4.5	Turbine positions along the y axis (keeping the same x position), with the y direction spanning from 0 to 2595 m for the NBL and from 0 to 2304 m for the SBL, in the model domain of the main run; additionally, the local wind speed $U_{92\text{ m}}$ and turbulence intensity $\text{TI}_{92\text{ m}}$ at hub height at these y coordinates, taken $2.5D$ in front of the turbine averaged over the last 10 min of a 650 s simulation.	49
4.6	Summary of the parameters of the measurement interval data used for the spectra of the blade and turbine loads: wind speed at hub height $U_{92\text{ m}}$, turbulence intensity at hub height $\text{TI}_{92\text{ m}}$, shear parameter α and the length of the available time interval t_{interval}	54
4.7	Comparison of the equivalent load range Δ_{eq} of the simulation results (10 min interval), according to Eq. (4.3) with $m = 10$ for blade loads and $m = 4$ for tower loads.	58
5.1	Overview of the different models and their key differences.	67
5.2	Setup of the precursor simulations: Size of the model domain in streamwise x , spanwise y and vertical z direction, grid size Δ , cooling rate $\Delta\Theta/\Delta t$, geostrophic wind speed components at the surface in x - and y -direction u_g , v_g and total simulated time t_{end}	76

5.3	Resulting flow parameters after reaching a stationary state in the precursor simulations, averaged over 3600 s: The magnitude of the wind speed at hub height averaged over the model domain U_{92m} , turbulence intensity calculated at one position in 92 m height TI_{92m} , shear parameter α (based on the power law $u_2 = u_1 \left(\frac{z_2}{z_1}\right)^\alpha$ for the relation of wind speeds at different heights), Obukhov length L in a height of 2.3 m (height is chosen for comparison to the eddy-covariance data at the measurement site) and boundary layer height z_i	77
4	Summary of the blade resolutions used in Meyer Forsting et al. [2019], denoted with M-F, and here, as well as their corresponding power output for a laminar case of 8 ms^{-1}	83
6.1	Setup of the simulations: Size of the model domain in streamwise x , spanwise y and vertical z direction, grid size Δ , geostrophic wind speed components at the surface in x - and y -direction u_g, v_g and total simulated time t_{end} . All simulations were performed at latitude setting 54.5°	87
6.2	Summary of the performed simulations. The abbreviation for each run consists of the width of the patches in grid cells and further distinguishing letters (b: base, c: cold, w: warm, st: stable, us: unstable, T: temperature, l: long).	88
6.3	Mean \bar{P} and standard deviation σP of the power output, as well as in-plane M_x and out-of-plane M_y moments at the blade root, at two turbine positions. Averaged over 900 s, starting from simulation time 200 s.	108
6.4	Equivalent load ranges Δ_{eq} , calculated for the time series of 900 s, starting from simulation time 200 s, for the in-plane M_x and out-of-plane M_y moments at the blade root.	109
5	Mean wind speed at 145 m height for distances 0km, 5km, and 10km, averaged in y -direction at different distances to the coastline. Additionally, the positive and negative deviation from the mean value are shown in %. The maximum values per distance to coastline are marked in bold.	114

List of Abbreviations and Symbols

Abbreviations

ABL	Atmospheric boundary layer
ADM	Actuator Disk Model
ADM-R	Actuator Disk Model with rotation
AeroDyn	Aerodynamics Module of FAST
AFM	Actuator Farm Model
ALM	Actuator Line Model
ASM	Actuator Sector Model
ASM SWIRL	Actuator Sector Model with SWIRL induction model
ASM-CL	Actuator Sector Model - continuous lines
ASM-SL	Actuator Sector Model - single line
BEM	Blade Element Momentum (Theory)
CFD	Computational Fluid Dynamics
CFL	Courant-Friedrichs-Levy
DEL	Damage Equivalent Loads
DNS	Direct Numerical Simulation
FAST	Fatigue, Aerodynamics, Structures and Turbulence
FFT	Fast Fourier Transform
FSI	Fluid Structure Interaction
IEA	International Energy Agency
LES	Large-eddy simulation
LLT	Lifting Line Theory
MOST	Monin–Obukhov similarity theory
MR	Main Run
NBL	Neutral Boundary Layer
NREL	National Renewable Energy Laboratory
NWC	Near Wake Correction
PALM	PARallelised Large-eddy simulation Model
PR	Precursor Run
PSD	Power Spectral Density
RANS	Reynolds-averaged Navier–Stokes
RWT	Reference Wind Turbine

SBL	Stable Boundary Layer
SGS	Subgrid-scale
SWIRL	SWIRL induction model of FAST
TI	Turbulence Intensity
TKE	Turbulent kinetic energy
TSR	Tip Speed Ratio
TURBSIM	Turbulence Simulator (tool for generating wind fields)

Mathematical Symbols

α	Angle of attack
α	Wind shear parameter
\bar{U}	Mean wind speed
χ	Wake skew angle
$\Delta \tilde{u}_{s,v}^n$	Biot-Savart velocity component
Δr	Span-wise length of a rotor blade element
ΔS	Loading amplitude (used for DEL calculation)
ΔT	Temperature difference
Δt	Time step
Δt_F	Time step in FAST
Δt_P	Time step in PALM
Δ	Grid size
$\Delta+$	Positive deviation from the mean wind speed
$\Delta-$	Negative deviation from the mean wind speed
Δ_{eq}	Equivalent load range
δ_{ij}	Kronecker-Delta
ϵ_{ijk}	Levi-Civita symbol
η	Regularization function applied at grid nodes
Γ	Vorticity of trailing vortices
γ	Pitch angle
κ	von Kármán constant
\mathcal{T}_{aero}	Aerodynamic thrust
\mathcal{T}_{total}	Total thrust
Ω	Rotor speed
\bar{u}_i	Resolved component of velocity
ϕ^*	Helix angle for vortex shedding
Φ_m	Similarity function for momentum
π^*	Resolved-scale pressure deviation
ρ	Air density
σ'	Local solidity
$\sigma_{P_{10,max}}$	Maximum standard deviation of 10-minute power
$\sigma_{P_{10}}$	Standard deviation of power over a 10-minute interval

LIST OF ABBREVIATIONS AND SYMBOLS

τ_{ij}	Stress tensor
θ	Potential Temperature
ε	Smearing length scale, related to the grid size ($\varepsilon = 2\Delta$)
φ	Flow angle
a	Axial induction factor
A_{disk}	Rotor disk area
A_{seg}	Reference area of rotor ring segment
$a_{\{X,Y\}}, b_{\{X,Y\}}$	Coefficients for vortex calculations
c	Chord length of blade section
c_D, c_d	Drag coefficient
c_L, c_l	Lift coefficient
c_m	Model constant for SGS closure
c_T	Thrust coefficient of the wind turbine
C_{CFL}	Courant-Friedrichs-Lewy factor
D	Rotor Diameter
e	Subgrid-scale turbulent kinetic energy
F	Tip- and hub-loss correction factor
F_{Θ}	Tangential force on blade element
f_{ε}	Smearing factor
f_c	Coriolis parameter
F_N	Axial force on blade element
$F_{D,\beta}$	Drag force on rotor ring segment
$F_{L,\beta}$	Lift force on rotor ring segment
g	Gravitational acceleration vector
k	von Kármán constant
K_m	Eddy-transfer coefficient of momentum
L	Obukhov length
l	Mixing length
L_{patch}	Patch width
m	Wöhler exponent (used for DEL calculation)
M_x	In-Plane Blade Root Bending Moment
M_y	Out-of-plane Blade Root Bending Moment
N	Total number of cycles (used for DEL calculation)
N_{ref}	Reference number of cycles (used for DEL calculation)
p	Atmospheric pressure
p^*	Pressure deviation
P_{10}	10-minute average of measured power data
P_{aero}	Aerodynamic power
P_{total}	Total power
q	Dynamic pressure
q_v	Water vapor mixing ratio

LIST OF ABBREVIATIONS AND SYMBOLS

r	Distance between grid node and blade element
s	Passive scalar
T	Air temperature
t_{FAST}	Simulation time in FAST
t_{PALM}	Simulation time in PALM
t_{end}	Total simulation time
T_{surf}	Surface Temperature
TI_{92m}	Turbulence intensity at hub height (92 m)
U	Wind speed
u	Horizontal Wind Speed Component (along x -axis)
u_*	Friction velocity
u_{ec}	Wind speed at eddy-covariance station
U_d	Wind speed at the rotor disk
u_g	Geostrophic wind speed component in x -direction
u'_i	Fluctuating component of velocity
U_{92m}	Wind speed at hub height (92 m)
U_{ref}	Free inflow wind speed at the center of the rotor disk
v	Horizontal Wind Speed Component (along y -axis)
v_g	Geostrophic wind speed component in y -direction
V_{rel}	Relative velocity at rotor blade
w	Vertical Wind Speed Component (along z -axis)
x	Streamwise (main flow) direction
x_i	Spatial coordinates
$X_{s,v}^n, Y_{s,v}^n$	Indicial functions for vortex shedding
y	Spanwise (perpendicular to x) direction
z	Vertical (height) direction
z_0	Roughness Length
z_{ec}	Height of eddy-covariance station
z_i	Boundary Layer Height
$z_{0,h}$	Roughness length for heat

Chapter 1

Introduction

Wind energy has emerged as a crucial pillar in the global transition towards sustainable and renewable energy sources, playing a vital role in reducing carbon emissions and combating climate change. In Germany, the Energiewende initiative exemplifies this commitment, aiming to significantly increase the share of renewable energy, particularly wind power, in the national energy mix while fostering economic growth and environmental protection. The intention is to expand the offshore wind energy capacity to a total of 30 GW by 2030, see Fig. 1.1 and the onshore wind energy capacity to a total of 115 GW. As of the end of 2024, the installed wind energy capacity in Germany stands at 63.6 GW on land and 9.2 GW offshore [WindGuard, 2025a,b]. Effective planning is essential to achieve the targets of the Energiewende, and numerical simulations play a critical role in this process. Accurate predictions of power output, loads, wake effects from wind turbines and turbine interactions within wind farms are vital for optimizing wind turbine design and site selection.

Power output predictions are essential for assessing the energy generation potential of a wind farm, helping developers estimate the financial viability and return on investment. Load predictions are crucial for ensuring that the turbine structures can withstand the various forces they will encounter during operation, thus maintaining safety and longevity. Furthermore, understanding wake effects—where the wind speed and turbulence are altered downstream of turbines—allows for better placement strategies to minimize energy losses and optimize the performance of neighboring turbines. Finally, analyzing turbine interactions is important for understanding how multiple turbines will affect each other’s performance, which is critical for maximizing overall energy capture and ensuring efficient operation of the wind farm. Numerical simulations often offer a more cost-effective approach for evaluating specific scenarios, turbine or wind farm designs and site conditions compared to traditional field campaigns, while ensuring reproducibility.

Numerical simulation tools typically specialize in a specific area, such as mesoscale weather simulations, microscale atmospheric flow modeling, or high-resolution simulations of individual wind turbines. This specialization is essential because not every tool can accurately model all length scales, given the differing complexities and dynamics involved. Figure 1.2 presents a schematic diagram illustrating the spatial and temporal resolutions covered by different meteorological scales. Larger scales can be simulated using mesoscale simulation tools like the Weather Research and Forecasting (WRF) model [Powers et al., 2017]. The spatial resolution in this context can vary from a few kilometers to hundreds of kilometers, while the temporal scale can range from several minutes to several months. This model is versatile and can be used to simulate flows representing diurnal cycles

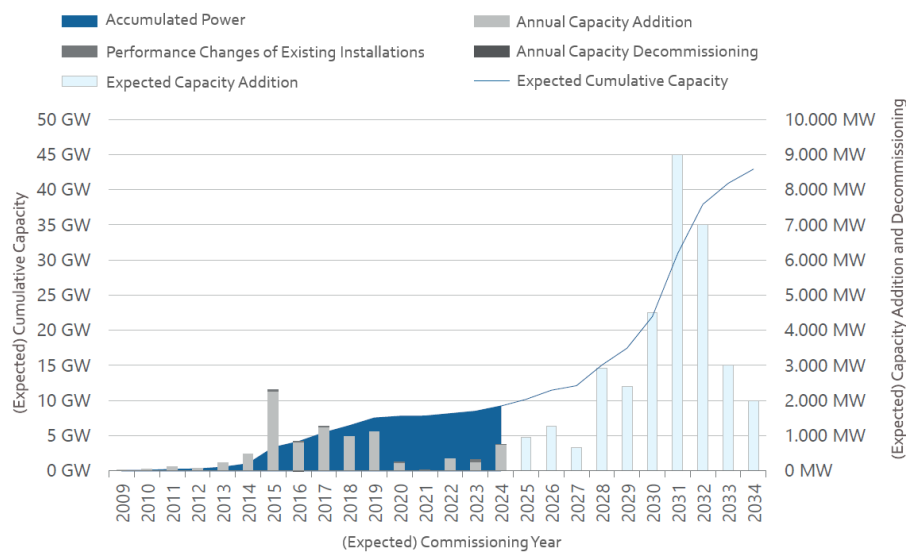


Figure 1.1: Expected Development of Offshore Wind Energy Capacity in Germany. Source: [Wind-Guard \[2025a\]](#).

or seasonal variations. Furthermore, it also considers topographical influences such as coastlines and mountain ranges. Clusters of wind farms can also be represented, with a simplified parameterization illustrating the impact of these wind farms on the flow.

The microscale offers a higher resolution, which is effectively captured by Large-Eddy Simulations (LES), like the model PALM [[Maronga et al., 2020](#)], in simulations. The spatial scale for this can range from millimeters up to approximately 1 kilometer, with the resolution of LES typically falling within 1 meter to less than 100 meters. Such simulations are ideal for simulating single or multiple wind turbines, up to a wind farm. Additionally, LES can accurately represent atmospheric flows and stratification, which refers to the layering of different air masses in the atmosphere based on temperature, density, or other properties. This stratification can significantly influence wind patterns and turbulence. LES resolves large energy-carrying eddies that dominate the flow dynamics while parameterizing the subgrid scales (SGS), these are the smaller turbulent structures that cannot be explicitly resolved due to computational limitations. By parameterizing these subgrid scales, LES can still capture their effects on larger scales, ensuring a more comprehensive representation of atmospheric conditions.

To depict the aerodynamic conditions on an individual rotor blade, a significantly higher resolution is required, necessitating scales in the millimeter range. Approaches such as Direct Numerical Simulation (DNS) are suitable for this, although they are highly computationally intensive.

These models are designed around their primary focus, which often leads to limitations in other areas. For example, a mesoscale model like WRF cannot accurately calculate turbine responses (e.g. blade loads), whereas a microscale model like LES cannot effectively represent global weather conditions. One of the key challenges in wind energy research and development is bridging these scales, as noted by [Veers et al. \[2019\]](#). Various approaches exist for linking scales for specific purposes. For instance, several methods have been developed to integrate weather data into LES models to visualize realistic diurnal cycles at higher resolutions, often aimed at analyzing urban flows [[Wyszogrodzki](#)

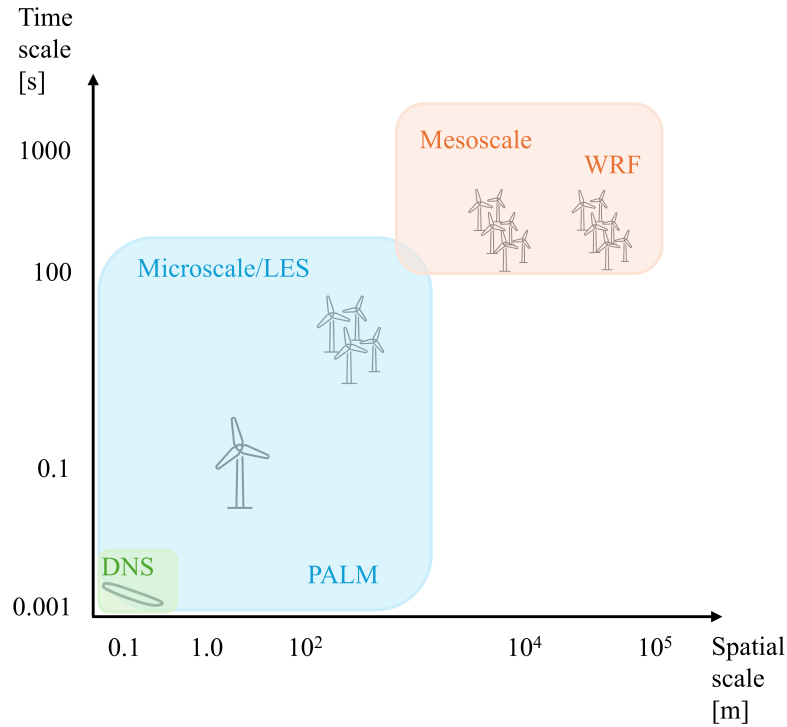


Figure 1.2: Schematic representing the scales and their corresponding temporal and spatial resolution.

et al., 2012, Lin et al., 2021, Vogel et al., 2022].

For the design of wind turbines, less computationally intensive engineering models are usually used by the wind energy industry. These models are supposed to reflect the turbine behavior under various flow conditions, but must work quickly and efficiently. Examples of such models are FAST [fatigue, aerodynamics, structures, and turbulence Jonkman and Buhl Jr., 2005] or Bladed [DNV GL, 2020], which are commonly used in the wind energy industry. These aeroelastic models, which account for the interaction between aerodynamic forces and structural deformations, require a wind field as input, which can be varying in complexity, and can then calculate the reaction of the turbine, including blade loads, tower loads, torque and power. With such an engineering model, the wind energy industry can develop turbine designs and load assessments without the need for expensive hardware infrastructure.

A key challenge for aeroelastic models like FAST is accurately modeling the inflow. Tools like TurbSim [Jonkman, 2009a] can generate turbulent wind fields based on stochastic models, but their simplified turbulence assumptions and coarse resolution may limit accuracy in complex flow conditions. Since turbulence, shear, and stability significantly influence wind turbine loads, accurate inflow modeling is essential.

In LES simulations, parameterization options for representing turbines in the flow have been available for some time as detailed in Section 2.1. However, these simulations quickly reach a limit in the turbine information they can provide. Conversely, there are the aeroelastic models utilized by the wind energy industry that offer sufficient turbine data for designing wind turbines and assessing their performance, but do not capture the inflow conditions with sufficient accuracy. Therefore,

combining these tools, specifically coupling LES with an engineering turbine model, could yield significant benefits. In this study, we utilize and consider the LES model PALM, and the aeroelastic tool FAST, which will both be introduced in Chapter 2. This approach results in two variants of the PALM-FAST coupling.

1.1 Impact of atmospheric flow conditions on wind turbines

Atmospheric stability impacts several factors, including wind speed, wind shear, turbulence, and temperature, all of which significantly affect wind turbine performance. For instance, variations in atmospheric stability can lead to differences of up to 15% in average power output, as documented by studies such as [Wharton and Lundquist \[2012\]](#). Wind shear directly affects turbine loads, impacting their service life, while turbulence influences wake recovery, which is particularly important for wind farms with multiple turbines. Unstable atmospheric stratification typically results in higher turbulence compared to stable stratification, leading to different wake characteristics, as discussed in [Vollmer et al. \[2016\]](#).

LES have proven effective in simulating various atmospheric stability conditions, from stable [e.g., [Beare et al., 2006](#), [Kosović and Curry, 1998](#)], to neutral [[Porté-Agel et al., 2011](#), [Drobinski et al., 2007](#)], to unstable stratifications [[Maronga and Raasch, 2013](#)]. When turbines are included in these simulations, they offer valuable insights into turbine performance and wake behavior under controlled conditions, as seen in [Witha et al. \[2014\]](#), [Vollmer et al. \[2016\]](#). While turbine parameterization within LES enables the analysis of power output and thrust in the rotor plane, it is limited in providing detailed insights into turbine loads and other structural parameters. Nevertheless, the insights gained from LES serve as a foundation for developing and validating less computationally expensive models, such as Reynolds-averaged Navier–Stokes (RANS) [[Lübcke et al., 2001](#)] or Kaimal/Mann models [[Doubrawa et al., 2019](#)].

Offshore and onshore wind conditions further emphasize the need for accurate simulations that effectively capture the unique atmospheric dynamics, turbulence characteristics, and flow patterns specific to each setting. Offshore environments, characterized by low roughness lengths and potential coastal effects, often exhibit more complex wind conditions compared to onshore locations (see also Section 1.3). Conversely, onshore wind conditions are heavily influenced by topographical features.

To calculate wind turbine loads, models like FAST [fatigue, aerodynamics, structures, and turbulence [Jonkman and Buhl Jr., 2005](#)] or Bladed [[DNV GL, 2020](#)] are commonly used. These models require wind fields as input, which are typically generated using simpler tools like TurbSim [[Jonkman, 2009a](#)]. While TurbSim can efficiently generate randomized turbulent structures, it is based on simplified turbulence models, such as the Mann model [[Mann, 1998](#)] or the Kaimal model [[Kaimal et al., 1972](#), [IEC, 2005](#)], which often assume Gaussian statistics and fail to capture intermittency observed in real wind conditions [[Mücke et al., 2011](#)]. This limitation can significantly affect the accuracy of turbine load predictions, as small-scale turbulent structures and non-Gaussian turbulence are critical in complex flow conditions. Moreover, the coarse resolution of turbulence and reliance on assumptions about turbulence characteristics limit the applicability of such tools for highly sheared or stratified flows, or flows over complex terrain. In contrast, LES provides a more comprehensive representation of real-world wind conditions by simulating intermittent and non-Gaussian turbulence [[Bock et al., 2024](#)]. Given that turbulence, shear, and atmospheric stability have a major influence on the structural loads of wind turbines, sufficient modeling accuracy is essential to capture these effects. Ultimately, a comprehensive analysis of wind turbines in atmospheric flows using LES, while accounting for various atmospheric conditions and phenomena, is essential to optimize turbine performance, extend their lifetime and enhance the efficiency of wind power generation.

1.2 Wind turbine parametrization - Actuator sector models for wind turbines

Various approaches have been developed to represent the effects of wind turbines in numerical simulations, each balancing computational demand and the quality of results. As illustrated in Figure 1.3, the Actuator Disk Model (ADM), both in its standard form without rotation and its extended version with rotation (ADM-R), is among the most commonly used turbine models, along with the Actuator Line Model (ALM). In ADM and ADM-R, the rotor is modeled as a disk, while the ALM represents the blades as separate lines in the flow. Additionally, the Actuator Sector Model (ASM), which divides the turbine into circular segments, bridges the gap between ADM(-R) and ALM by offering a compromise in terms of computational efficiency and detailed turbine output [Storey et al., 2015, Krüger et al., 2022]. Often, the tower of the wind turbine is neglected or alternatively represented with a fixed drag coefficient at the corresponding position, leading to a blockage of the flow at that location. The various methods of wind turbine parameterization in LES are elaborated upon in Section 2.1.2.

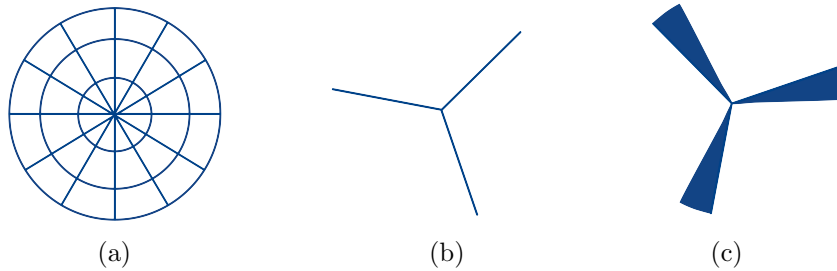


Figure 1.3: Various approaches to represent the effects of wind turbines in numerical simulations: (a) ADM-R, (b) ALM and (c) ASM.

The computational costs associated with these models vary significantly. The ADM without rotation has relatively low computational demands and provides accurate results for mean wind speeds in the far wake. However, the model cannot capture the double Gaussian structure of the near wake or resolve quantities along the blades [Witha et al., 2014b] due to the missing rotation. In contrast, the ALM provides more detailed information, such as blade and tower loads, but requires significantly more computational resources due to rotor speed limitations on the time step. The ASM offers a middle ground, delivering detailed turbine outputs while improving computational efficiency compared to an ALM [Krüger et al., 2022]. Furthermore, the accuracy of all these models depends on factors such as the method used to project turbine forces into the flow, grid resolution, and the sampling of wind speed at blade positions. For instance, as shown in Martínez-Tossas et al. [2015] and Churchfield et al. [2017], the method of force projection can influence simulation results, while Mittal et al. [2015] demonstrated that different wind speed sampling methods at blade positions can impact power and thrust output.

Storey et al. [2015] introduces an ASM within an LES framework, emphasizing an accurate representation of the wind turbine wake while achieving greater computational efficiency compared to ALM simulations. The ASM provides enhanced resolution over ADM-based simulations and was tested using the generic NREL 5 MW turbine [Jonkman et al., 2009b]. The results show that the

ASM significantly improves flow solution accuracy compared to an ADM. The ASM in [Storey et al. \[2015\]](#) demonstrates a marked reduction in computational time while achieving a similar accuracy as ALM simulations. However, the study primarily focuses on flow effects and does not investigate detailed turbine behavior, such as loads or power output. This type of analysis would require coupling with an aeroelastic tool like FAST. Unlike ALM and ASM, which are parametrizations applied to atmospheric flows in LES, the engineering model FAST requires inflow data. The quality of the results from FAST is highly dependent on the accuracy of this inflow data. Once provided with reliable inflow information, FAST can effectively assess turbine dynamics, including loads and power output. Additionally, FAST, like other aeroelastic models, represents the movement of the rotor blades individually, allowing for a more detailed analysis of their aerodynamic interactions and structural responses during operation.

Several studies have explored LES-aeroelastic couplings to investigate turbine loads. For example, [Lee et al. \[2012\]](#) employed a coupling between an LES model and the aeroelastic code FAST, synchronizing their time steps. However, this approach was constrained by the small time step required for the ALM, leading to high computational costs. Similarly, the open-source ExaWind framework [[Sprague et al., 2019](#)] couples the LES code Nalu-Wind [[Domino, 2015](#)] with OpenFAST [[Jonkman, 2013](#)], incorporating ALM, moving meshes, and fluid-structure interaction (FSI) to provide high-fidelity turbine simulations. While this method delivers detailed results, it comes with substantial computational demands. Other FSI couplings, such as those presented in [Vitsas and Meyers \[2016\]](#) and [Santo et al. \[2020\]](#), facilitate research into topics like the impact of tilt on turbines or the loads experienced by turbines within wind farms.

Balancing computational cost and accuracy becomes even more critical when coupling an LES with an aeroelastic tool, such as coupling PALM with FAST. The primary limitation of this coupling is the computation time required for the LES, specifically PALM, which should be optimized to the greatest extent possible. However, a direct coupling with a coupled time step between LES and an aeroelastic code would mean a very small time step and a high computing time for the LES model. FAST, similar to other aeroelastic models, captures the individual movement of rotor blades. This allows a directly coupled time step to be translated into an ALM representation within the LES. However, this is not ideal due to the substantial computational time it requires. One goal of this thesis is, therefore, to establish a computationally efficient coupling between flow simulations, such as LES, and aeroelastic turbine dynamics modeling, like FAST. This is achieved by optimizing the time stepping in the LES simulations while decoupling it from the time stepping in the FAST simulations. To facilitate this approach, the ASM parameterization of the turbine was implemented in the LES model PALM, making it well-suited for the task. The ASM model represents the turbine in the flow by dividing the area swept by the blade into sectors corresponding to the PALM time step. The technical details of the PALM-FAST coupling are provided in Chapter 3.

In the best-case scenario, ASM results are comparable to those of ALM, but with significantly lower computational costs. A key factor influencing ASM accuracy is the sampling of wind speed, which is used to calculate aerodynamic forces on the rotor blades. Ideally, the sampled wind speed should reflect the flow affecting the blades. However, ALM implementations often overestimate wind speeds and turbine power output. This is mainly caused by the required projection of the blade forces onto the LES grid, which is designed to maintain numerical stability. However, this approach deviates from accurately reflecting the actual effect of blade movement on the flow. To project aerodynamic forces onto the computational grid, where u , v , and w are defined, turbine

models such as ALM, ADM(R), and ASM rely on a Gaussian-shaped distribution [Sørensen et al., 1998]. The smearing coefficient, a parameter defining the width of this Gaussian distribution, directly controls how forces are spread across the grid. This coefficient is tied to the grid size and influences the velocity field near the blades [Troldborg, 2008, Mikkelsen, 2003], thereby affecting the accuracy of both the turbine response and the flow representation. Consequently, the smearing coefficient becomes a critical adjustment factor in turbine simulations.

Martínez-Tossas et al. [2017] proposed an analytical method to optimize the smearing coefficient by comparing the velocity field to a desired potential velocity field for a uniform inflow. They found that the optimal value depends on the ratio of grid size to blade chord length, requiring recalibration for each simulation setup.

Alternatively, a universal approach to address inaccuracies in blade velocities caused by force projection is described in Dag [2017] and further refined in Meyer Forsting et al. [2019]. These authors identified the root cause of the problem. The ALM representation developed by [Sørensen and Shen, 2002] of a turbine is intended as a lifting line method. However, due to the numerical requirements, the Gaussian shaped distribution of the forces is chosen, which does not represent the lifting line theory (LLT) entirely [Dag, 2017]. To counteract, Dag [2017] proposes a correction based on the dynamic near-wake model, described in Pirrung et al. [2016, 2017a,b], with a viscous core model [Lamb, 1932, Oseen, 1911]. This method is discussed in detail in Chapter 2.3.

In Meyer Forsting et al. [2019] the deficits of the Gaussian smearing used in ALM are discussed and a solution based on the considerations described in Dag [2017] is presented. According to Dag [2017] the discrepancy between the lifting line theory and the Gaussian shaped smearing can be reduced by considering the Lamb-Oseen vortex.

Meyer Forsting et al. [2019] demonstrated that the correction mentioned above leads to improved results for the NREL 5 MW turbine with stiff blades, with the drawback to be computationally costly. To address this, Meyer Forsting et al. [2020] proposed a reduced version of the correction that significantly decreases computational time, while maintaining the quality of the corrected results. As a result, this method proves to be a valuable addition to existing ALM codes, as it does not significantly increase overall calculation time. The correction method proposed in Meyer Forsting et al. [2020] is from now on denoted as NWC (near-wake correction). In Hodgson et al. [2022], the NWC, developed for rigid rotor blades, was evaluated in ALM configurations for flexible rotor blades. The results indicated that the NWC also enhances performance in this context, particularly improving load calculations. However, it was noted that its effectiveness is sensitive to flow conditions, with performance deteriorating under high shear and yaw values.

In Mohammadi et al. [2024a] the main focus was to investigate the wind speed sampling positions for ASM simulations in comparison to ALM results, using a laminar flow and a fixed LES time step (and thus a fixed sector size). Additionally, the study explored the impact of applying wind speed corrections, such as the NWC, on ASM results. Two main velocity sampling methods were analyzed for ASMs: sampling at the position of maximum smeared forces within the sector, or sampling at the new blade position before forces are smeared at that position. For both strategies, several positions were selected for sampling the wind speed and the results were compared with those of an ALM. Mohammadi et al. [2024a] found that, for the case under consideration, the best agreement with the ALM results was achieved when wind speed sampling was conducted at 70% of the sector for the sampling method within the sector where the forces were already smeared. Or correspondingly at 0% of the sector if the sampling was carried out at the position of the new sector, adjacent to the

previously smeared forces. Besides the examined positions for wind speed sampling, [Mohammadi et al. \[2024a\]](#) also evaluated the ASM method incorporating wind speed corrections, including the NWC. The application by [Mohammadi et al. \[2024a\]](#) of this correction in an ASM yielded promising results, comparable to an ALM that also incorporated the same correction.

[Mohammadi et al. \[2024a\]](#) points out in the study that the quality of the agreement of the ASM with an ALM depends on the tip speed ratio (TSR). It should also be noted that the investigation is limited to a laminar flow with a fixed sector size. Its general applicability must therefore still be confirmed. A comparison of ASM using the suggested position for velocity sampling with measurement data has yet to be conducted.

The methodology of [Mohammadi et al. \[2024a\]](#), specifically the 70% position, was implemented in a coupling of an LES with OpenFAST (the current format in which FAST is provided and further developed [[OpenFAST](#)]), as detailed in [Mohammadi et al. \[2024b\]](#). In this instance, a turbulent case was simulated, and the results of the ASM simulation were compared to those from an ALM simulation. Notably, both methods were computed without any wind speed corrections, leading to an overestimation of the power data. In addition, it should be noted that validation with actual measurement data was not performed in this study. The clarity and comparability of these results with actual data remain ambiguous. In addition, the behavior in more complex scenarios, e.g. when one turbine is in the wake of another, has not yet been investigated.

The referenced publications conduct various studies on ASM implementations, including one focused on coupling an ASM with an aeroelastic tool [[Mohammadi et al., 2024b](#)]. These studies emphasize computational efficiency, the accurate representation of wind turbine wakes, and comparability to ALM. A comparative analysis with ALM simulations demonstrates that ASM provides significant improvements in computational time while also offering better accuracy than the ADM parameterization.

However, some important aspects remain unaddressed in the mentioned studies. For instance, the studies by [Mohammadi et al. \[2024a,b\]](#) are limited to one laminar and one turbulent flow with a fixed sector size, leaving uncertainty about their applicability to other scenarios. Additionally, they do not investigate complex configurations, such as scenarios where one turbine operates in the wake of another. Another critical omission is the lack of validation against measured data, which is essential for evaluating the accuracy and reliability of the proposed methods in real-world applications.

Chapter 5 of this thesis addresses these open questions by investigating the applicability of coupling an ASM in LES, including the NWC, with an aeroelastic code in complex flow scenarios, such as a turbine in the wake of another. The simulations are validated against measured data to assess their accuracy. This ensures a more comprehensive understanding of ASM performance in such a coupling and its potential for broader applications.

1.3 Effect of upstream heterogeneities on the downstream offshore flow

Offshore wind energy plays a pivotal role in the energy transition. The maritime environment presents unique flow conditions that differ significantly from those on land. Characteristics of offshore settings include a low roughness length and a high thermal capacity of the subsurface.

Coastal regions, extending several tens of kilometers offshore, hold significant importance for wind energy. The strategic placement of offshore wind farms is influenced by several factors. These factors, including water depth, proximity to the coast, and site availability, play a critical role in determining the viability and potential productivity of wind farms. Land-to-sea flows can create complex wind patterns, leading to challenging operating conditions for turbines. As emphasized in [Schulz-Stellenfleth et al. \[2022\]](#), these coastal effects can significantly impact offshore wind farms. Therefore, a comprehensive understanding of coastal effects on wind farms is crucial. It can substantially enhance the planning, design and operational strategies of offshore wind energy, optimizing their performance and efficiency.

In the study by [Kethavath and Ghaisas \[2024\]](#), the impact of a roughness transition, such as the shift from onshore to offshore, on offshore wind farms was analyzed using LES. Changes in turbulence statistics were found in the flow at the wind farm that would not have been present without the roughness jump. In the analyzed case, the roughness was changed over the entire lateral length and the transition from a rough to a smoother surface was considered. In this case, the turbulence statistics changed compared to a case without roughness change. Leading to a change in the velocity deficit within the wind farm as a result of the increased turbulence. This in turn leads to an increased power output in the simulated case. The study focuses on a specific example of roughness change without lateral variation and does not explore additional variations in surface properties.

The introduction of additional heterogeneities along the coast, beyond the transition from rough to smooth surfaces, can lead to flow structures downstream. These structures can result in strong gradients lateral to the primary flow direction and stripes of reduced wind speeds. Under stable conditions, these low-speed streaks can extend several tens of kilometers offshore from the coast [[Dörenkämper et al., 2015](#)]. Heterogeneities stem from different land uses, e.g. urban use next to grassland and are reflected in roughness length or temperature differences.

Research utilizing LES has explored the flow directly over surface heterogeneities [[Avissar and Schmidt, 1997](#), [Raasch and Harbusch, 2001](#), [Letzel and Raasch, 2003](#)], revealing the occurrence of secondary circulation induced by the heterogeneities. In [Avissar and Schmidt \[1997\]](#) the focus was on the investigation of surface heterogeneities generated by waves in the surface heat flux. These waves were generated with different amplitudes and wavelengths and their influence on the convective boundary layer (CBL) was analyzed. Strong circulations above the heterogeneities, were observed for large amplitudes and wavelengths of the surface heterogeneity. These lead to strongly altered profiles of the horizontally averaged variables of the CBL. It was also observed that background wind can reduce or even eliminate these effects, as investigated here, for flows aligned with the surface heat flux. Despite the comprehensive analysis, [Avissar and Schmidt \[1997\]](#) did not delve into the investigation of the downstream effects of these surface heterogeneities. The study primarily concentrated on the flow above the heterogeneities, revealing significant circulations and alterations in the profiles of the horizontally averaged variables of the CBL.

In Raasch and Harbusch [2001], the LES model PALM [Raasch and Schröter, 2001] was used to investigate the relevance of the size of heterogeneities for a CBL. Two-dimensional, discontinuous, small-scale surface heterogeneities were simulated in the LES. It was observed that the effects are most pronounced when the heterogeneities have the size of the boundary layer height. Not only the surface roughness was varied here, but also the thermal properties. The thermal variations seem to have a greater influence on the CBL structure than the change in surface roughness. These effects are mainly on the variances of the velocity components, i.e. the characteristics of turbulence, not so much on the potential temperature or the heat flux, averaged using a phase-averaging method. The results of Raasch and Harbusch [2001] were confirmed in Letzel and Raasch [2003]. Here it was found that circulations induced by surface heterogeneities that are larger than 5 km can significantly change the turbulent transport processes and trigger oscillations. Letzel and Raasch [2003] also found that the circulations have a greater kinetic energy than a flow under homogeneous conditions. These thermally induced mesoscale circulations can trigger a temporal oscillation of the atmospheric boundary layer (ABL) flow, so that the influence of the heterogeneities appears to change with time. In confirming the findings of Raasch and Harbusch [2001], Letzel and Raasch [2003] added to the understanding of the effects of large-scale surface heterogeneities on turbulent transport processes. However, similar to previous studies, the focus remained on the immediate impacts, particularly on the kinetic energy and temporal oscillation of the ABL flow. The downstream effects of these thermally induced mesoscale circulations, a critical aspect of the broader impact of these phenomena, were not incorporated into the study.

The LITFASS-2003 experiment was taken as the basis for an LES study in Maronga and Raasch [2013]. The LES utilized surface boundary and initial conditions derived from the experiment with the objective of visualizing the secondary circulations induced by surface heterogeneities. These play a significant role in the transport of heat and moisture [Maronga and Raasch, 2013]. Visualizing these secondary circulations poses challenges, but temporal and spatial averaging, as well as ensemble averaging, can make them visible. Maronga and Raasch [2013] also observed that a higher background flow results in the formation of roll-like circulations aligned with the main wind direction. Additionally, the study found evidence that the effects of surface heterogeneities in the order of the boundary layer height in a CBL can persist until the capping inversion. This can lead to horizontal variations in the boundary layer depth. Maronga and Raasch [2013]’s study, based on the LITFASS-2003 experiment, contributes significantly to the visualization of secondary circulations induced by surface heterogeneities, emphasizing their role in heat and moisture transport. The research also sheds light on the impact of a higher background flow and the persistence of effects from surface heterogeneities. However, the study does not extend to the exploration of the downstream impacts of these phenomena.

The study Paleri et al. [2024] investigates the influence of surface heterogeneities on the secondary circulation in the ABL using LES of the CHEESEHEAD19 field campaign. It provides an insight into the effects of surface heterogeneity on the dynamics of the ABL. The authors used LES to investigate how effective surface length scales, determined by the spatial arrangement of surface patches, and the stability of the ABL influence the secondary circulation induced by heterogeneous land surfaces. Their results show that surface heterogeneities have a significant influence on the transport processes in the ABL when the ratio of the effective surface length scale to the ABL height is greater than one. The study emphasises the importance of integrating surface heterogeneities into weather forecasting and climate models to better understand local atmospheric conditions and wind dynamics. This understanding is crucial for accurate weather forecasting, which is essential for optimising wind

energy generation and management.

In Zhang et al. [2025], the development and decay of secondary vortices induced by variations in surface roughness are investigated. To achieve this, LES incorporating spanwise roughness changes are employed. In each simulation, cubes are introduced into the model domain, with different simulations utilizing cubes of varying sizes. Downstream of the cubes, the model domain retains the same length as it did when the cubes were present, but without the cubes themselves. This setup enables the analysis of the resulting secondary vortices' decay. The study reveals that this decay follows an exponential trend, and a phenomenological model is proposed to predict it. The characteristic decay length is determined to be between 25 and 50 boundary layer heights.

Both Paleri et al. [2024] and Zhang et al. [2025] provide further insights into the intricate dynamics of the ABL, illuminating the significant role surface heterogeneities play in these processes. Their findings underscore the necessity of integrating such heterogeneities into weather forecasting and climate models to optimize wind energy management. While Zhang et al. [2025] goes a step further to investigate the decay of secondary vortices induced by surface roughness variations, the exploration of the downstream effects of surface heterogeneities is still not fully addressed. Specifically, the parameters influencing the strength of these downstream structures remain unexplored.

Gaining a comprehensive understanding of the downstream effects necessitates an in-depth investigation into how various surface parameters and their combinations - such as roughness length, temperature, and the width of a heterogeneity - shape these impacts. It is particularly important to consider these effects in the context of a downstream flow occurring over a homogeneous surface with a low roughness length, akin to a sea surface. This nuanced understanding could significantly enhance the accuracy of predictive models used in the field of offshore wind energy generation.

For wind energy, accurate predictions of site conditions are crucial. Given the common placement of offshore wind farms in coastal effect zones, understanding coastal effects on wind turbines is vital. Hence, it is evident that the coast's influence, especially its heterogeneity, is a crucial factor for the optimal utilization of offshore wind energy. Further research into which parameters significantly influence downstream structures could lead to more accurate predictive models and more efficient utilization of wind energy. This is where the integration of an LES tool with an aeroelastic tool comes into play, as realized by the PALM-FAST coupling in this work. The LES tool PALM excels in accurately modeling atmospheric flow and simulating effects induced by heterogeneities, while the FAST aeroelastic tool comprehensively captures the turbine's response.

1.4 Objectives and structure of the thesis

In the field of high-fidelity wind energy simulations, various methods are available, each with distinct advantages and limitations. Fast and less accurate methods, such as the ADM, are suitable for simulating scenarios with uniform wind fields and large wind farms, facilitating rapid analysis and optimization of wind farm locations. However, these methods struggle to accurately model situations behind coastlines or in complex topographical conditions where local effects, such as wakes and turbulence, are significant. In contrast, more accurate yet computationally intensive methods, like the ALM, provide deeper insights into turbine interactions and atmospheric conditions, particularly in complex scenarios.

Despite these advancements in wind energy simulation methodologies, significant knowledge gaps persist in the field. A critical area of concern is the validation of existing models under specific turbulent scenarios, particularly regarding wind turbine wakes. Furthermore, many of the more accurate models are computationally intensive, rendering them impractical for real-world applications. Therefore, there is a pressing need for a cost-efficient numerical solution that can effectively bridge the gap between realistic inhomogeneous turbulent atmospheric flows and precise turbine responses. Additionally, understanding the underlying processes that contribute to observed inhomogeneities, especially in land-sea transitions, is essential for determining their impact on offshore turbine performance.

This thesis aims to address these identified gaps by advancing the understanding of wind turbine dynamics in atmospheric flows through various critical aspects. A key emphasis is placed on validating the proposed PALM-FAST coupling using measurement data, which will extend the research to various scenarios, including complex situations such as turbines operating within the wake of others. Additionally, this research presents systematic simulations of heterogeneous coastal transitions, utilizing the validated PALM-FAST coupling to investigate the effects of heterogeneity-induced structures on wind turbines within the marine atmospheric boundary layer.

Ultimately, the contributions of this dissertation seek to enhance the accuracy and applicability of wind turbine dynamics modeling in complex atmospheric conditions.

Objectives

Based on the state of the art of numerical simulations for the calculation of the behavior of wind turbines in atmospheric flows at the time of writing this thesis, the primary objectives of this dissertation are:

- **Objective 1:** To reliably and computationally efficiently represent the influence of complex inflow conditions on turbine dynamics in simulations.
- **Objective 2:** To investigate the impact of surface roughness and temperature variations at the coast on flow structures and turbine dynamics within and behind a nearby offshore wind farm.

To achieve these objectives, the following research questions are addressed:

- Can the coupling between the LES tool PALM and the aeroelastic model FAST be validated against measurement data for mapping turbine behavior under varying atmospheric conditions?

- How does the PALM-FAST coupling perform in a complex scenario involving one turbine operating in the wake of another?
- How do downstream structures from heterogeneities affect wind turbine performance within the flow?
- Which parameters influence the strength of downstream flow patterns and lateral gradients due to surface heterogeneities in land-sea transitions and what mechanisms and impacts are observed?

Structure of the thesis

Chapter 2 delves into the methodologies employed. The technical background is explained, such as the numerical fundamentals and the types of wind turbine parameterization of the LES model PALM, the aerodynamic fundamentals of FAST and the method behind the NWC.

In **Chapter 3**, technical aspects of the PALM-FAST coupling are presented that are not covered in the subsequent chapters.

Chapter 4 presents a variant of the PALM-FAST coupling that incorporates the SWIRL induction model in FAST to address the overestimation of wind speeds in the calculation of aerodynamic forces. In addition, measurement data and their processing are presented, which were used to validate the proposed coupling. Simulation results of the PALM-FAST coupling were compared with measurement data and the performance, blade and tower loads were analyzed in comparison. The results and findings of this work were published in the peer-reviewed paper: Krüger et al., 2022, *Validation of a coupled atmospheric-aeroelastic model system for wind turbine power and load calculations*.

Chapter 5 introduces an evolved version of the PALM-FAST coupling. To ensure broader applicability, several modifications were made to the variant outlined in Chapter 4. This revised model chain underwent validation using measurement data, with an additional verification involving one turbine operating in the wake of another, conducted through a model-to-model comparison.

Chapter 6 systematically explores the downstream flow along a geometrically idealized coastline by varying conditions. Variations in parameters such as roughness, temperature and the width of the heterogeneity are examined. Furthermore, simulations were conducted with wind turbines positioned at various points in the resultant flow. The PALM-FAST coupling, as detailed in Chapter 5, was employed and an analysis of turbine performance and loads was performed.

The final chapter of the thesis, **Chapter 7**, contains the conclusion, in which the most important findings from the previous chapters are summarized and related to the research questions. An outlook is also provided, in which possible future directions and progress in this area are discussed based on the research carried out as part of this thesis.

Chapter 2

Foundational methods and models

This chapter outlines the existing models and methods utilized in this thesis, emphasizing the underlying theories and techniques. It serves as a foundational resource and supplement for the work presented in Chapters 4 to 6.

2.1 PALM

In this thesis, the LES model PALM [Maronga et al., 2015, 2020] was used to simulate atmospheric flow. This chapter explains the fundamentals of LES and describes the existing wind turbine models, which serve as the basis for the development of the new methods presented in this thesis.

2.1.1 Governing equations and numerical methods in PALM

In this subsection, we will focus on the core components of PALM, including the governing equations, the pressure solver, the turbulence closure, the spatial and temporal discretization, the time step limitation and the boundary conditions. Each of these elements plays a crucial role in the functionality of the model and the accurate representation of the atmospheric flow.

Governing equations

The motion processes in atmospheric flows can be described by the conservation of momentum (Eqn. 2.1) and mass (Eqn. 2.2). These basic equations can describe the motion in a dry atmosphere [Sengers, 2023].

$$\underbrace{\frac{\partial u_i}{\partial t}}_{(a)} + \underbrace{u_j \frac{\partial u_i}{\partial x_j}}_{(b)} = - \underbrace{\frac{1}{\rho} \frac{\partial p}{\partial x_i}}_{(c)} + \underbrace{\frac{1}{\rho} \frac{\partial \tau_{ij}}{\partial x_j}}_{(d)} + \underbrace{\delta_{ij} g_j}_{(e)} - \underbrace{2\epsilon_{ijk} \Omega_j u_k}_{(f)} \quad (2.1)$$

$$\frac{\partial \rho}{\partial t} + \frac{\partial(u_j \rho)}{\partial x_j} = 0, \quad (2.2)$$

where u_i is the wind velocity field, t the time, ρ the air density, p the atmospheric pressure, x_i the spatial coordinates, τ_{ij} the stress tensor, g the gravitational acceleration vector, Ω the angular velocity vector, δ_{ij} the Kronecker-Delta and ϵ_{ijk} the Levi-Civita symbol.

The equation of conservation of momentum consists of several terms:

- (a) Storage of momentum
- (b) Advection
- (c) Pressure gradient
- (d) Viscous Forces
- (e) Gravitational Force/Buoyancy
- (f) Coriolis Force

The equations presented above represent the unfiltered version of the dynamics involved. In LES, however, a filtering process is applied according to the grid size. This means that smaller scales are parameterized, while larger scales are directly calculated. In PALM, this filtering is accomplished using a spatial scale separation approach as outlined by Schumann [1975]. The following equations will therefore provide the filtered representation suitable for LES. In general, in the equations, a double prime denotes subgrid scale (SGS) variables, while an overbar signifies filtered quantities.

In order to be able to describe the movements in the atmosphere, assumptions must be made for the basic equations. For the turbulent processes in the atmosphere, for example, it must be assumed that the vertical velocity component is of the same order of magnitude as the horizontal velocity component. The Boussinesq approximation can be used here. The Boussinesq approximation means that the change in density is neglected in all terms except the buoyancy term (e) [Stull, 2003]. The pressure p is split into a mean state \bar{p} and a deviation from it: $p = \bar{p} + p^*$. The deviation p^* consists of the resolved scales π^* minus the parameterized subscales $\frac{2}{3}\rho e$, where e is the subgrid-scale turbulent kinetic energy, leading to Eqn. 2.3:

$$-\frac{1}{\rho} \frac{\partial p}{\partial x_i} = -\frac{1}{\rho} \frac{\partial \bar{p}}{\partial x_i} - \frac{1}{\rho} \frac{\partial \pi^*}{\partial x_i} + \frac{\partial^2 e}{\partial x_i^2}. \quad (2.3)$$

Looking now at the vertical direction only, one can use term (e) of Eqn. 2.1 and the term of the mean pressure in Eqn. 2.3 and substitute, using the assumptions of the Boussinesq approximation, the hydrostatic law $d\bar{p} = -\rho_0 g dz$ and the inverse relation between ρ and θ , assuming an ideal gas ($p = \rho R \theta$):

$$-g - \frac{1}{\rho} \frac{\partial \bar{p}}{\partial z} = -g + g \frac{\rho_0}{\rho} = g \left(\frac{\rho_0 - \rho}{\rho} \right) = g \left(\frac{\theta - \theta_0}{\theta_0} \right). \quad (2.4)$$

Transferring Eqn. 2.4 to the LES means substituting θ by a box average $\bar{\theta}$ and substituting θ_0 to a domain average $\langle \theta \rangle$:

$$g \left(\frac{\theta - \theta_0}{\theta_0} \right) = g \left(\frac{\bar{\theta} - \langle \theta \rangle}{\langle \theta \rangle} \right). \quad (2.5)$$

Considering the horizontal components, the definition of geostrophic wind can act as a substitute for the horizontal pressure gradient [Stull, 2003]:

$$f_c u_g = -\frac{1}{\rho_0} \frac{\partial \bar{p}}{\partial y} \quad (2.6)$$

$$f_c v_g = +\frac{1}{\rho_0} \frac{\partial \bar{p}}{\partial x}, \quad (2.7)$$

where $f_c = 2\omega \sin \Phi$ and $\omega = 2\pi/86400s$ and Φ being the latitude. Combining the components for the gravity (e) and pressure (c) term, assuming the Boussinesq approximation, and using Eqn. 2.5 leads to:

$$-\delta_{ij}g_j - \frac{1}{\rho_0} \frac{\partial \bar{p}}{\partial x_i} = \epsilon_{i3j} f_c u_{g,j} + \delta_{ij}g \left(\frac{\bar{\theta} - \langle \theta \rangle}{\langle \theta \rangle} \right). \quad (2.8)$$

In addition, the Coriolis force term (f) can be replaced, using the Coriolis parameter f_j as follows:

$$-2\epsilon_{ijk}\Omega_j \bar{u}_k = -\epsilon_{ij3} f_j \bar{u}_k. \quad (2.9)$$

The advection term (b) can be separated into its mean and fluctuating components, a process known as Reynolds decomposition. Term (b) is expressed as follows:

$$\begin{aligned} u_j \frac{\partial u_i}{\partial x_j} &= (\bar{u}_j + u'_j) \frac{\partial (\bar{u}_i + u'_i)}{\partial x_j} \\ &= \bar{u}_j \frac{\partial \bar{u}_i}{\partial x_j} + \bar{u}_j \frac{\partial u'_i}{\partial x_j} + u'_j \frac{\partial \bar{u}_i}{\partial x_j} + u'_j \frac{\partial u'_i}{\partial x_j} \\ &= \frac{\partial \bar{u}_i \bar{u}_j}{\partial x_j} + \frac{\partial u'_i u'_j}{\partial x_j}. \end{aligned} \quad (2.10)$$

Finally, the viscous force term (d) can be disregarded, as molecular friction is minimal compared to other effects.

Substituting the assumptions from Eqn. 2.3 to Eqn. 2.10 into Eqn. 2.1 and 2.2 lead to the filtered form of the equations for conservation of momentum and mass, that are described in [Maronga et al. \[2020\]](#) as two of the governing equations of PALM:

$$\frac{\partial \bar{u}_i}{\partial t} = -\frac{\partial \bar{u}_i \bar{u}_j}{\partial x_j} + \delta_{i3}g \left(\frac{\bar{\theta} - \langle \theta \rangle}{\langle \theta \rangle} \right) - \epsilon_{ij3} f_j \bar{u}_k + \epsilon_{i3j} f_c u_{g,j} - \frac{1}{\rho_0} \frac{\partial \bar{\pi}^*}{\partial x_i} - \frac{\partial}{\partial x_j} \left(\overline{u'_i u'_j} - \frac{2}{3} e \delta_{ij} \right) \quad (2.11)$$

$$\frac{\partial \bar{u}_j}{\partial x_j} = 0. \quad (2.12)$$

Pressure solver

The Boussinesq approximation assumes an incompressible flow, but the relevant equations do not ensure this by themselves, which leads to flow divergences. To correct this, a predictor-corrector method is used.

- Predictor step: The pressure term is omitted from the first equation in the temporal integration, resulting in a preliminary velocity:

$$u_{i,pre}^{t+\Delta t}$$

- Correction step: The prognostic velocity is adjusted to:

$$u_i^{t+\Delta t} = u_{i,pre}^{t+\Delta t} - \Delta t \frac{1}{\rho_0} \frac{\partial \bar{\pi}^{*t}}{\partial x_i}$$

- Incompressibility Condition: The condition of incompressibility leads to a Poisson equation for the pressure:

$$\frac{\partial^2 \pi^{*t}}{\partial x_i^2} = \frac{\rho_0}{\Delta t} \frac{\partial u_{i,\text{pre}}^{t+\Delta t}}{\partial x_i}$$

The solution of this Poisson equation provides a pressure π^* that helps to eliminate divergences in the velocity field. The solution can be calculated using fast Fourier transform (FFT) methods, including singleton FFT and Temperton FFT, or using an iterative multigrid method taking into account non-cyclic boundary conditions, which was used in this work. [Maronga et al., 2015]

Subgrid turbulence closure

A special characteristic of an LES model is the handling of unresolved scales, the subgrid scales (SGS). When the basic equations are filtered in the LES, the filtering process separates the flow field into resolved and unresolved scales. This leads to the appearance of additional terms in the equations, in particular four covariance terms on the subgrid scale. These cannot be calculated explicitly, as these small turbulence structures in the flow are not resolved and therefore no associated values are available. In addition, the associated processes are very complex and depend on many factors that are not mapped in the equations. Therefore, these terms must be approximated or modelled with the help of closure models. In PALM, these SGS terms are parametrized using a 1.5-order closure approach based on Deardorff [1980] in the modification according to the methods of Moeng and Wyngaard [1988] and Saiki et al. [2000]. The closure model states that the energy transport through SGS eddies is proportional to the local gradients of the mean quantities. This means that the model estimates the influence of unresolved turbulence on the resolved scales by linking it to the spatial variations of the mean flow variables.

The covariance term appearing in Eqn. 2.11 can be expressed using the SGS closure approach:

$$\overline{u_i' u_j'} - \frac{2}{3} e \delta_{ij} = -K_m \left(\frac{\partial \overline{u_i}}{\partial x_j} + \frac{\partial \overline{u_j}}{\partial x_i} \right)$$

where K_m is the eddy-transfer coefficient of momentum. Accordingly, there are formulations for temperature, moisture, and passive scalars. The eddy-transfer coefficient of momentum K_m is related to the SGS turbulent kinetic energy (TKE) e :

$$K_m = c_m l \sqrt{e}$$

where $c_m = 0.1$ is a model constant and l is the mixing length, which depends on the height z and the stratification. [Maronga et al., 2015]

Spatial and temporal discretization

In PALM, the model domain is discretized using finite differences and equidistant horizontal grid spacing. Above the atmospheric boundary layer (ABL) the vertical grid can be stretched, in order to reduce the computational effort in the free atmosphere. For the grid an Arakawa C-grid is used, in which the scalar quantities are located in the centre of the grid volumes, while the velocity components are positioned at the edges. This arrangement simplifies the calculation of derivatives and enables a higher effective spatial resolution compared to non-staggered grids.

Different schemes for the time step and advection calculation are possible, standard is the 3rd order Runge-Kutta time stepping method. This is combined with a 5th order scheme to calculate the advection term, as proposed by Williamson [1980]. In Wicker and Skamarock [2002] multiple combinations of time stepping and advection schemes were investigated deeming this combination to be most accurate, while keeping the algorithm simple. An alternative 2nd-order scheme is available, which, while non-dissipative, can lead to significant numerical dispersion. Various time discretization methods, including 2nd-order Runge-Kutta and 1st-order Euler schemes, can also be used. [Maronga et al., 2015]

Time step limitation

In PALM, the time step is determined by the Courant-Friedrichs-Lewy (CFL) and the diffusion criterion. The time step is selected on the basis of the more restrictive criterion, the one which suggests a smaller time step, in order to ensure the numerical stability and accuracy of the simulation. It is also possible to specify a fixed time step.

The CFL criterion refers to the spatial propagation of the flow and ensures that the numerical wave propagation does not exceed the spatial discretization. If the wave moves faster than the grid can resolve, it can lead to numerical instability. This can be expressed using the characteristic velocity u , the time step size Δt , the grid spacing Δx and the CFL factor C_{CFL} , which is a constant:

$$\frac{u\Delta t}{\Delta x} \leq C_{CFL}.$$

Similar to the CFL criterion, the diffusion criterion links the time step Δt to the grid size Δx and the physical properties of the fluid. It prevents the diffusion of a variable from spreading beyond a grid width in one time step. [Maronga et al., 2015]

Boundary conditions

PALM offers various boundary condition options for the upper and lower boundary of the model domain. The most important boundary conditions, where fixed values or gradients are defined at the boundary, are Dirichlet and Neumann.

Additionally, in PALM the Monin–Obukhov similarity theory (MOST) can be applied between the surface and the first grid level. It assumes that there is a layer above the surface in which the momentum and heat flows are constant. For the calculations the roughness length for momentum z_o and heat $z_{o,h}$ are needed. In PALM MOST is applied locally, although there is no theoretical basis for it. However, experience shows the applicability of this method, and it is also used in other LES. Therefore, fluxes, velocities, and scaling parameters are also calculated locally. The vertical profile of the horizontal wind speed $u_h = (u^2 + v^2)^{\frac{1}{2}}$ in the surface layer is thus given by:

$$\frac{\partial u_h}{\partial z} = \frac{u_*}{\kappa z} \Phi_m \left(\frac{z}{L} \right)$$

where $\kappa = 0.4$ is the von Kármán constant, u_* the friction velocity and Φ_m the similarity function for momentum. The similarity function of momentum depends on the Obukhov length L and is used in the formulation of Businger-Dyer in PALM:

$$\Phi_m = \begin{cases} 1 + 5\frac{z}{L} & \text{for } \frac{z}{L} \geq 0 \\ (1 - 16\frac{z}{L})^{-\frac{1}{4}} & \text{for } \frac{z}{L} < 0 \end{cases}$$

The friction velocity u_* is calculated in PALM as:

$$u_* = \left[\left(\overline{u'w'_0} \right)^2 + \left(\overline{v'w'_0} \right)^2 \right]^{\frac{1}{4}}.$$

2.1.2 Wind turbine parameterizations

Various parameterizations are available to represent the effects of a wind turbine in LES. A direct calculation, meaning a fully resolved simulation of a wind turbine within an LES, is not feasible due to the large grid sizes. Therefore, parameterizations are employed to account for the blockage in the flow caused by the turbine.

ADM

The Actuator Disk Model (ADM) is the most computationally efficient approach for parameterizing a turbine. It conceptualizes the turbine as a permeable disk that acts as an obstacle in the flow. Forces are uniformly distributed across the entire disk surface, which prevents the modeling of individual rotor blades. This simplification enhances computational efficiency while still capturing the primary effects of a turbine on the flow. In the far wake, defined as the region more than 10 rotor diameters downstream, most wake parameters are accurately represented [Witha et al., 2014b]. Thus, this method is particularly well-suited for simulating wind farms, where multiple turbines are modeled over relatively large areas. In PALM the ADM parametrization is based on Jimenez et al. [2008] and Calaf et al. [2010]. The thrust force is defined as:

$$F_T = \frac{1}{2} \rho_0 c_T A U_{\text{ref}}^2, \quad (2.13)$$

where ρ_0 is the air density, c_T the thrust coefficient of the wind turbine, depending on the free inflow wind speed at the center of the rotor disk U_{ref} . The axial induction factor a is used to calculate U_{ref} :

$$U_{\text{ref}} = U_d \left(\frac{1}{1-a} \right), \quad (2.14)$$

where U_d is the wind speed at the rotor disk. And the relation between the axial induction factor and the thrust coefficient can be expressed as:

$$a = \frac{1}{2} (1 - \sqrt{1 - c_T}). \quad (2.15)$$

ADM-R

An advanced version of the ADM is the Actuator Disk Model with Rotation (ADM-R), which incorporates the rotation of the turbine while still utilizing the disk representation. In this approach, the disk is divided into rotor ring segments that allow for the calculation of lift and drag forces. A schematic representation of the ADM-R parametrization is presented in Fig. 2.1. This representation

enhances wake quality [Witha et al., 2014b] compared to the ADM, although it still does not enable the modeling of individual rotor blades.

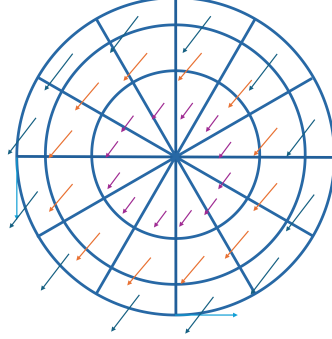


Figure 2.1: Schematic of the ADM-R wind turbine parameterization. The rotor disc is divided into ring segments, with each segment calculating the respective shares of the lift and drag forces individually, as shown by the arrows.

The lift and drag forces are calculated for each rotor ring segment (β) with a span-wise length of Δr using the following equations:

$$F_{L,\beta} = \frac{1}{2} \rho_0 V_{\text{rel}}^2 c_L A_{\text{seg}} \quad (2.16)$$

$$F_{D,\beta} = \frac{1}{2} \rho_0 V_{\text{rel}}^2 c_D A_{\text{seg}}, \quad (2.17)$$

with ρ_0 being the air density, V_{rel} the wind speed relative to the rotor blade, $c_{L,D}$ the lift and drag coefficients respectively and A_{seg} the reference area of the rotor ring segment. The area A_{seg} can be calculated by the number of blades N_B , the chord length c and the distance between the segment and rotor center r : $A_{\text{seg}} = \frac{N_B c}{2\pi r}$.

The forces exerted on the flow are equal in magnitude but opposite in direction to those acting on the blades. To accurately represent these forces on the flow instead of the blades, they are projected and inverted into the axial and tangential directions. A polynomial function (Eqn. 2.21) following a Gaussian form is used to smooth the forces within the model area in the ADM-R of PALM. The polynomial function is based on the principle described for the ALM in Sørensen et al. [1998], Troldborg [2008], see also the subsequent section *ALM*. The smearing of forces is essential because the LES grid points do not align with the locations where the forces were originally computed, and it also enhances numerical stability.

$$\varepsilon = 2\Delta \quad (2.18)$$

$$\varepsilon_{\min} = \left(\frac{105}{32}\right)^{\frac{1}{3}} \cdot \pi^{\frac{1}{6}} \cdot \varepsilon \quad (2.19)$$

$$\varepsilon_f = \frac{105}{32\pi\varepsilon_{\min}} \quad (2.20)$$

$$\eta_\varepsilon(d) = \left[\left(\frac{1}{\varepsilon_{\min}^4} \cdot d - \frac{2}{\varepsilon_{\min}^2} \right) \cdot d + 1 \right] \cdot \varepsilon_f \quad (2.21)$$

where d is the distance between the grid cell center and the blade element from which the respective force stems and ε is a factor of the grid size. Typically it is set to $\varepsilon = 2\Delta$, with Δ being the grid size, as determined by [Troldborg \[2008\]](#).

In contrast to the ADM, both lift and drag forces are calculated alongside the thrust, thereby introducing torque into the flow.

ALM

A more detailed representation of a wind turbine, where the rotor blades are resolved individually, is the Actuator Line Model (ALM), as described in [Troldborg \[2008\]](#), [Churchfield et al. \[2017\]](#). This parameterization is based on the Blade Element Momentum Theory (BEM). Instead of treating the rotor as a disk in the flow, lines are assumed for each individual blade, which are also divided into segments for calculations. Different airfoil-shapes can be assigned to these segments, allowing for an approximate representation of a rotor blade's shape. The forces are calculated per segment using the corresponding segment data, such as lift and drag coefficients and the chord length, see Fig. 2.2 for a schematic representation.

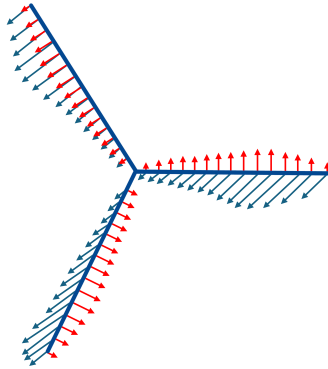


Figure 2.2: Schematic of the ALM wind turbine parameterization. The rotor blades are divided into segments, for each segment the respective lift and drag forces are being calculated individually, as shown by the arrows.

The detailed resolution of individual rotor blades allows for a more thorough investigation of

their effects on the flow. This leads to a better representation of the near wake compared to disk models [Witha et al., 2014b]. However, a significant drawback of the ALM is the high computational cost, as the movement of the rotor blades must be resolved all the way to the tips, requiring very small time steps in the order of 0.01 s for the calculations and a spatial resolution of at least 10 grid points per blade. Additionally, information along the blade, such as lift and drag coefficients and chord length, is required, which is also the case for an ADMR. These data are often not published by manufacturers, which is why studies frequently rely on generic turbines. The most commonly used turbines are the NREL 5MW turbine [Jonkman and Buhl Jr., 2005], along with the larger 15 MW IEA 15-240 RWT turbine [Gaertner et al., 2020].

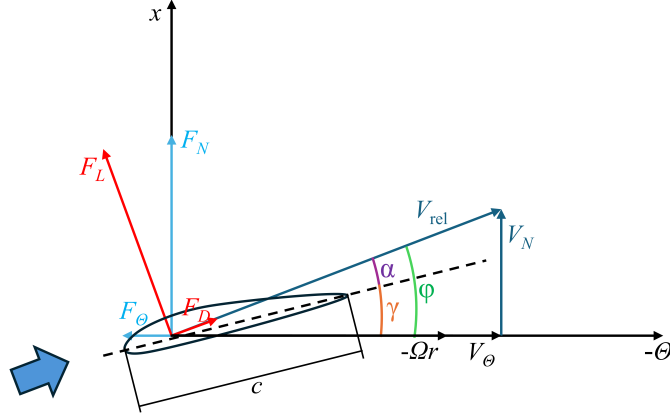


Figure 2.3: Schematic of the forces, velocities and angles at a blade element of a wind turbine, based on Troldborg [2008].

In Fig. 2.3 the forces, velocities and angles acting on an airfoil element are shown. Here, α denotes the angle of attack, γ the pitch angle, φ the flow angle and Ω the angular velocity.

Similar to the ADM-R the lift and drag forces can be calculated for a single blade element b with span-wise length Δr with the following equations:

$$F_L = \frac{1}{2} \rho_0 V_{\text{rel}}^2 c_L c \Delta r \quad (2.22)$$

$$F_D = \frac{1}{2} \rho_0 V_{\text{rel}}^2 c_D c \Delta r. \quad (2.23)$$

The relative velocity V_{rel} can be determined by looking at Fig. 2.3:

$$V_{\text{rel}} = \sqrt{V_N^2 + (\Omega r - V_\Theta)^2}, \quad (2.24)$$

where V_N and V_Θ are the axial and tangential velocities respectively. The flow angle φ can be calculated as:

$$\varphi = \tan^{-1} \left(\frac{V_N}{\Omega r - V_\Theta} \right). \quad (2.25)$$

For the transfer of forces into the axial and tangential plane, the following geometric formulas can be used:

$$F_N = F_L \cos(\varphi) + F_D \sin(\varphi) \quad (2.26)$$

$$F_\Theta = F_L \sin(\varphi) - F_D \cos(\varphi). \quad (2.27)$$

To avoid numerical discontinuities, the aerodynamic forces must be evenly distributed across multiple grid points to transfer the information from the blade positions to the LES grid points, ensuring that the integral over all points accurately reconstructs the blade forces. As mentioned in the ADM-R, this is achieved using a Gaussian shaped function. The distribution is performed using the regularization kernel η_ε according to the following function, based on [Sørensen et al. \[1998\]](#), [Trolborg \[2008\]](#):

$$f_\varepsilon = f \otimes \eta_\varepsilon, \quad \eta_\varepsilon(d) = \frac{1}{\varepsilon^3 \pi^{3/2}} \cdot \exp\left[-\left(\frac{d}{\varepsilon}\right)^2\right], \quad (2.28)$$

where d is the distance between the grid cell center and the blade element from which the respective force stems and ε is a factor of the grid size. Within the scope of this thesis it is set to $\varepsilon = 2\Delta$, with Δ being the grid size. The equation 2.28 serves as the foundation for the polynomial function utilized in the ADM-R method, which is computationally more efficient than this exponential function. However, within the scope of this thesis, the exponential formulation is employed, as the work is based on an ALM version that relies on the exponential representation.

The thrust and power coefficients $c_{T,P}$ can be calculated by putting the aerodynamic thrust/power $\mathcal{T}_{\text{aero}}/P_{\text{aero}}$ in relation to the total thrust/power $\mathcal{T}_{\text{total}}/P_{\text{total}}$. The aerodynamic thrust and power can be calculated by summing up the calculated forces for the blade elements b and the radius r , see the following equations:

$$c_T = \frac{\mathcal{T}_{\text{aero}}}{\mathcal{T}_{\text{total}}} = \frac{\sum_b \sum_r F_N \Delta r}{\frac{1}{2} \rho V_{\text{rel}}^2 A_{\text{disk}}} \quad (2.29)$$

$$c_P = \frac{P_{\text{aero}}}{P_{\text{total}}} = \frac{\sum_b \sum_r \Omega r F_\Theta \Delta r}{\frac{1}{2} \rho V_{\text{rel}}^3 A_{\text{disk}}}, \quad (2.30)$$

where A_{disk} denotes the area of the rotor disk.

ASM

Another option for turbine parameterization is the Actuator Sector Model (ASM). The aim of the ASM is to speed up the calculation time compared to the ALM, but to obtain more details than an ADM(-R). Depending on the implementation of the model, it is possible to obtain information about individual rotor blades with an ASM, while the calculation time is significantly less than with the ALM. The ASM parametrization allows for a larger time step compared to the ALM parametrization. The area covered by the rotor blade during the larger time step defines the sector. Consequently, the sector size depends on the rotor speed of the turbine and the LES time step. Various approaches can be employed for calculating forces and sampling wind speed within a sector [[Storey et al., 2015](#), [Krüger et al., 2022](#), [Mohammadi et al., 2024a](#)]. The schematic in Fig. 2.4 shows the approach of

dividing the sector into small blade movements according to an ALM and then calculating the forces per blade segment. This approach was developed as part of this thesis and can be found in the implementation of the PALM-FAST coupling, which is explained in Chapters 3, 4 and 5.

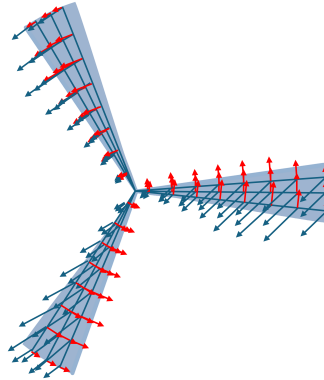


Figure 2.4: Schematic of the ASM wind turbine parameterization. The sector represents the area the rotor blades swipe within the LES time step. Different approaches for the calculation of the forces is possible. This schematic depicts one method, where the sector is subdivided into lines, allowing for the individual calculation of lift and drag forces for each segment, as indicated by the arrows.

Although there are various methods to sample wind speed within the sector and reintroduce the forces into the flow, the ASM parametrization is based on the same principles and formulas as the ALM. The forces are calculated based on airfoil data at specified segments. These forces are then introduced into the LES using a Gaussian-shaped function. For further details on the velocity sampling and force distribution see Chapters 3, 4 and 5.

2.2 FAST v8

The second code that was extensively used in the scope of this thesis is the aeroelastic code FAST v8 [Jonkman and Buhl Jr., 2005] developed by the National Renewable Energy Laboratory (NREL). The name FAST stands for Fatigue, Aerodynamics, Structures and Turbulence as it is an extensive tool to calculate these components with respect to wind turbines. FAST encompasses aerodynamic, control and structural dynamic (elastic) models to calculate the dynamic behavior of a wind turbine. There are numerous configurable options, such as the number of rotor blades (2 or 3), pitch or stall control, rigid or teetering hub, upwind or downwind rotor, and lattice or tubular tower. The inflow conditions can be entered in various formats to compute a time series of the turbine's response, including three-dimensional and time-varying atmospheric turbulence, as well as discrete gusts or steady mean wind speeds. Additionally, it is possible to conduct an eigenvalue analysis for the development of state matrices of a wind turbine to support the development and analysis of controllers or to determine the complete system modes.

The AeroDyn module [Moriarty and Hansen, 2005] of FAST contains code for calculating the aerodynamic lift and drag and pitching moments for segments along the rotor blade. Information about the turbine geometry is required for all aerodynamic calculations. AeroDyn continuously combines information such as blade-element velocity and position, turbine control, wind inflow from

the input files and data from the aeroelastic module of FAST. It offers various aerodynamic models to choose, the most relevant one being the wake models. Here, the options are the blade element momentum theory (BEM) and the generalized dynamic wake theory. The following section explains the BEM option, as it was utilized within the scope of this thesis.

2.2.1 Blade element momentum theory

In the BEM theory two approaches are being combined: the blade element theory and the momentum theory [Leishman, 2000]. The Blade Element Theory assumes that a rotor blade can be divided into segments, whereby ring segments are formed to subdivide the blades in a similar way to ADM-R, see Fig. 2.5. It is also assumed that these segments can be regarded as two-dimensional airfoils and that the aerodynamic forces per segment can be calculated and summed over the length of the blade.

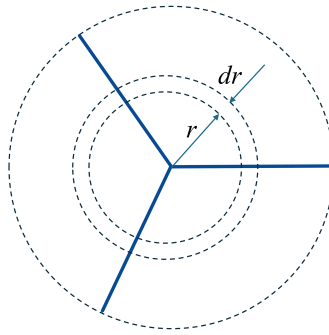


Figure 2.5: Schematic of the annular ring segments at distance r to the nacelle and width dr , based on Moriarty and Hansen [2005].

With the help of the momentum theory, both axial and tangential induction can be taken into account, as the pressure or momentum loss occurring in the rotor plane due to the work done by the airflow on the rotor blades is considered. The velocities at the rotor blades, which take induction into account, can in turn be used in blade element theory, resulting in an iterative process, combining both theories, for determining aerodynamic forces.

The following equation relates the flow angle φ to the velocities in the rotor system.

$$\tan \varphi = \frac{U_\infty(1-a)}{\Omega r(1+a)} = \frac{1-a}{(1+a')\lambda_r}, \quad (2.31)$$

where U_∞ denotes the mean wind speed, a the axial induction factor, a' the rotational or tangential induction factor, Ω the rotor speed, r the local radius and λ_r the local tip speed ratio. For a blade motion that is significant, the local element velocities due to the blade motion in-plane v_{e-op} and out-of-plane v_{e-ip} need to be included:

$$\tan \varphi = \frac{U_\infty(1-a) + v_{e-op}}{\Omega r(1+a) + v_{e-ip}}. \quad (2.32)$$

The induced velocity components from equation 2.32 are a function of the forces acting on the blades. The BEM can be used for their calculation. According to the blade element theory, the thrust force over a ring $d\mathcal{T}$ of width dr (see Fig. 2.5) is equal to:

$$d\mathcal{T} = B \frac{1}{2} \rho V_{\text{total}}^2 (c_L \cos \varphi + c_D \sin \varphi) c dr, \quad (2.33)$$

where B denotes the number of blades, ρ the air density, V_{total} the total velocity seen by the blade element, $c_{L/D}$ the lift and drag coefficient respectively and c the chord length. The torque of a blade element $d\mathcal{Q}$ with width dr can be described similarly:

$$d\mathcal{Q} = B \frac{1}{2} \rho V_{\text{total}}^2 (c_L \sin \varphi - c_D \cos \varphi) c r dr. \quad (2.34)$$

To calculate the thrust or torque of each blade segment as a function of the induction factor and the mean wind speed, the momentum theory can be used, which states that the thrust or torque per blade segment is equal to:

$$d\mathcal{T} = 4\pi r \rho U_{\infty}^2 (1 - a) a dr, \quad (2.35)$$

and

$$d\mathcal{Q} = 4\pi r^3 \rho U_{\infty} (1 - a) a' dr. \quad (2.36)$$

Information about the lift and drag coefficients as a function of the angle of attack is required as input, after which these formulas can be solved iteratively to calculate the induced velocities and forces per blade element.

Additionally, several corrections can be applied. For instance, FAST includes a tip- and hub-loss model that accounts for vortices shed in these positions, the Glauert correction for high induced velocities and the skewed wake correction for scenarios where the inflow is not perpendicular to the rotor plane.

Tip- and Hub Loss Correction

The vortex shedding at the tip has a major influence on the distribution of the induced velocity, but is not taken into account in the original BEM theory. FAST therefore implements a tip-loss correction based on a theory by Prandtl [Glauert, 1935]. The wake is assumed to be simplified by modeling the wake as vortex blades that are convected by the mean flow and have no direct influence on the wake itself. This theory can be expressed by a correction factor F to the induced velocity field as follows:

$$F = \frac{2}{\pi} \cos^{-1} e^{-f}, \quad \text{where } f = \frac{B}{2} \frac{R - r}{r \sin \varphi}, \quad (2.37)$$

with R being the rotor radius. This correction factor can be added to equations 2.35 and 2.36 as follows:

$$d\mathcal{T} = 4\pi r \rho U_{\infty}^2 (1 - a) a F dr, \quad (2.38)$$

and

$$d\mathcal{Q} = 4\pi r^3 \rho U_{\infty} (1 - a) a' F dr. \quad (2.39)$$

Similarly, the hub-loss model contains a correction factor to correct the induced velocity, here f of Eqn. 2.37 is given by:

$$f = \frac{B r - R_{\text{hub}}}{2 r \sin \varphi}. \quad (2.40)$$

Glauert Correction

In turbines with a high tip speed ratio, the induction factor a can exceed 0.5. According to momentum theory, this would imply that the flow is moving upstream, which is physically impossible. Instead, additional flow from outside the wake is introduced, increasing turbulence. The flow behind the rotor slows down, while thrust at the rotor disc continues to increase. To correct for this, [Glauert \[1926a\]](#) developed an empirical correction for the rotor thrust coefficient. This correction is closely linked to the tip loss model, as high losses near the tip can lead to higher induced velocities and a greater likelihood of turbulent wake formation. Therefore, both should always be activated. In [Buhl Jr. \[2004\]](#) a modification was developed to incorporate the tip-loss correction in the Glauert empirical relation as shown below:

$$c_T = \frac{8}{9} + \left(4F - \frac{40}{9}\right) a + \left(\frac{50}{9} - 4F\right) a^2, \quad (2.41)$$

rearranging for the induction factor gives:

$$a = \frac{18F - 20 - 3\sqrt{c_T(50 - 36F) + 12F(3F - 4)}}{36F - 50}. \quad (2.42)$$

Skewed Wake Correction

The skewed wake correction is necessary when the flow does not approach the rotor plane in an axisymmetric manner, as the BEM theory becomes invalid. The formula employed in AeroDyn to adjust the induction factor is derived from the work of [Glauert \[1926b\]](#), [Pitt and Peters \[1981\]](#), as follows:

$$a_{\text{skew}} = a \left[1 + \frac{15\pi r}{32 R} \tan \frac{\chi}{2} \cos \Psi \right], \quad (2.43)$$

where Ψ represents the azimuth angle, which is zero at the rotor's most downwind position after considering tilt and yaw and χ denoting the wake skew angle. The relationship between the wake skew angle χ and the yaw angle γ can be approximated [[Burton et al., 2001](#)] by:

$$\chi = (0.6a + 1)\gamma. \quad (2.44)$$

Iteration Process for BEM

To start the iteration process in AeroDyn, the axial induction factor is first calculated. The following assumptions are made: the inflow angle φ is small ($\sin \varphi \approx \varphi$), the tangential induction a' is zero, the tip and hub loss corrections F equal one, the drag coefficient c_D is zero, the lift coefficient c_L is given by $c_L = 2\pi\alpha$, and α is defined as $\alpha = \varphi - \beta$. This leads to:

$$a = \frac{1}{4} \left[2 + \pi \lambda_r \sigma' - \sqrt{4 - 4\pi \lambda_r \sigma' + \pi \lambda_r^2 \sigma' (8\beta + \pi \sigma')} \right], \quad (2.45)$$

where σ' is the local solidity, which can be expressed as $\sigma' = \frac{Bc}{2\pi r}$. From this point, the iterative process can begin, as shown in the flow chart in Fig. 2.6. The thrust coefficient is calculated in AeroDyn as follows:

$$c_T = \left[1 + \frac{\sigma' (1-a)^2 (c_L \cos \varphi + c_D \sin \varphi)}{\sin^2 \varphi} \right]. \quad (2.46)$$

After calculating the hub and tip losses, the induction factor a is recalculated, if necessary ($c_T > 0.96F$) using the Glauert correction (Eqn. 2.42), otherwise according to the BEM theory:

$$a = \left[1 + \frac{4F \sin^2 \varphi}{\sigma' (c_L \cos \varphi + c_D \sin \varphi)} \right]^{-1}. \quad (2.47)$$

Similarly, the tangential induction factor is calculated:

$$a' = \left[-1 + \frac{4F \sin \varphi \cos \varphi}{\sigma' (c_L \sin \varphi + c_D \cos \varphi)} \right]^{-1}. \quad (2.48)$$

This process is repeated for each blade element, beginning again with the calculation of the flow angle (Eqn. 2.32), and continues iterating until the induction factors and inflow angle converge to their final values.

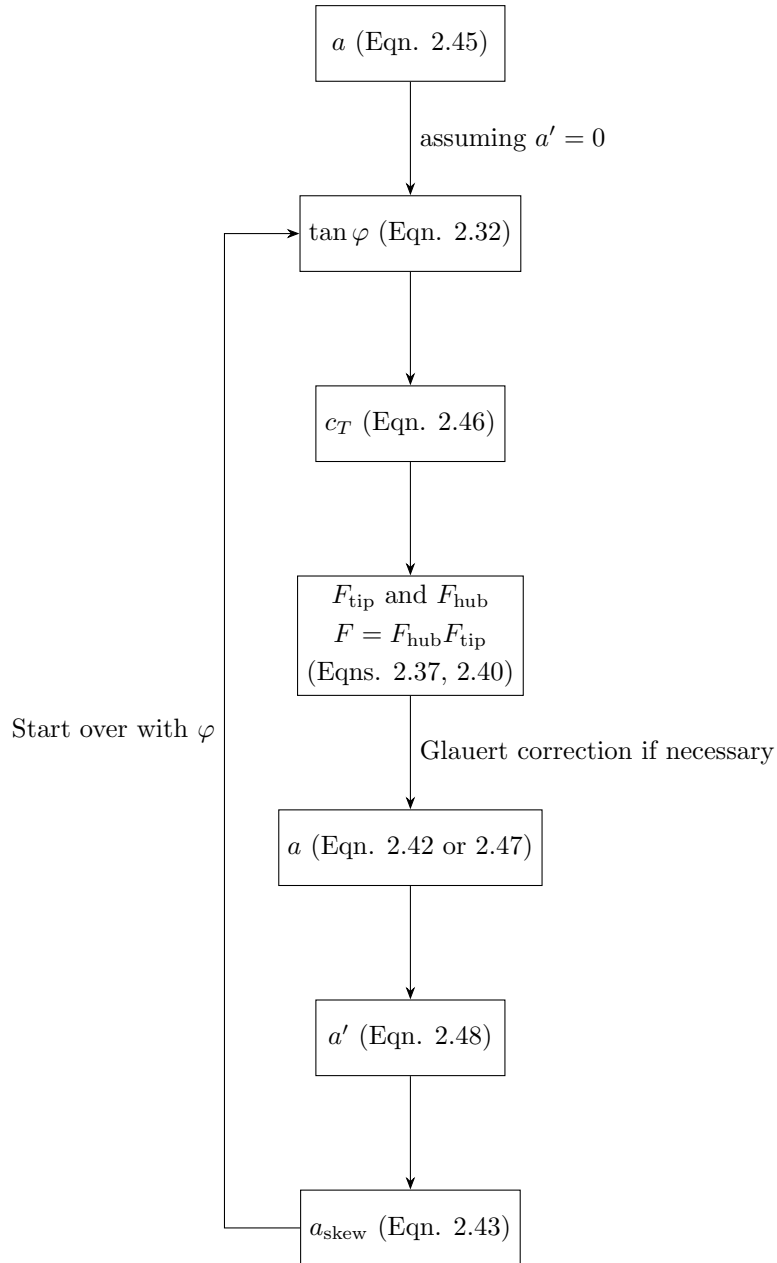


Figure 2.6: Flow chart of the iterative BEM process as implemented in AeroDyn.

2.3 Near wake correction

When parameterizing wind turbines using ALM, implementations without further corrections tend to overestimate power and loads. This issue is well-documented, and several strategies have been explored to mitigate it, like e.g. [Martínez-Tossas et al. \[2017\]](#), [Shives and Crawford \[2013\]](#), [Jha et al. \[2014\]](#). Among these, the approach proposed by [Dag \[2017\]](#) and realised by [Meyer Forsting et al. \[2019, 2020\]](#) will be discussed in this section, it is denoted as Near-wake correction (NWC) within the scope of this thesis.

The ALM is based on the lifting-line theory (LLT) developed by [Sørensen and Shen \[2002\]](#). A key difference between the simulations and the LLT is that the blade forces are spatially smeared to avoid numerical instabilities. This smearing of forces within the flow domain results in reduced induction at the rotor blades, which, in turn, increases lift and drag. [Dag \[2017\]](#) examined this discrepancy between ALM with the LLT and proposed a correction.

The force smearing in an ALM leads to the formation of vortices with relatively large viscous cores, resulting in an underestimation of axial induction. This relationship between force smearing and the viscous cores of trailing vortices was investigated by [Shives and Crawford \[2013\]](#). Their suggested improvements did not address the underlying problem, which is needed for smaller vortex cores in the ALM.

[Dag \[2017\]](#) investigated the viscous core effects in an ALM simulation in comparison to a lifting line computation of a rectangular wing. These comparisons indicate that the results of the ALM increasingly align with those of the lifting-line calculations as the smearing coefficient ε decreases. This suggests that induction increases with a lower ε . Additionally, [Dag \[2017\]](#) found that ε is related to the core size of the generated vortices. However, the resulting notion of reducing ε promises few advantages, as this leads to numerical instabilities. Instead, [Dag \[2017\]](#) aims to find a correction that addresses the gap in wake induction caused by the viscous vortex cores. To achieve this, a viscous core model is defined that analytically links the vortex core size to the ε value. The Lamb-Oseen vortex model [[Lamb, 1932](#), [Oseen, 1911](#)] is particularly suitable for this purpose, as it produces an induction profile similar to that of a vortex generated by a defined body force in an ALM computation. The following equation describes this relation:

$$w_i = \frac{\Gamma}{2\pi r} \left(1 - \exp\left(\frac{-r^2}{r_{vc}^2}\right) \right), \quad (2.49)$$

where Γ denotes the vorticity, r the distance to the induction point from the center of the vortex and r_{vc} the viscous core radius. The first term represents the inviscid component of the induction, while the second term reflects the effect of the viscous core. A notable finding of [Dag \[2017\]](#) is that by using $r_{vc} = \varepsilon$, the exact same induction as observed in the ALM computation can be achieved. The missing induction caused by the presence of an artificial viscous core can now be analytically estimated: When comparing the induction profile represented by the Biot-Savart law, which assumes no vortex core, with the induction profile that includes a viscous vortex core, the difference illustrates the missing induction in an ALM simulation. Leading to the following analytical formulation, where the Lamb-Oseen vortex induction is subtracted from the Biot-Savart induction, representing the missing induction:

$$w_{\text{corr}} = \frac{\Gamma}{2\pi r} - \frac{\Gamma}{2\pi r} \left(1 - \exp\left(\frac{-r^2}{\varepsilon^2}\right) \right) \quad (2.50)$$

$$= \frac{\Gamma}{2\pi r} \left(\exp\left(\frac{-r^2}{\varepsilon^2}\right) \right). \quad (2.51)$$

A theoretical derivation of the relationship between the Lamb-Oseen vortex and the Biot-Savart law, based on the incompressible Navier-Stokes equation, can be found in [Meyer Forsting et al. \[2019\]](#). In [Meyer Forsting et al. \[2019\]](#), the correction found by [Dag \[2017\]](#) is also implemented in an ALM.

Equation 2.50 can be split into an inviscid and a viscous part. The first term representing the inviscid part:

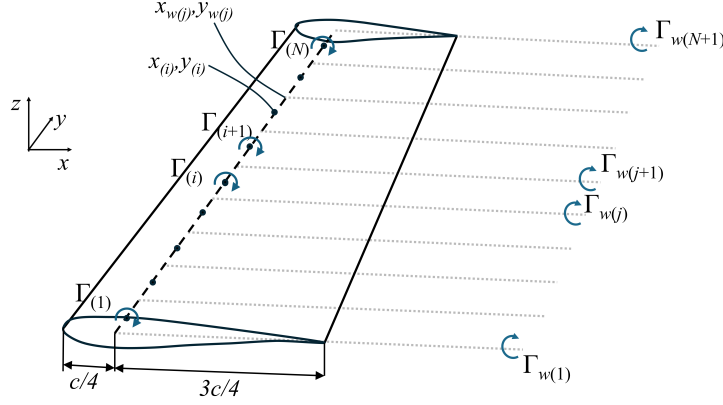


Figure 2.7: Schematic of the trailing vortices at a planar wing, based on [Dag \[2017\]](#). N denotes the total number of actuator line points and Γ the strength of the vortices.

$$v_{\Theta}(r) = \frac{\Gamma}{2\pi r}, \quad (2.52)$$

and the viscous being:

$$f_{\varepsilon}(r_{\varepsilon}) = \exp\left(\frac{-r^2}{\varepsilon^2}\right). \quad (2.53)$$

When applied to an ALM, the velocity correction leads to a velocity correction vector in three-dimensional space. The behaviour described, which is caused by the force smearing, is transferred from the boundary vortex zone to the trailing vortices, which in turn leads to a reduced induction. Figure 2.7 shows the diagram of the trailing vortices that arise between two sections. Their strength is described by Γ_w and their magnitude can be calculated by computing the difference between two neighboring circulations $\Delta\Gamma = \Gamma_{(j)} - \Gamma_{(j-1)}$.

The strength of the bound circulation depends on the chord length c , relative velocity u_{rel} and the lift coefficient c_L :

$$\Gamma_{(i)} = \frac{1}{2}c_{(i)}c_{L(i)}u_{\text{rel}(i)}. \quad (2.54)$$

The missing induction from a single trailed vortex at a point C can be calculated by integrating along the vortex line:

$$u^* = \int_0^{\infty} f_{\varepsilon}\delta\tilde{u}dl. \quad (2.55)$$

The vorticity moves away from the blade along the vortex line l due to the blade's rotation and downwind convection, further influencing the wind speed at the rotor blade. Considering a vortex element δl along this line, the induced velocity at a control point C on the blade is represented as $\delta\tilde{u}$. The induction from this vortex element can be calculated using the Biot-Savart law, taking into account the relevant geometric considerations:

$$\delta\tilde{u} = \frac{\Delta\Gamma}{4\pi} \frac{\delta l \times x}{|x|^3}, \quad (2.56)$$

where x denotes the vector pointing from the element towards the point C , where the induced velocity is being calculated. The smearing factor f_ε for the vortex element is defined as:

$$f_\varepsilon = \exp\left(-\frac{(x\hat{e}_\perp)^2}{\varepsilon^2}\right). \quad (2.57)$$

The viscous core operates only in the plane perpendicular to the vortex element δl , so \hat{e}_\perp projects x onto this plane. This differs from [Dag \[2017\]](#), who suggested using the distance $|x|$, which does not respect the two-dimensional nature of the viscous core. The total missing induction at a blade section s is calculated by adding up the contributions from all the trailed vortices. By discretizing the vortices over time, the missing induction at a specific blade section can be expressed as:

$$u_s^* = \sum_v^{N_v} \sum_n^{N_t} f_{s,v}^n \Delta \tilde{u}_{s,v}^n, \quad (2.58)$$

where v is the trailed vortex index, n the time index and N_t the number of time steps. In order to have a computational feasible way to compute the Biot-Savart component $\tilde{u}_{s,v}^n$, [Meyer Forsting et al. \[2019\]](#) proposes to use the near-wake model for trailed vorticity by [Pirrung et al. \[2016, 2017b\]](#), which can be computed as follows:

$$\tilde{u}_{s,v}^n = (X_{s,v}^n + Y_{s,v}^n) \begin{bmatrix} 0 \\ \sin(\phi^n) \\ -\cos(\phi^n) \end{bmatrix}, \quad (2.59)$$

where ϕ denotes the helix angle of the vortex shed. The indicial functions are expressed in the following manner:

$$\{X_{s,v}^n + Y_{s,v}^n\} = a_{\{X,Y\}} \frac{r_v}{4\pi h_s |h_s|} \Delta \Gamma_v^n \phi_{s,v}^{*n} \left[1 - \exp\left(-b_{\{X,Y\}} \frac{\Delta \beta^{*n}}{\phi_{s,v}^{*n}}\right) \right] \exp\left(-b_{\{X,Y\}} \sum_i^{n-1} \frac{\Delta \beta^{*i}}{\phi_{s,v}^{*i}}\right) \quad (2.60)$$

For the definitions of $a_{\{X,Y\}}$, $b_{\{X,Y\}}$, β^* , and ϕ^* refer to [Pirrung et al. \[2016, 2017b\]](#).

The application of the correction affects the blade forces via the angle of attack and the magnitude of the speed. This changes the circulation on each blade, which in turn changes the vortex shedding. The correction process is therefore iterative, as shown in the flow chart in [Fig. 2.8](#).

To expedite the iterative process described, an accelerated version is presented in [Meyer Forsting et al. \[2020\]](#). The code is freely available to be implemented in ALM computations.

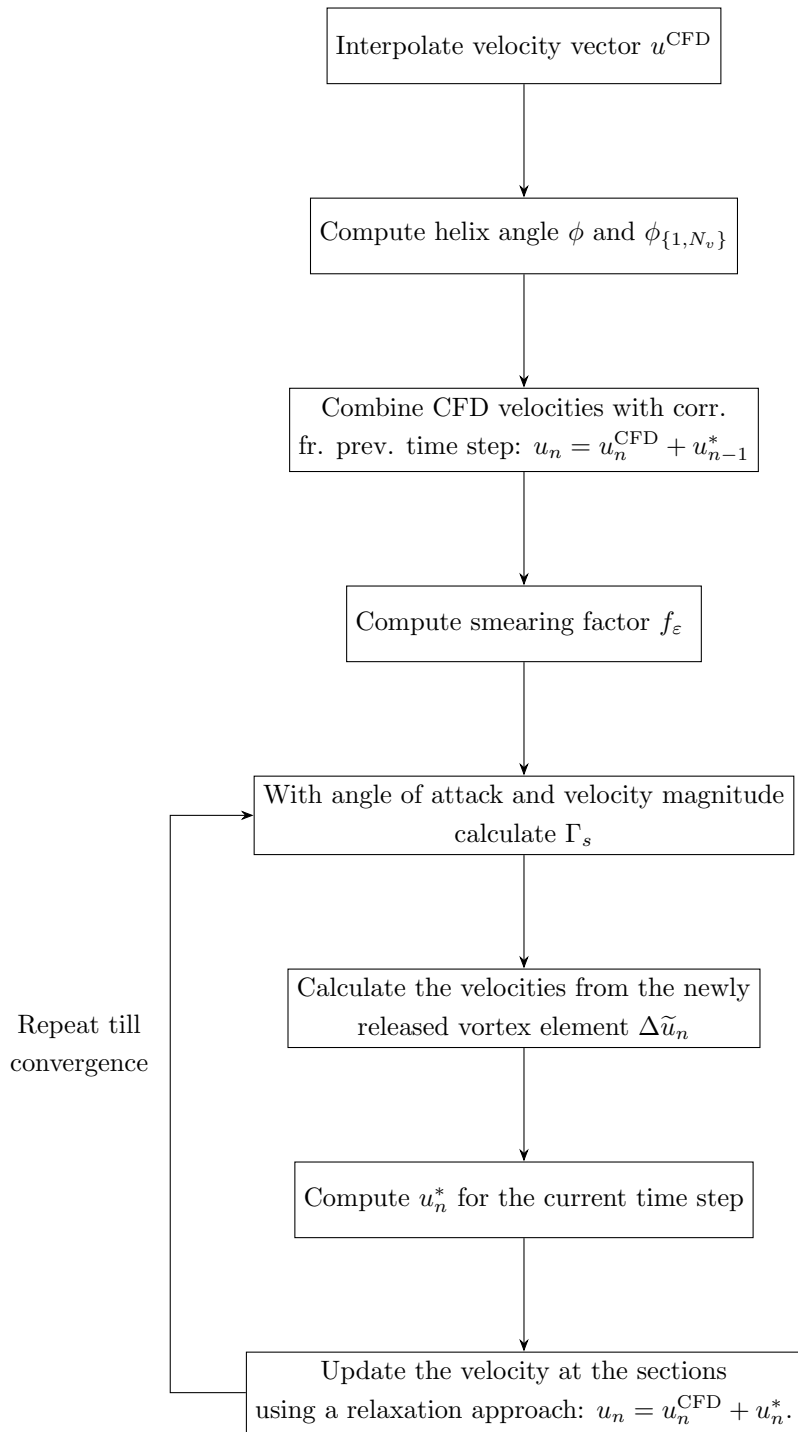


Figure 2.8: Flow chart of the iterative process of the NWC as described by Meyer Forsting et al. [2019]

Chapter 3

Newly developed method: PALM-FAST coupling

This chapter serves as an introduction to the technical details of the coupling of the PALM and FAST models, developed within the scope of this thesis. It aims to present technical insights that complement the descriptions in the subsequent chapters. In the context of this thesis, the models described in Sections 2.1 to 2.3 have been coupled. This combination enables the simulation of atmospheric flows with a wind turbine while providing a detailed and accurate representation of the turbine and its responses. Additionally, this approach is computationally efficient due to the implementation of the coupling as an ASM within the PALM framework.

The coupling is based on the work of [Bromm et al. \[2017\]](#), in which FAST v7 was coupled with PALM with a coupled time step, i.e. FAST and PALM have the same time step. As FAST requires a very small time step for the BEM calculation, this coupling was very time- and resource-consuming. In addition, there was no correction of the wind speeds as for example described in the Section 2.3.

The evolution from the coupling version by [Bromm et al. \[2017\]](#) to the current version encompasses several significant changes. Firstly, the code was upgraded from FAST v7 to the module-based FAST v8. From now on FAST denotes the version FAST v8. Secondly, a major advancement was the development of an ASM-based version, which greatly enhances computational efficiency. Thirdly, it was necessary to address the issue of power overestimation. This thesis explores two approaches: the ASM SWIRL variant detailed in Chapter 4, and the ASM NWC variant, which is elaborated upon in Chapter 5.

The general approach to couple PALM and FAST is sketched in Fig. 3.1. Both models offer distinct information and advantages that can be effectively integrated in a simulation through coupling. PALM and FAST are both implemented in Fortran and are publicly accessible. The coupling of these two programs is achieved through an interface developed in C, utilizing a TCP/IP connection for communication. PALM is a parallelized program that operates across multiple computing nodes, whereas FAST runs on a single node, allowing access via a single IP address.

To establish the connection, this IP address must be configured on the PALM side, and a communication port must be defined on both sides, which corresponds to the specific turbine ID. Consequently, when simulating multiple instances of FAST, different turbine IDs must be assigned, each associated with a unique port number. Initially, communication is established before the first time step begins. The functions that retrieve information from the FAST side are initiated on the PALM side. First, static information is gathered, including air density, the number of turbine blades and blade elements, rotor radius, and the simulation end time specified in FAST. Following this, the

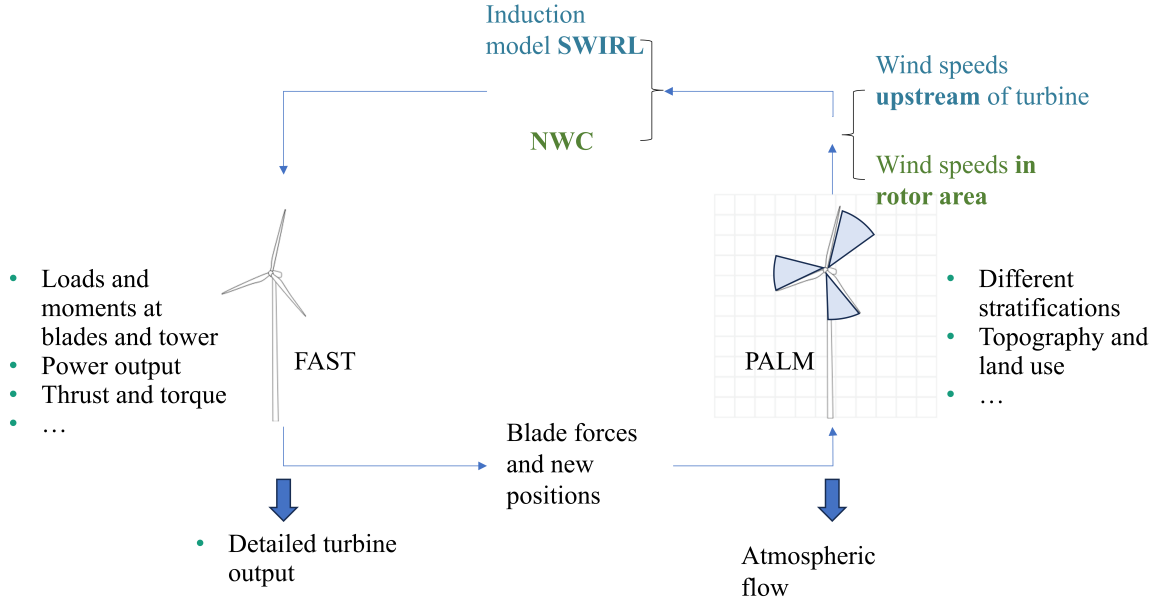


Figure 3.1: Overview of the PALM-FAST coupling methods. The options for wind speed sampling and corrections are written in color, blue representing the ASM SWIRL option and green the ASM NWC.

blade positions, rotor speed, and current time are transmitted from FAST to PALM. The rotor speed is essential for determining the sector size of the ASM in PALM, while the blade positions indicate where the wind speeds are sampled within the PALM wind field.

The blade positions are added to the turbine's x and y coordinates in PALM to determine their horizontal positions within the PALM grid. In the vertical direction, the blade positions already incorporate the turbine height from the FAST configuration, eliminating the need to specify hub height in PALM. Consequently, calculations in FAST are performed within its own coordinate system. The blade positions and forces calculated in FAST are stored in arrays of size $n_{bl} \times n_{el}$, where n_{bl} is the number of rotor blades and n_{el} is the number of elements per blade. This forms look-up tables for retrieving corresponding values according to the blade element number. When transferring forces from FAST to the PALM model area, it is crucial to select the correct coordinate system. FAST utilizes different reference systems for calculations, as detailed in [Jonkman and Buhl Jr. \[2005\]](#). For the coupling, the forces in FAST have therefore already been saved according to the PALM coordinate system for transfer to PALM.

When implementing the coupling with ASM in PALM, both the small time step and the BEM, or a blade element approach, are retained in FAST for accurate calculations. This allows for multiple FAST time steps to be computed within a PALM sector, with forces transferred from FAST to PALM during these shorter FAST time intervals. The FAST forces from these smaller time steps are smeared and applied at their respective positions within the PALM sector using the Gaussian shape (see equation 2.28 in Section 2.1.2), effectively composing a PALM sector of several FAST lines. It is essential to normalize the forces by the number of FAST steps within a PALM time step; otherwise, the forces will be significantly overestimated. Further distinctions and details about the methods can be found in the subsequent Chapters 4 and 5.

Chapter 4

Validation of a coupled atmospheric–aeroelastic model system for wind turbine power and load calculations

This chapter includes results that were published in the following journal article (authored under my maiden name): Krüger, S., Steinfeld, G., Kraft, M., Lukassen, L. J. (2022). Validation of a coupled atmospheric-aeroelastic model system for wind turbine power and load calculations. *Wind Energy Science*, 7(1), 323–344. <https://doi.org/10.5194/wes-7-323-2022>

While the methods and results sections remain identical to the publication, the introduction has been moved to an earlier section of the thesis and has been rewritten, while the conclusion has also been rewritten to better align with the overall flow and topic of the thesis, facilitating its integration into the broader context of the work.

Contributions: I updated the existing ALM coupling to the at the time of the work latest versions of FAST and PALM, developed and implemented an ASM method within PALM and conducted thorough testing of the framework. Additionally, I performed simulations, analyzed the results, created plots to visualize the findings, wrote the first draft and integrated corrections based on linguistic and content-related feedback.

The work presented in this Chapter was completed in 2022 and focuses on the development of one of the earliest variants of an ASM. Consequently, the literature reviewed and referenced in this chapter is limited to publications available up to that year, reflecting the knowledge and advancements in the field up to that point. Subsequent developments are not covered in this chapter. This work was conducted prior to my absence due to parental leave.

To address the challenge of simulating dynamic turbine behavior in atmospheric flow, as mentioned in Chapter 1.2, and to offer a dependable tool for detailed turbine analysis, a comprehensive computational framework is presented in this chapter. This framework enables the coupling of the LES tool PALM with the aeroelastic model FAST, allowing the calculation of not only turbine power output but also detailed quantities along the blades and for individual blade components in an atmospheric flow.

The enhanced coupling method presented in this chapter is systematically validated against measurement data under varying atmospheric conditions. The evaluation of the coupling within this chapter includes simulations of the generic NREL 5 MW turbine to compare turbine output and computational efficiency across different models. To further validate the coupling and assess result quality, a non-generic turbine located in northeast Germany is also simulated and compared against measurement data. These comparisons confirm that the PALM–FAST coupling produces realistic turbine output parameters for statistically stationary atmospheric flows, capturing both global parameters, such as power output, and local parameters, such as blade and tower loads. Additionally, the simulations demonstrate variations in turbine behavior under different atmospheric conditions, offering valuable insights into turbine performance.

4.1 Methodology: the PALM–FAST coupling

In the present work, the aeroelastic turbine code FAST [Jonkman and Buhl Jr., 2005], developed at the National Renewable Energy Laboratory (NREL), USA, and the large-eddy simulation (LES) tool PALM [Maronga et al., 2015, 2020], developed at the Institute for Meteorology and Climatology (IMUK) of Leibniz University Hannover, are coupled. In addition to the power output FAST provides extensive information about the turbine response to the incoming flow, i.e. individual blade and tower loads, rotor speed, etc. PALM enables the simulation of an atmospheric flow for a wide range of different situations, like different stabilities using heating or cooling of the surface. It is based on the non-hydrostatic, filtered, incompressible Navier–Stokes equations in Boussinesq-approximated form and has seven prognostic quantities: the wind speed on a cartesian grid (u , v and w), the potential temperature (Θ), the water vapour mixing ratio (q_v), a passive scalar (s) and the subgrid-scale turbulent kinetic energy (e). The domain is divided into equidistant cells in the horizontal direction; stretching of the cells is possible in the vertical direction. To define the position of the quantities, the Arakawa staggered C-grid [Harlow and Welch, 1965, Arakawa and Lamb, 1977] is used.

An earlier version of the coupling between FAST and PALM, described in Bromm et al. [2017], was used here as a basis to be extended with respect to decreasing the computational time and improving the quality of the results. The previous implementation from Bromm et al. [2017] was based on an ALM and required small time steps in both FAST and PALM. Also, it used the wind speeds at the rotor disk for calculation in FAST.

In an ALM the rotor blades are simulated as moving lines in the model domain and require a small computational time step in order to calculate the movement and in order not to miss information at the fast-moving blade tips. As the movement of the blades is reproduced, an ALM can give information on the turbine in general but also on separate blade data like blade loads. A more computational time-saving option is to simulate the turbine rotor as a disk, which is done in ADM simulations. Additionally to the obstruction the rotor causes for the flow, a rotation can be added to the simulation (ADMR), which increases the quality of the wake simulation. However, no information about individual blade parameters can be gained in such a simulation. To combine the advantages of both kinds of turbine models, i.e. the detailed output of the ALM and the low computational costs of the ADMR, a so-called actuator sector method (ASM) is used in this work.

PALM, when run in a normal set-up without FAST, uses either the Courant–Friedrichs–Levy (CFL) criteria or the diffusion criteria to determine the largest possible time step, which in general is larger than a time step needed for a proper ALM simulation. Therefore, using the same time step in

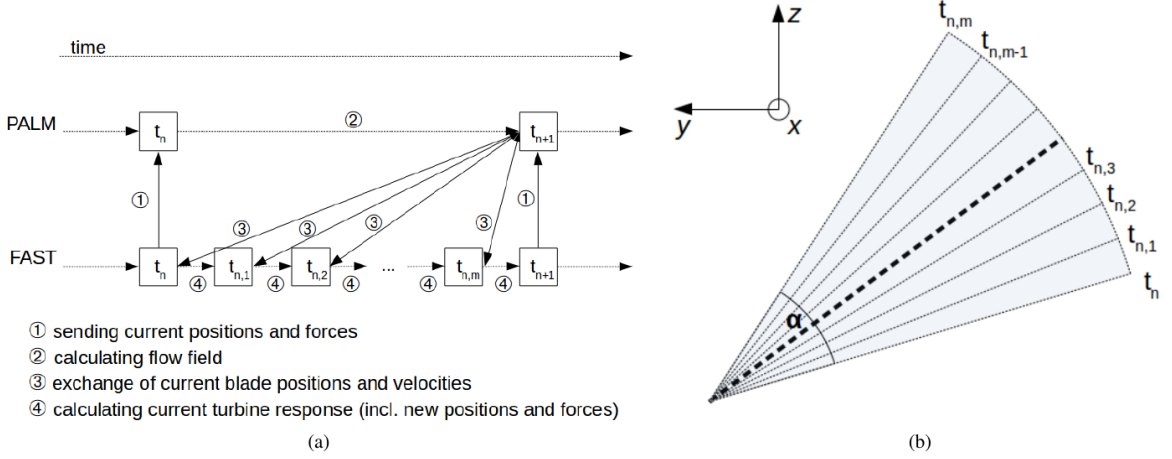


Figure 4.1: Schematic of the operation mode of the PALM–FAST ASM coupling. **(a)** Schematic of the PALM and FAST time stepping. **(b)** Schematic of one circle segment of the ASM. The values of the bold central line are used for the projection of the forces into the flow. Here, y and z denote the rotor plane and x the streamwise direction.

both FAST and PALM affects the computational time required for the LES. In the present work, we decouple the time step and allow the pure LES time step criteria (CFL and diffusion criteria), which were mentioned above, to determine the time step in PALM and with this reduce the total computational time significantly.

In more detail, we use an ASM model for the projection of forces in PALM, whereas in FAST we still use the ALM model. Through this set-up, the computing time can be reduced tremendously, since the more time-consuming operations take place in PALM and not in FAST. However, for simplicity, our whole coupling routine described in this work is simply abbreviated as ASM hereafter.

Our ASM works as follows (see Fig. 4.1a): while FAST carries out small time steps Δt_F as is necessary in an ALM, PALM uses its own time step $\Delta t_P > \Delta t_F$ determined by the atmospheric model time step criteria. The simulation starts with FAST communicating the initial blade positions. The wind speeds at these positions are determined from the wind fields simulated by PALM and sent back to FAST. PALM then carries out one time step and is ahead in the simulation. Once PALM has calculated its time step, the wind field is frozen and provides FAST with the wind speeds that are needed while FAST catches up and calculates up to the current simulation time in PALM.

FAST therefore receives wind speeds of this frozen wind field and calculates the responding forces for the blades. During the larger PALM time step, the rotor blades cover a segment of the rotor area, a sector. The width of the sector α is calculated by the PALM time step Δt_P and the rotor speed Ω , which the FAST model communicates to PALM at the beginning of the PALM time step, using $\alpha = \Omega \cdot \Delta t_P$. During the time step of PALM, several calculations of FAST are performed, similar to the schematic in Fig. 4.1b. Except the values of the bold central line, the information of the forces at the positions of the neighbouring lines is not used in PALM but is output in FAST. The values of the bold central line are used for all of the m lines in the sector, as in Fig. 4.1b. For each line a Gaussian-shaped smearing is calculated and projected into the model domain.

This smearing of the forces is realised by a polynomial resulting in a Gaussian shape that distributes the forces over the area surrounding the rotor blade in all three direction of space

(Sørensen et al., 1998):

$$\eta = \frac{1}{\varepsilon^3 \pi^{3/2}} \cdot \exp \left[- \left(\frac{r}{\varepsilon} \right)^2 \right], \quad (4.1)$$

where η is the so-called regularisation function which is applied at the nodes of the grid within a certain vicinity of the turbine, r is the distance between the respective node and the blade element from which the respective force stems, and ε is a factor of the grid size that is typically set to $\varepsilon = 2 \cdot \Delta$ [Troldborg, 2008], with Δ being the grid size.

In general, the forces acting on the blades are calculated based on the wind speed that is present at the blade position, i.e. the positions in the rotor plane. However, this wind speed does not represent the actual wind speed entirely as it depends on the grid resolution and has to be interpolated to the desired positions. Close to the last known blade positions this interpolation leads to higher wind speeds than in reality, which leads to an overestimation of the power output. Additionally, the projection width of the forces, i.e. the width defined by the regularisation function, influences the wind speed close to the blade immensely. To circumvent these issues, we take the wind speeds for the ASM in positions upstream of the turbine.

Far enough upstream of the rotor, the flow can be assumed to be almost undisturbed by the rotor. The wind speeds at the rotor area are then estimated using the induction model SWIRL of FAST. SWIRL uses the so-called Taylor frozen turbulence hypothesis (Taylor, 1938) and calculates the induced velocity in axial and tangential direction. In Moriarty and Hansen [2005] the AeroDyn model of FAST is described, including the blade-element momentum theory to compute the induction. The calculation of the induction factors when using SWIRL is based on Harman [1994]. With enabling SWIRL we assume that the turbulent structures in the wind field do not change while moving to the turbine. In the current coupling a temporal change of the wind field as it approaches the rotor is not included. A comparison of different approaches, including the enhanced coupling described here, was done in Doubrawa et al. [2020] to simulate site-specific behaviour of a turbine. Besides LES, the discussed models also included Reynolds-averaged Navier–Stokes (RANS) simulations and were compared with respect to turbine output and wake data in different atmospheric stabilities. The models performed differently depending on the simulation of the inflow conditions and the resolution used. Especially for the neutral case our coupling showed very good results.

4.2 Validation

The validation of the coupling is divided into two parts. The first part is the evaluation of results using the generic NREL 5 MW turbine. The second part is the comparison to measurement data for a more extended analysis, for which a non-generic turbine is simulated.

4.2.1 Evaluation of the coupling on the basis of the generic NREL 5 MW turbine

The NREL 5 MW turbine [Jonkman et al., 2009b] is a generic turbine which has been used extensively in simulations [Churchfield et al., 2012, Storey et al., 2013, 2015, Vollmer et al., 2016, Sathe et al., 2013, Lee et al., 2012]. The NREL 5 MW turbine was developed by the National Renewable Energy Laboratory (NREL), and a FAST model of the turbine is included in the FAST repository.

Table 4.1: Overview of the turbine models that were used in the comparisons. The new enhanced coupling method is ASM, the respective time steps in PALM and FAST are denoted as Δt_P and Δt_F respectively, and the inflow wind speed is denoted as U . The coupled model that is the focus of this paper is highlighted in bold.

Name	Time step	Wind speed information	Rotor model in PALM
ALM	coupled time step: $\Delta t_P = \Delta t_F$	U taken at positions of rotor blade elements in PALM	line
ASM without SWIRL	decoupled time step: $\Delta t_P = n \cdot \Delta t_F$	U taken at positions of rotor blade elements in PALM, from a frozen wind field	sector
ASM	decoupled time step: $\Delta t_P = n \cdot \Delta t_F$	U taken upstream of the rotor blade positions in PALM and use of the induction model SWIRL of FAST	sector
FAST	only FAST Δt_F	steady wind case in FAST, no LES	–

As this is a generic turbine, no comparison with measured data is possible. But the availability of the turbine data allows an evaluation of our enhanced coupling method, also in terms of turbulent flows. Additionally, the availability of the turbine data offers the opportunity to compare different methods and their computational resources. Therefore, two cases were considered, firstly a laminar and secondly a turbulent flow.

A comparison of four different methods is made, as summarised in Table 4.1. This includes a transient coupling between FAST and an ALM in PALM, meaning the same time step size in FAST and PALM (abbreviated as ALM). Furthermore, the ASM with two different modes of retrieving the wind speed is used, namely the ASM with the described method of reading out wind speeds in front of the turbine in combination with the induction model SWIRL (denoted as ASM), as well as taking the wind speeds at the rotor area without any induction model (denoted as ASM without SWIRL). As the fourth method, just in the laminar case, FAST on its own is used (denoted as FAST). For FAST on its own, the inflow wind option is set to match the PALM simulations; i.e. the power law variables are set to a wind speed of 8 m s^{-1} constant with time and with height.

To evaluate the different methods, at first, a laminar case with a constant wind speed with height, i.e. zero vertical gradient of the streamwise velocity, is considered. The LES simulations use a resolution of 5 m and 384×192 grid points in the flow direction and perpendicular to the flow direction. In the vertical direction, 192 grid points and a stretching are used, resulting in a total domain height of 3359 m. A larger model domain of 384 grid points perpendicular to the flow direction was tested as well to determine whether the size of the model domain influences the results. However, no significant differences in the conditions of the flow in the turbulent case (i.e. a deviation of 2% in the wind speed at 92 m) or the turbine output were detected, and therefore the smaller model domain was used for the simulations. The boundary conditions at the inflow and

outflow are set to cyclic; however, only the time at which the wake does not affect the inflow yet was evaluated. Additionally, the surface condition is set to a free-slip condition. PALM offers different possibilities for the subgrid-scale turbulence closure. For the simulations mentioned in this work the default model was used, which is a modified version of Deardorff’s subgrid-scale model [Deardorff, 1980], as mentioned in Moeng and Wyngaard [1988] and Saiki et al. [2000]. The time stepping and advection schemes were used in the default settings as well, which is a third-order Runge–Kutta scheme [Williamson, 1980, Baldauf, 2008] for time stepping and a fifth-order upwind scheme, based on Wicker and Skamarock [2002], for the advection. The pressure solver was set to the multigrid option [Uhlenbrock, 2001]. The wind speed in the flow is set to 8 m s^{-1} . The inflow conditions for FAST are set accordingly. The standard controller of the NREL turbine is employed as described in Jonkman et al. [2009b], which means that at the prevailing wind speeds no pitching of the blades is enabled.

In Fig. 4.2, a comparison of the generator power for the generic 5 MW NREL turbine is shown. The ALM and ASM without SWIRL result in too high a power output, which is assumed to be, most importantly, due to the wind speeds used to calculate the blade response which is taken in the rotor plane. A further difference can be seen in the projection of the forces, which leads to different shapes of the simulated rotor. As described above, in the rotor area there is the danger of reading out velocity values that are too large. The ASM bypasses this issue by using the SWIRL induction method and results in a generator power which corresponds well with the expected one. The ASM without SWIRL shows an even higher power output than the ALM. The reason for that may be that in the ASM without SWIRL the area that is blocked in the rotor area is larger than for ALM, which might result in higher wind speeds in between the sectors, like a nozzle. As the wind speeds next to the projected forces are used to calculate the turbine response, these higher wind speeds would lead to a higher power output.

A comparison of quantities along the 62 blade nodes shows a difference between the methods using wind speeds at the rotor blade positions (ALM and ASM without SWIRL) and the two methods using a different inflow, namely ASM and FAST (figures can be seen in Appendix A.1). The distribution of the angle of attack shows a smoothed curve for the ALM and ASM without SWIRL, which is due to the smearing of the forces around the rotor blades. On the other hand ASM and FAST show a choppy curve due to the different airfoil profiles along the blade; here, it can be seen at which position a change of an airfoil profile and twist angle along the blade is predefined in the NREL model. These differences are transferred to the lift and drag coefficients. Additionally, for dynamic pressure, it can be observed that ALM and ASM without SWIRL overestimate the dynamic pressure at the blade tips and slightly underestimate it at the hub compared to FAST and ASM. These observations suggest that the smearing of the forces has a great influence on the lift and drag properties and thus the turbine response.

As a second case a turbulent flow is calculated. However, no comparison to FAST alone is done here since there is no literature value available to compare the results with. For the turbulent case, a neutral flow is simulated with neither heating nor cooling of the surface. A resolution of 4 m is used with 1200×480 grid points in the flow direction and perpendicular to the flow direction. In the vertical direction 192 grid points and a vertical stretching are used again, resulting in a vertical height of 1728 m. The roughness length is set to 0.05 m; the wind speed at hub height is about 7.4 m s^{-1} . In this simulation non-cyclic boundary conditions are used. If cyclic boundary conditions were used, the wake of the turbine would be fed into the inflow again and would, therefore, distort the flow in

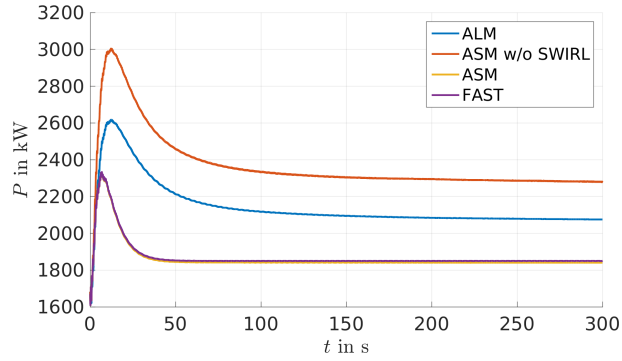


Figure 4.2: Comparison of different simulation methods for the generator power of the 5 MW NREL turbine in a laminar flow with 8 m s^{-1} wind speed.

front of the turbine. In order to avoid this, PALM offers the opportunity of non-cyclic boundary conditions and a turbulence recycling method; for more information, see [Maronga et al. \[2015\]](#).

Figure 4.3 shows the time series of the generator power. The wind speeds in the ASM are taken 2D in front of the turbine, which in this example is a distance of 252 m, resulting in a time shift of the flow reaching the turbine of about 34 s. Therefore, when comparing the turbine output the result of the ASM simulation is shifted by 34 s for a better comparison to the other results. This does not affect the statistics but is a simple method to make the time series obtained from the different models comparable to each other. A model or tool that automatically fixes this time shift is not included in the current version of the coupling.

As for the laminar case, the ASM leads to a lower power output than the other models, whereas the differences are comparable to the laminar case in Fig. 4.2. Also, roughly the same peaks and therefore structures of the flow are present in the ASM results. This indicates that the coupling also works in a turbulent environment insofar as the turbulent structures are reflected in the power output.

Furthermore, these simulations are used to compare the computational times of the ALM and ASM. In the laminar case the ASM is 9 times faster than the ALM while using the same amount of cores; i.e. the computational time is reduced by up to 89%. The turbulent case is calculated with a difference in the allocated cores: the ALM uses 4 times more cores than the ASM; however, the ASM is still about 3.5 times faster than the ALM. Consequently, the ASM provides the same set of output parameters as the ALM but is significantly faster.

Through these simple simulations it can be seen that the sector methods offer savings in the computing time in comparison to the ALM. However, the ASM without SWIRL does not provide the expected results. Therefore, it is considered useful to compare the ASM with measurement data in the following.

4.2.2 Validation of the coupling with the eno114 3.5 MW turbine

As the generic NREL 5 MW does not allow for a comparison to measurement data, a free-field turbine is used for further analyses. Measurement data of an eno114 3.5 MW turbine, manufactured by eno energy [[eno energy, 2019](#)], with a hub height of 92 m and the corresponding FAST turbine model are used for further investigations.

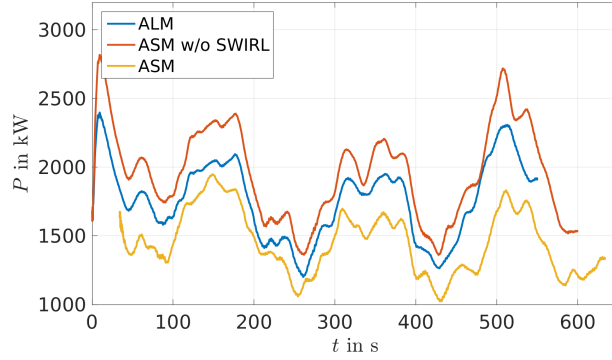


Figure 4.3: Comparison of different simulation methods for the generator power of the 5 MW NREL turbine in a turbulent flow at about 7.4 ms^{-1} wind speed at hub height.

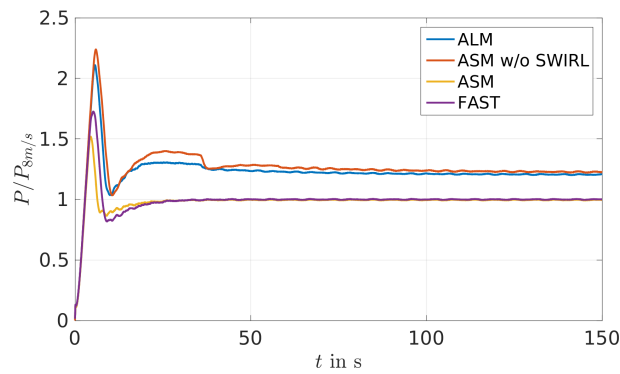


Figure 4.4: Comparison of different simulation methods for the generator power of the eno114 3.5 MW turbine in a laminar case with a wind speed of 8 ms^{-1} , normalised by the respective value of the eno114 3.5 MW energy power curve at 8 ms^{-1} .

First, we consider laminar cases with uniform wind speed over height for the eno114 3.5 MW in order to establish a power curve. The reference power curve is obtained from stand-alone FAST runs, with a laminar inflow. The FAST turbine model is provided by eno energy, but the source code of the turbine controller was not available to us; only an executable file was provided. The calculated reference power curve coincides well with the published power curve of eno energy [eno energy, 2019], without figure. Of the published power curve no further information on the computation or data is available, and therefore no comparative plot is possible. For a wind speed of 8 ms^{-1} the different models are compared again (see Fig. 4.4). The ALM again shows a higher power output than the reference power curve; the ASM coincides with the reference value and therefore with the value published by eno energy. The ASM without SWIRL shows again a higher power output than the ALM, although the difference is not as significant as in the laminar case of the NREL 5 MW turbine (see Fig. 4.2).

4.2.2.1 Conditions at the onshore measurement site near Brusow

The onshore measurement site, from which data were available, is situated in northern Germany close to the village of Brusow. At the measurement site two eno114 3.5 MW turbines are present. For

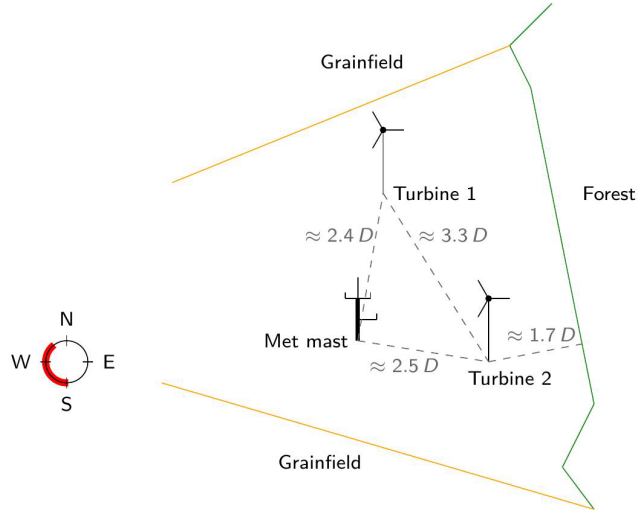


Figure 4.5: Schematic of the measurement site in Brusow. The remaining wind directions in the measurement data, after filtering, are indicated in red; D is the turbine diameter, here $D = 114.9$ m.

one turbine (turbine 1 in Fig. 4.5) measurement data were available, consisting among others of the power output, rotor speed, generator speed and tower, main shaft, and blade root bending moments.

Apart from the two energy turbines the measurement site was also equipped with a met mast. Figure 4.5 shows the general set-up of the site. The met mast contained three cup anemometers, one wind vane and one eddy-covariance station of the IRGASON type from Campbell Scientific. The cup anemometers were situated at the heights 34.6, 89.3 and 91.5 m; the wind vane was situated at 89.3 m; and one of the eddy-covariance stations was situated at 34.6 m. Another eddy-covariance station was located at a height of 2.3 m on the boom of a separate tripod that was situated next to the met mast.

From the 20 Hz data provided by the eddy-covariance stations, turbulence statistics with a resolution of 30 min are obtained by applying the eddy-covariance software TK3 [Mauder and Foken, 2015]. The planar fit method [Wilczak et al., 2001] is used for correcting impacts of a tilted device on the turbulence statistics. For calculating the planar coefficients, the whole available data set is taken into account. As the IRGASON is not an omnidirectional device, planar fit coefficients are calculated for four different wind direction sectors as suggested by the manufacturer of the IRGASON. The distance of the met mast to the turbine, for which measurement data are available, was 280 m ($\approx 2.5D$) in the 190° direction, referring to the wind turbine.

Data of all sensors is available from 10 May until 30 June in 2017. To the east of the site of the turbines and met mast a forest is located, which influences the measurements greatly. Therefore, the measurement data are filtered for the westerly wind directions, where mostly grainfields are situated.

We estimate the roughness length of the surrounding area using the wind speed u_{ec} and the friction velocity u_* , both provided by the lower eddy-covariance station, with Eq. (4.2) for data of neutral stratification, where k is the von Kármán constant, z_{ec} the height of the respective eddy-covariance station and z_0 the desired roughness length:

$$u_{ec} = \frac{u_*}{k} \ln \left(\frac{z_{ec}}{z_0} \right). \quad (4.2)$$

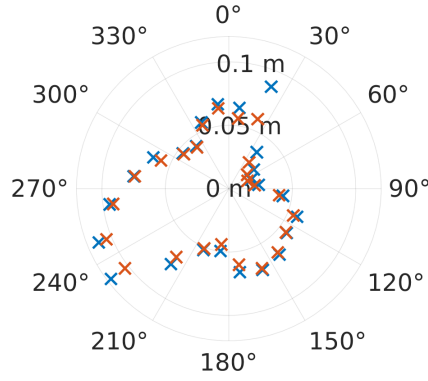


Figure 4.6: Roughness length distribution for varying wind directions for the measurement period. Two methods of averaging the roughness length values gained by Eq. (4.2) were used; here z_0 denotes the roughness length determined from 30 min eddy-covariance data, and j denotes the 15° wind direction bins: (1) averaging $z_{0,j}$ per 15° bins (blue) and (2) averaging using $\ln z_{0,j} = \frac{\langle u_* \ln(z_{0,j}) \rangle}{\langle u_* \rangle}$ per 15° bins (red), where the angle brackets $\langle \dots \rangle$ denote the average over values within the 15° bins.

The plot of the roughness length distribution (Fig. 4.6) shows an approximate roughness length of $z_0 = 0.1$ m for the westerly region. This value corresponds to farmland and hedges in the summer time according to Stull [2003], which is in agreement with the plants on-site, and therefore $z_0 = 0.1$ m is a reasonable value for the roughness length.

From the data of the eddy-covariance stations the stability parameter $\frac{z}{L}$, with z as the measurement height, here z_{ec} , and L the Obukhov length are obtained from the application of the software TK3 to them. In the following, the power that was produced during the respective times is plotted with respect to the wind speeds filtered by the stability, calculated from the data collected by the eddy-covariance stations. For that, the 50 Hz measurement data of the power are averaged over 10 min intervals, denoted as P_{10} . These 10 min power values are sorted according to stability and wind speed and averaged according to the wind speed within the respective stability, resulting in \bar{P}_{10} . For normalisation the maximum 10 min power value $P_{10 \max}$ is used. Accordingly, the standard deviation is calculated; i.e. the standard deviation is calculated for 10 min intervals $\sigma_{P_{10}}$, and then these 10 min values are averaged according to their stability and wind speed $\bar{\sigma}_{P_{10}}$ and normalised with the maximum 10 min standard deviation value $\sigma_{P_{10 \max}}$.

Figure 4.7 shows the resulting power data analysed with respect to the stability and normalised by simulation data of FAST, which coincides with the values provided by eno energy for the 3.5 MW turbine (cf. eno energy, 2019). Due to the relatively low number of measurements, the stabilities, based on the data of the lower eddy-covariance station of $z_{ec} = 2.3$ m, are sorted to stable ($\frac{z}{L} > 0.0115$), neutral ($-0.0115 < \frac{z}{L} < 0.0115$) and unstable ($\frac{z}{L} < -0.0115$) but not for further classification in very stable and very unstable (Table 4.2).

It can be seen that the measurement data deviate only slightly from the simulation data. Also, no clear trend between the different stratifications can be observed. Differences for the stratifications can be seen in the turbulence intensity and the shear (see Figs. 4.9 and 4.10). As expected the unstable cases have a higher turbulence intensity (TI) than the stable cases. This is also visible in the standard deviation of the power (see Fig. 4.8), as the higher TI in the neutral and unstable case leads to a higher standard deviation of the power than in the stable situations with lower TI.

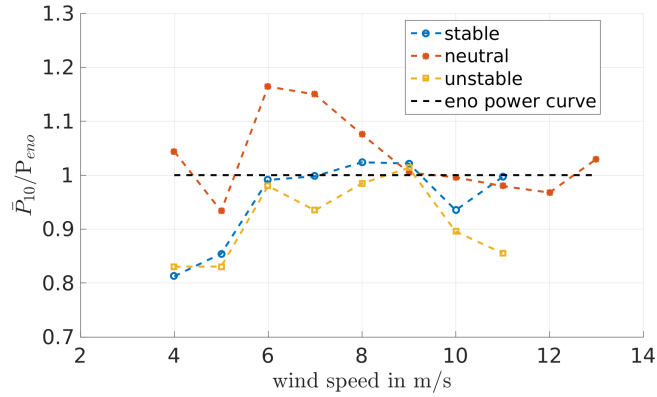


Figure 4.7: Power data determined from the measurement data for May/June 2017, normalised by the corresponding power of the eno114 3.5 MW power curve determined by FAST in laminar conditions, for different stabilities (determined from eddy-covariance data).

Table 4.2: Classification of atmospheric stability according to Obukhov length L , based on Peña et al. [2008]. The distribution of the atmospheric stability in the measured data can be seen in Figs. 4.9 and 4.10.

Obukhov length [m]	Atmospheric stability
$10 \leq L \leq 200$	Stable
$ L \geq 200$	Neutral
$-200 \leq L \leq -50$	Unstable

4.2.2.2 Simulation set-up for Brusow

In the following, the simulation set-ups for PALM and FAST that are used for the comparison to the measurement data are described.

PALM

In order to compare simulation results to the measurement data, simulations are computed that result in flow conditions similar to those observed under neutral boundary layer (NBL) and stable boundary layer (SBL) flow at Brusow. As can be seen in Figs. 4.9 and 4.10 most data are available for the NBL and slightly SBL.

Precursor simulations without a turbine are performed in order to reach a stationary state and evaluate the produced inflow conditions prior to the main simulations containing a wind turbine. The resolution for both neutral and stable conditions is set to 4 m in the x and y direction and in the vertical direction up to a height of 600 m. Above $z = 600$ m a vertical stretching of the grid with a factor of 1.08 is used. In accordance with the results of our evaluation of the roughness length from eddy-covariance data at the site, the roughness length z_0 is set to 0.1 m (see Fig. 4.6). A homogeneous roughness length is set in the model domain, and no topography is taken into account, which means that idealised simulation conditions are used. In Table 4.3 the different set-ups and in

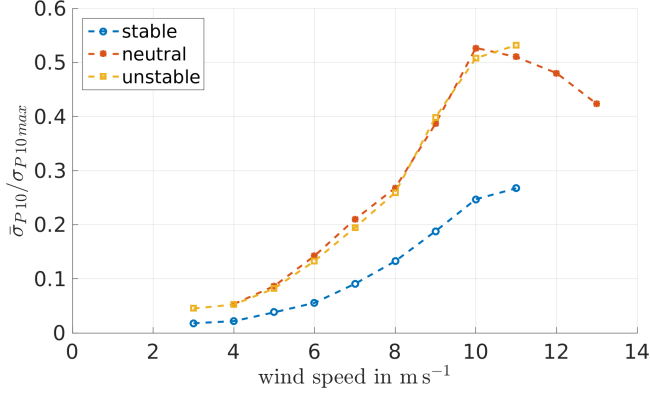


Figure 4.8: Standard deviation for 10 min intervals of the measured turbine power output, calculated according to $\sigma_{P_{10}} = \sqrt{\frac{1}{N_{\text{meas}}-1} \sum_{k=1}^{N_{\text{meas}}} |P(t_k) - P_{10}|^2}$, where $P(t_k)$ denotes the power data measured in 50 Hz, P_{10} the 10 min average and N_{meas} the number of measurements within the 10 min interval, normalised by the maximum 10 min standard deviation of the power, for May/June 2017, and sorted and averaged according to stability (determined from eddy-covariance data) and wind speed.

Table 4.3: Set-up of the precursor simulations: size of the model domain in the streamwise x , spanwise y and vertical z direction; grid size Δ ; cooling rate $\Delta\Theta/\Delta t$; geostrophic wind speed components at the surface in the x and y direction u_g and v_g ; and total simulated time t_{end} .

	x	y	z	Δ	$\Delta\Theta/\Delta t$	u_g	v_g	t_{end}
	[m]	[m]	[m]	[m]	[K h ⁻¹]	[m s ⁻¹]	[m s ⁻¹]	[s]
NBL	5184	2304	2928	4	0	10.0	-4.25	93600
SBL	1440	960	616	4	-0.25	9.5	-5.17	46800

Table 4.4 the resulting flow conditions are shown.

For the respective main runs including the turbine a larger model domain and non-cyclic boundary conditions were used to avoid influences of the wake onto the turbine. The model domain of the neutral case is larger than the one of the stable case, as in neutral conditions the turbulent structures tend to be larger than in stable conditions: the neutral model domain is set to 7680 m × 2595 m × 2928 m, and the stable is set to 5760 m × 2304 m × 616 m. The simulations are set up according to the simulations in Vollmer et al. [2016].

To reduce local effects caused by possible persistent structures in the flow, the main run is simulated three times with three different turbine positions in the y direction. Table 4.5 shows the differences of the flow between the turbine positions. The power output resulting from the simulations at the different positions is used to compare to the measured data, yielding three results for both stabilities as can be seen in Figs. 4.11 to 4.14.

Figures 4.9 and 4.10 show how the precursor simulations, i.e. the inflow conditions for the turbine, compare to the measurement data. The crosses represent the data from the precursor runs, so the undisturbed inflow averaged over space, at height 92 m, and time. In comparison to the measurement data, both simulations, neutral and stable, are in the lower region of the measured turbulence and

Table 4.4: Resulting flow parameters after reaching a stationary state in the precursor simulations, averaged over 3600 s: the magnitude of the wind speed at hub height averaged over the model domain $U_{92\text{m}}$, turbulence intensity calculated at one position in 92 m height $\text{TI}_{92\text{m}}$, shear parameter α (based on the power law $u_2 = u_1 \left(\frac{z_2}{z_1}\right)^\alpha$ for the relation of wind speeds at different heights), Obukhov length L in a height of 2.3 m and boundary layer height z_i .

	$U_{92\text{m}}$	$\text{TI}_{92\text{m}}$	α	L	z_i
	[m s ⁻¹]	[%]	[]	[m]	[m]
NBL	8.6	10.1	0.15	1228698	550
SBL	8.4	5.6	0.28	102	180

Table 4.5: Turbine positions along the y axis (keeping the same x position), with the y direction spanning from 0 to 2595 m for the NBL and from 0 to 2304 m for the SBL, in the model domain of the main run; additionally, the local wind speed $U_{92\text{m}}$ and turbulence intensity $\text{TI}_{92\text{m}}$ at hub height at these y coordinates, taken $2.5D$ in front of the turbine averaged over the last 10 min of a 650 s simulation.

	y	$U_{92\text{m}}$	$\text{TI}_{92\text{m}}$
	[m]	[m s ⁻¹]	[%]
NBL	500	8.21	10.3
	1000	8.92	10.5
	1700	8.87	8.0
SBL	1000	8.32	6.0
	1200	8.22	5.6
	1600	8.23	6.2

shear. However, the TI of the simulations is calculated using the resolved turbulence and disregarding the subgrid-scale one; hence, it is likely that the TI in the simulations is slightly higher than seen here. Therefore, the simulation set-up seems to resemble the inflow conditions at Brusow reasonably well. Since the flow conditions in the simulations match the measurements, the turbine output is compared in the following.

FAST

The turbine model of the eno114 3.5 MW turbine for FAST was provided by eno energy, including structural information and a pitch, a speed and a yaw control in the format of a Bladed .dll file, which was not accessible to us. However, the yaw of the turbine is neglected, as the flow in PALM was directed in such a way that the turbine is aligned with the wind. In FAST the modules ElastoDyn, AeroDyn and ServoDyn were used, and the degrees of freedom for the blade and tower were set to true except the rotor-teeter and yaw flag. All the platform degrees of freedom were neglected, i.e. set to false. The time step throughout all modules was set to $\Delta t = 0.01$ s. In AeroDyn the

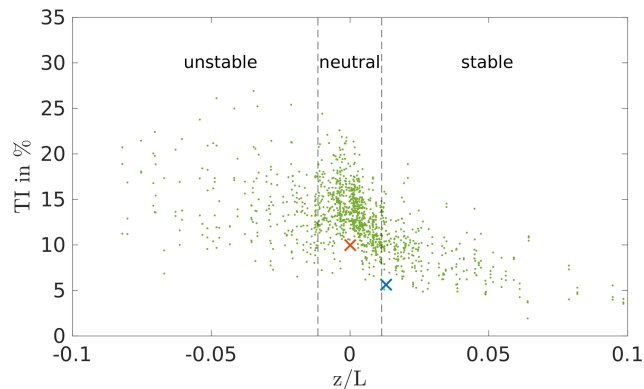


Figure 4.9: Turbulence intensity TI_{92m} of the measurement data (green) in comparison to the resulting TI_{92m} of the precursor runs sorted in neutral and stable (red – neutral; blue – stable).

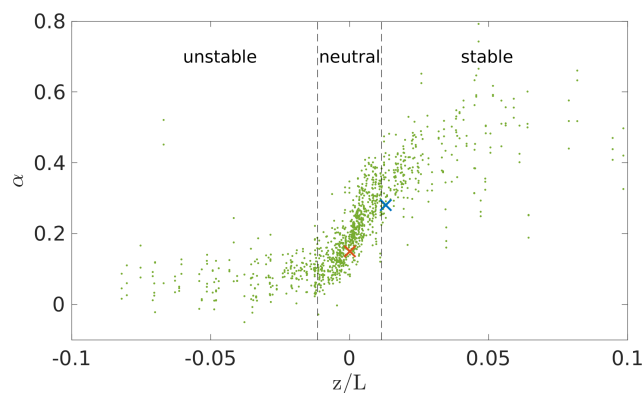


Figure 4.10: Shear of the measurement data (green) in comparison to the resulting shear of the precursor runs sorted in neutral and stable (red – neutral; blue – stable).

Beddoes–Leishman dynamic stall model, based on [Leishman and Beddoes \[1989\]](#) and the “Equil” option, a blade element momentum (BEM) theory model, for the inflow was selected. Additionally, the tip-loss and hub-loss models were enabled and set to the Prandtl tip-loss model [[Prandtl and Betz, 1927](#)].

4.2.2.3 Comparison of the turbine data

In the following plots the output data of the turbine in the simulations are compared to the measurement data. The main runs of the simulations are run for a simulation time of 650 s, and the results are averaged over 600 s, discarding the first 50 s as a spin-up of the turbine simulation; this time frame is derived from the laminar case (see Fig. 4.4). To compare the power output of the simulations to the measurement data, the power needs to be set into relation with the correct corresponding inflow wind speed. As the wind speed in Brusow is determined from a cup anemometer on a met mast at a distance of $2.5D$ from the turbine at hub height, in the simulation the wind speed is taken as well in a single point at a distance of $2.5D$ in front of the turbine position at hub height and averaged over time.

4.2. Validation

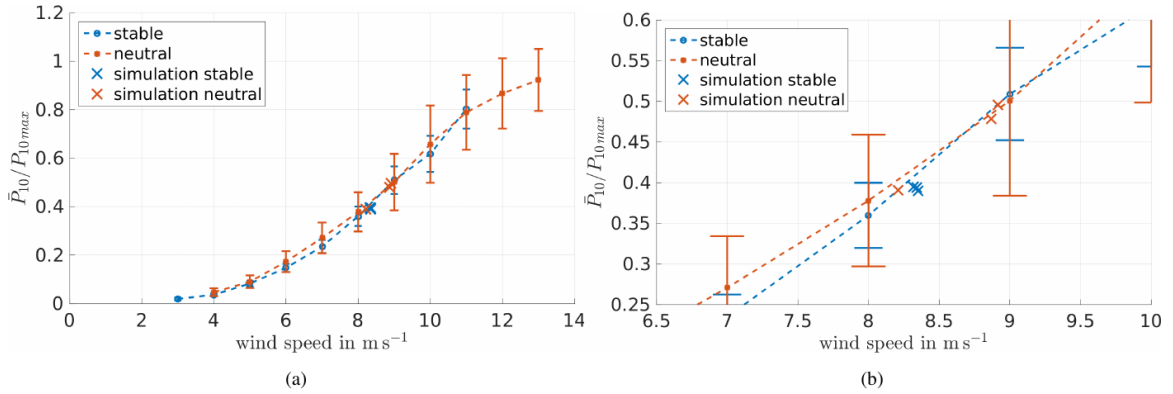


Figure 4.11: **(a)** Power curve, normalised by maximum 10 min power, determined from measurement data including standard deviation in comparison to the results of the simulation (marked by \times). **(b)** Enlargement of panel **(a)**. The standard deviation is plotted again in Fig. 4.12.

In Fig. 4.11 the simulation results are shown in comparison to the power curve determined by the measurement data at hub height. The error bars show the standard deviation of 10 min means. Figure 4.11 shows the same plot enlarged at the wind speeds of the simulation. According to [Dörenkämper et al. \[2014\]](#), using offshore data, and [Wharton and Lundquist \[2012\]](#), using onshore data, slight differences of the power output depending on the atmospheric stabilities can be seen. However, both publications together do not show a clear trend of which stability generally leads to the higher power output. In an offshore environment, as in [Dörenkämper et al. \[2014\]](#), unstable conditions lead to a higher power output below rated wind speed, and at an onshore site (see [Wharton and Lundquist, 2012](#)) the stably stratified atmospheric boundary layer (ABL) yields the higher power output. However, different wind speeds were used as a reference, which makes a comparison of the results difficult. In [Wharton and Lundquist \[2012\]](#) a rotor equivalent wind speed was used, while [Dörenkämper et al. \[2014\]](#) used the measurement data of a met mast at 90 m height.

The measurement data of Brusow, with the wind speed at hub height as reference, does not show any clear tendency for the dependency of the wind turbine power on atmospheric stability (see Figs. 4.7 and 4.11). A power curve depending on the rotor equivalent wind speed was calculated from the measured data as well but does not conclude in a clear trend either. The rotor equivalent wind speed was computed according to [Wagner et al. \[2014\]](#), but due to the limited number of measurement heights and their irregular distribution over the height, the results could be prone to errors. Therefore, for further analysis the hub height wind speed is used. The apparent independence of the wind turbine power on atmospheric stability might be due to the limited amount of only 2 months of data that were available or might be depending on the measuring and classification of the stability. As shown in [Wharton and Lundquist \[2012\]](#) the stability-filtered power curve greatly depends on the measurement heights used for determining the shear. However, this behaviour is also not present in the simulations. Therefore, in our case, the power output is not the proper parameter to show different turbine responses depending on the atmospheric stability.

Figure 4.12 shows the standard deviation of the power with respect to the wind speed. Higher fluctuations of the power in the neutral cases can be observed, corresponding to the higher TI that is present in the neutral stratification (cf. [Mittelmeier et al., 2017](#)). The simulation data show a

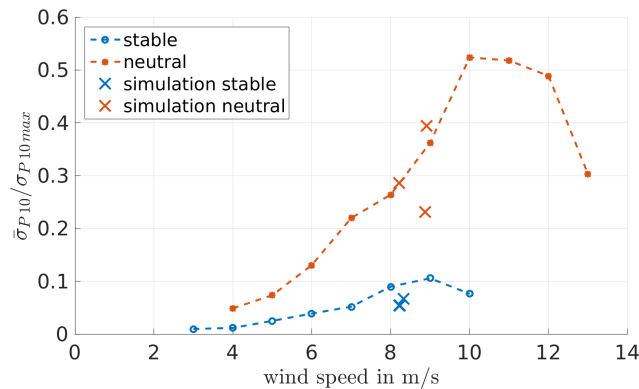


Figure 4.12: Normalised standard deviation of the power with respect to the wind speed determined from measurement data in comparison to the simulation results (\times). Sorted into stability by eddy-covariance data, TI and shear determined from the met mast data.

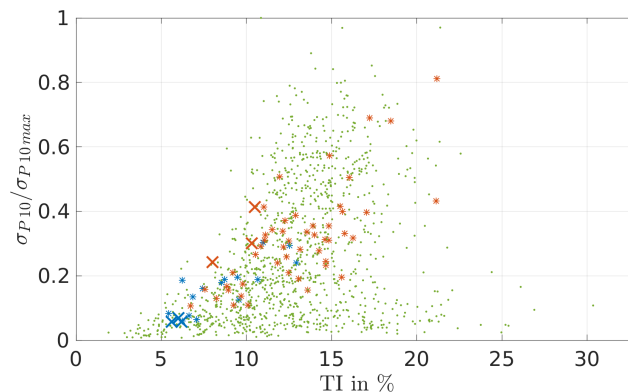


Figure 4.13: Standard deviation of the power with respect to the TI determined from measurement data (green – all wind speeds; blue and red asterisks – stable and neutral measurements at wind speeds of $8\text{--}9\text{ m s}^{-1}$) in comparison to the simulation results (\times).

comparable behaviour with lower fluctuating power in the stable cases than in the neutral ones. In the three neutral simulations the distribution of the standard deviation is spread relatively wide compared to the stable cases. The three different positions that were used for the neutral simulations differ slightly in wind speed and TI, which is not the case for the stable cases (see Table 4.5).

To check whether this distribution is comparable to the measurement data, a plot of the standard deviation of the power with respect to the TI is made (Fig. 4.13). It shows the relation between the power fluctuations to the TI for all measured values (green dots) and specifically the measured stable and neutral cases (blue and red asterisks) and in comparison the respective values of the simulations (blue and red crosses). As shown in Fig. 4.13, the results of the simulations show realistic data, even though they are not centrally located within the measurement points; therefore, other turbine parameters available are compared. Specifically, the blade and tower loads are investigated below.

The flap-wise and edgewise blade root bending moments are evaluated, but also data for the tower top and base loads are available and examined. Figure 4.14 shows the measured blade root bending moments with respect to the wind speed; the results of the simulations are indicated by

4.2. Validation

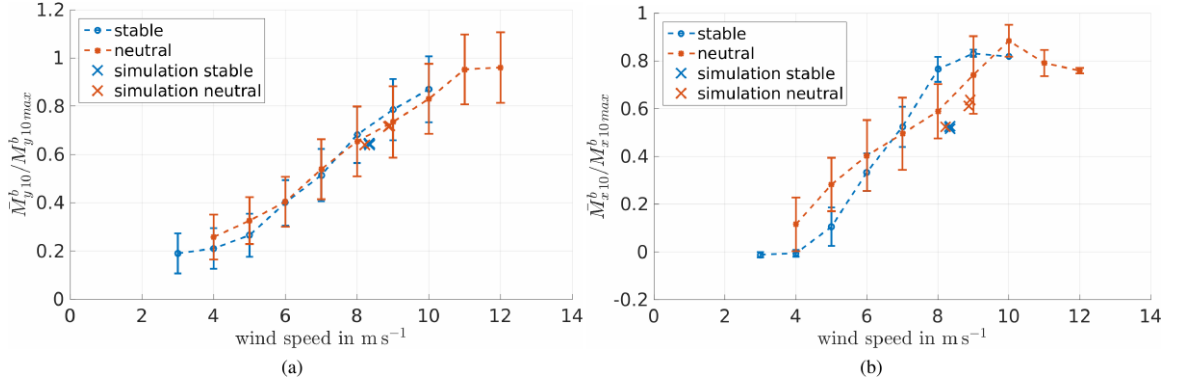


Figure 4.14: Blade root bending moment **(a)** out of plane M_y^b and **(b)** in plane M_x^b with respect to wind speed in comparison to the simulation results; averaged 10 min values were sorted by stability, averaged according to wind speed and normalised with the maximum measured moment.

crosses. The out-of-plane blade root bending shows a good agreement, and the in-plane blade root bending moment differs a bit more. However, a more suitable way to compare the loads is to look at the spectra.

We filtered the data with respect to westerly winds, stability and rotor speed. The analysis of the rotor speed showed a difference in the controller behaviour of the real system compared to the modelled one. This can be seen in Figs. 4.19 and 4.20, showing the measurements in Brusow. While Fig. 4.19 presents the relationship between the wind turbine power output and the rotor speed, Fig. 4.20 shows the relationship between rotor speed and wind speed. The combination of the respective values obtained from the simulations is provided by marks in these figures. Evidently, for the power output the values obtained for the simulation are within the standard deviation of the measurements that are indicated by bars. In that sense our set-up seems to be successful. We point out that we did not set up our simulations in such a way that they would lead to the reproduction of the mean behaviour of the wind turbine for the specific bins of measured data. We simulated just a few selected cases within the neutral and stable range of atmospheric stability. Thus, a deviation of the turbine response from the mean behaviour in the measurements can be expected. Note that the cases simulated by us are cases with a comparatively low turbulence intensity. We do not know the details of the controller of the wind turbine, so it is hard to verify any hypothesis for why our cases show a smaller rotor speed in comparison with the mean rotor speed for the next bin of measured data. Therefore, it is only possible to compare loads at either the same rotor speed or the same wind speed.

For the stable case some of the time intervals have to be discarded due to a varying quality of the load sensors, leaving one interval for the stable case where data are continuous for the blade and tower moments. For the neutral case the longest remaining interval covers a span 165 s long. The conditions of the chosen intervals are shown in Table 4.6. Ideally the chosen intervals should match the simulation parameters, but due to the described limitations in the measurement data, the remaining intervals can be seen as the best fit. These available cases suffice for the validation of our code. For an even more detailed load analysis, better fits might be necessary.

In the following the stable case will be discussed in detail. The neutral case also shows a good agreement between simulation and measurement data but covers only a short time interval of only

Table 4.6: Summary of the parameters of the measurement interval data used for the spectra of the blade and turbine loads: wind speed at hub height $U_{92\text{ m}}$, turbulence intensity at hub height $\text{TI}_{92\text{ m}}$, shear parameter α and the length of the available time interval t_{interval} .

	$U_{92\text{ m}}$ [m s ⁻¹]	$\text{TI}_{92\text{ m}}$ [%]	α []	t_{interval} [s]
Stable	7.7	9.0	0.27	600
Neutral	9.4	15.5	0.27	165

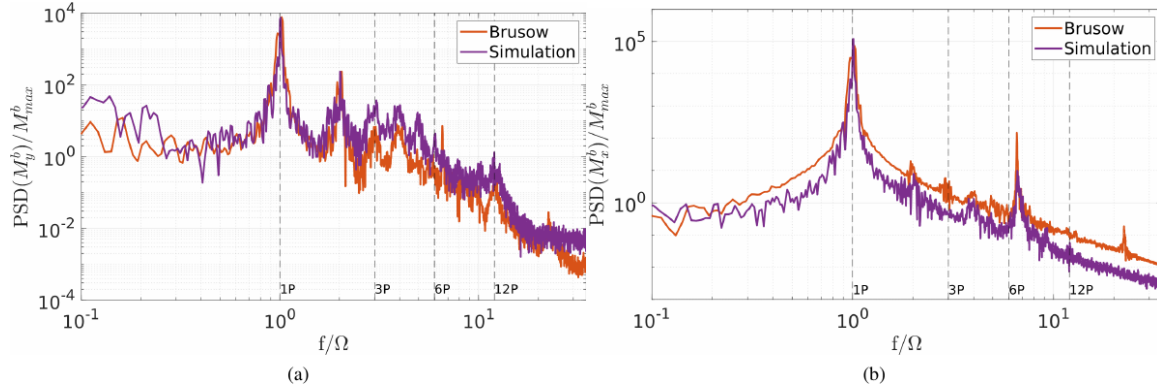


Figure 4.15: Spectrum of the blade root bending moment **(a)** out of plane M_y^b and **(b)** in plane M_x^b in comparison to the simulation results (stable). The data are normalised by the maximum value of the blade root bending moments.

165 s; the corresponding spectra can be found in Appendix A.2.

Figure 4.15 shows spectra of the blade root bending moments for the stable case. Figures 4.16 and 4.17 show the resulting tower load spectra for the stable case.

The spectra of the blade root bending moments are normalised by the same maximum value from both moments. The spectra of the tower top and tower base bending moments are normalised with their respective maximum values as well. The frequency is normalised by the rotor speed Ω .

In the spectra of the stable case it can be observed that the torsion loads show comparable results (see Fig. 4.17c). In addition, the fore–aft and side-to-side tower loads (see Fig. 4.16 and Fig. 4.17a, b) and the blade root bending moments (see Fig. 4.15) are represented well in the simulation. In general, most of the multiples of the rotor speed are represented in both the measurements and the simulations, and also their levels are comparable. The peaks show a difference in the width depending on the turbulence intensity; i.e. in the stable, less turbulent case the peaks are less wide than in the more turbulent, neutral case (figures in Appendix A.2). This can be observed both in the measurement data and the simulation results.

It can also be seen that the 1P peak is of different height in the tower load spectra. The peak of the simulation data reaches higher than the one of the measurement data. This is probably due to an overestimated blade imbalance in the simulation which has been used to respect weight and pitch differences between the blades (cf. Zhang et al., 2015). In the FAST turbine model one of the blades has a 1% higher mass density than the others, and also a pitch offset of 0.3° is set between all three

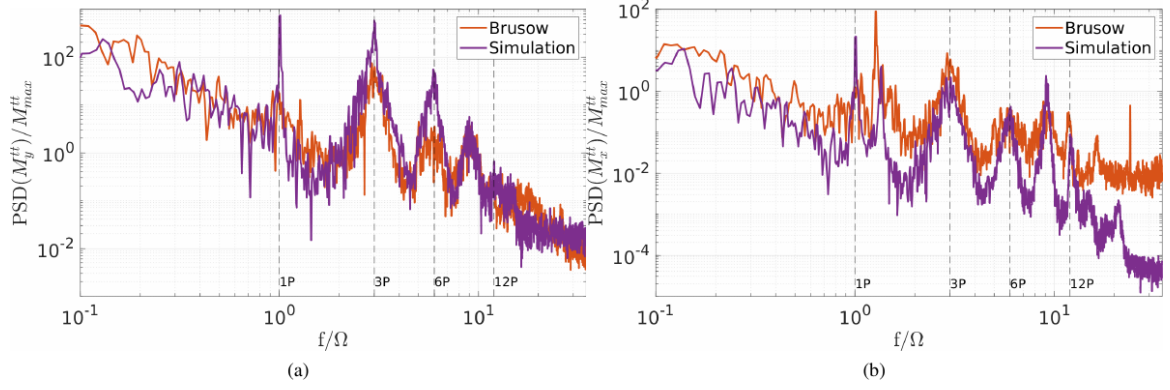


Figure 4.16: Spectrum of the tower top bending moment in **(a)** the fore-to-aft direction M_y^{tt} and **(b)** the side-to-side direction M_x^{tt} ; comparison of the measurement data to the simulation results (stable). The data are normalised by the maximum value of the tower top bending moments, and the frequency is normalised by the rotor speed.

blades. This results in a very pronounced 1P peak that does not exist in the measurement data.

Notable is also that there seems to be a discrepancy between the simulation and measurement data in the tower top side-to-side bending moment in stable and neutral conditions. This might be caused by the difference in the tower model to the real behaviour of the turbine tower. It can be seen that the first tower eigenfrequency is slightly lower on the real turbine and therefore more prone to the rotational excitation. In the measurement data the first tower eigenfrequency is closer to the 1P peak, and therefore the vibrations are less damped. Differences can also be observed in the 6P peak, especially in Fig. 4.16. The 6P peak is greatly influenced by the shear and the wind speed differences across the rotor area. A plot of the wind speed profiles can be found in Appendix A.3; even though the shear is similar, the difference in the wind speeds, which are caused by the above-described limitations in the measurement data, led to diverging wind speed profiles. In Fig. 4.18 a comparison between the neutral and stable simulation results for a blade root bending and tower bending moment is shown. The bending moments that are mostly affected directly by the flow, i.e. by the thrust, are chosen. It can be observed that the neutral simulation leads to wider peaks due to the higher TI and the resulting varying rotor speed. Also, a difference in the height and depth of some peaks can be seen. Namely for the blade root bending out-of-plane moment the 2P and for the tower fore-aft bending moments the 3P and 6P peaks are higher and reach further down for the stable case than the neutral case. These multiples of the rotor speed are influenced by the shear of the flow which also indicates a difference in the inflow of the turbines.

To investigate the loads further, rain flow counts and the value of the equivalent load range Δ_{eq} (non-normalised damaged equivalent loads (DEL)) were calculated. Equation (4.3) shows the used Palmgren–Miner rule, taken from [Vera-Tudela and Kühn \[2017\]](#):

$$\Delta_{\text{eq}} = \left(\sum_{k=1}^n N_k \Delta S_k^m / N_{\text{ref}} \right)^{1/m}, \quad (4.3)$$

where n is the number of different loading amplitudes, N the number of cycles and ΔS the loading amplitude. Further, a Wöhler exponent of $m = 10$ for the blades, $m = 4$ for the tower and a

4. Validation of a coupled atmospheric–aeroelastic model system for wind turbine power and load calculations

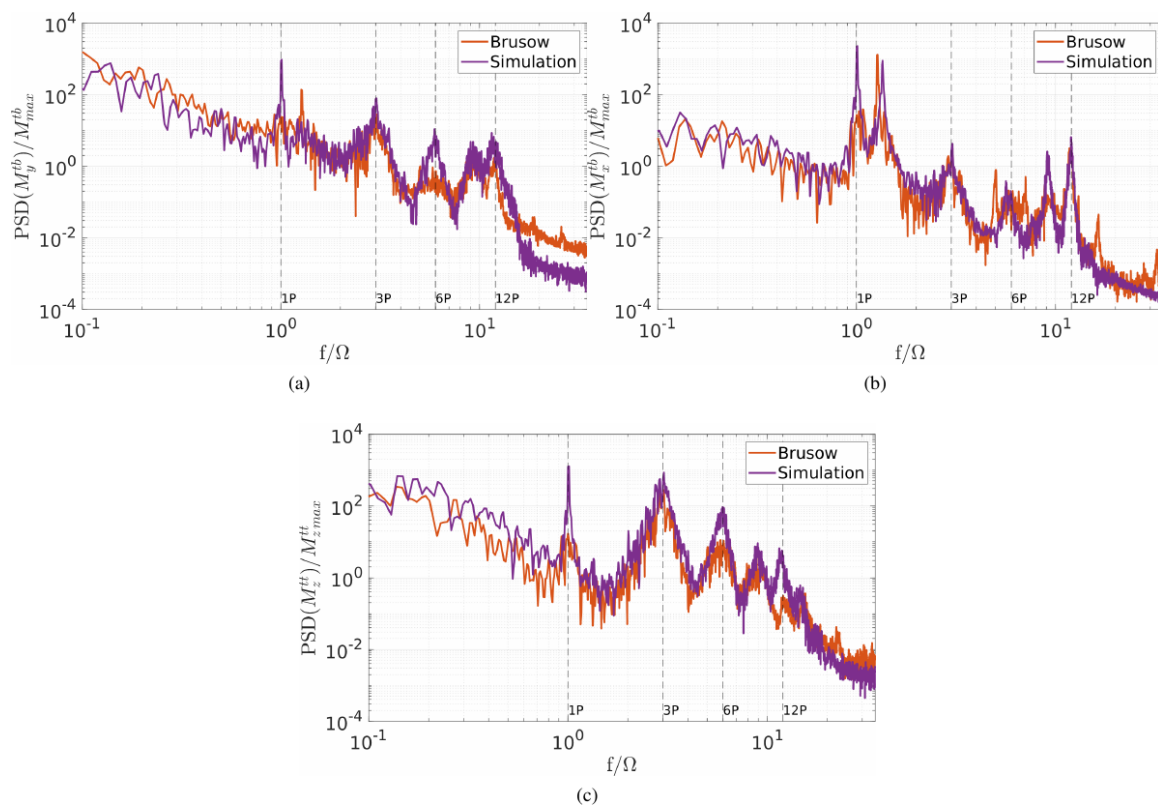


Figure 4.17: Spectrum of the tower moments: **(a)** the tower base bending in the fore-to-aft direction M_y^{tb} , **(b)** the tower base bending in the side-to-side direction M_x^{tb} and **(c)** the tower top torsion M_z^{tt} ; comparison of the measurement data to the simulation results (stable). The data are normalised by the maximum value of the tower base and tower top torsion moment, and the frequency is normalised by the rotor speed.

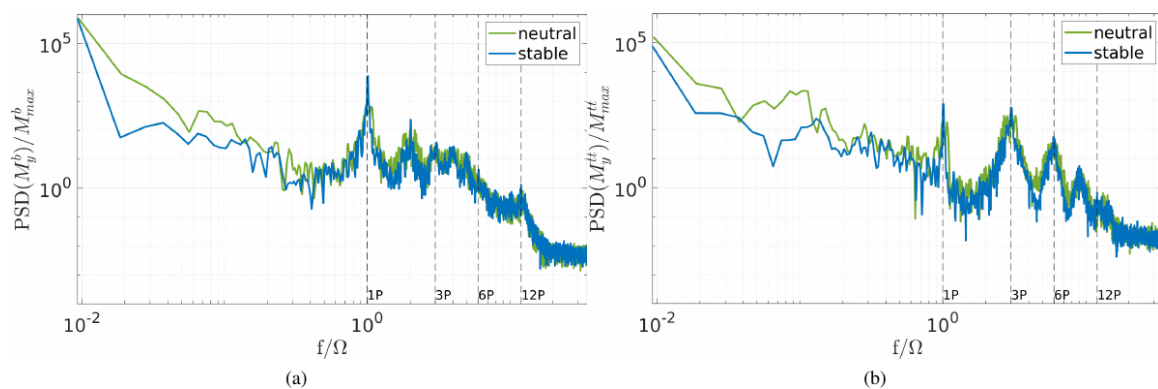


Figure 4.18: Comparison of the **(a)** blade root bending moments out of plane M_y^b and **(b)** tower top fore–aft bending moment M_y^{tt} for the stable and neutral simulation. The data are normalised by the maximum value of the blade root bending and tower top bending moments, and the frequency is normalised by the rotor speed.

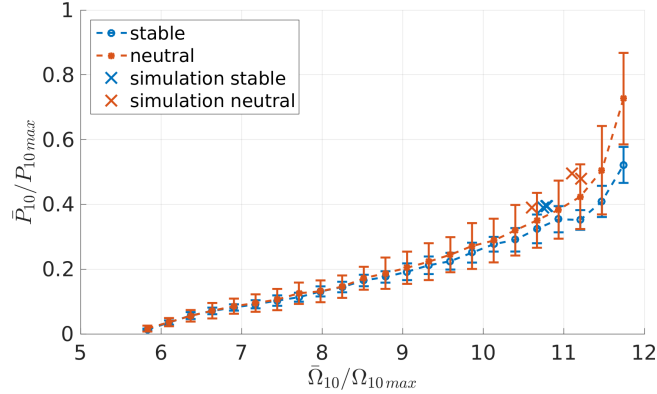


Figure 4.19: Power output normalised by the maximum measured power, plotted with respect to the rotor speed, and normalised with the maximum measured rotor speed with an added offset for the measurement data in comparison to the simulation data.

reference number of cycles $N_{\text{ref}} = 10^7$ is assumed.

A comparison between the measurement data and the simulation results is not useful in this case as the available intervals vary in their inflow parameters and therefore the rotor speed. However, a comparison between the results of the simulation of the neutral and stable boundary layer flow shows the influence of the stability on the load outputs of the LES coupling. Table 4.7 shows the comparison of the equivalent load range for the stable and neutral simulations, calculated for a 10 min interval. It can be observed that almost all the neutral values are higher than the ones from the simulation of the stable case. The only exception is the blade root bending in-plane load, which shows approximately the same value for both cases. As this load is not that dependent on the flow but rather influenced by gravity and rotor speed, the result still seems conclusive.

The values can be linked to the power spectra shown in Fig. 4.18. Particularly in the range of the lower frequencies larger power spectral density (PSD) values are obtained for the neutral case in comparison with the stable case. To investigate the influence of the lower frequencies on the equivalent load range, the equivalent load range for the tower top fore-aft bending moment is calculated with a high-pass filter as an example. The following values result for the equivalent load range when the frequencies below 0.1 are disregarded (stable: $\Delta_{\text{eq}} = 81.8 \times 10^5$ kNm; neutral: $\Delta_{\text{eq}} = 98.7 \times 10^5$ kNm), which clearly shows that the lower frequency range has a great influence on the equivalent load range. A higher value for the neutral case is expected as the flow contains larger eddies than the stable case.

This should be considered as a qualitative result. For a final quantitative analysis simulations with considerably larger run times or a number of simulations with different seeding would be required. Also, in the papers Lee et al. [2012] and Holtslag et al. [2016] no clear results are visible; in Lee et al. [2012] it is stated that mainly the roughness has an influence on the loads, while the stability has only a small effect. In Holtslag et al. [2016], on the other hand, a clear influence of stability on the loads is observed.

As can be found in Fig. 4.19 the measurement data show a dependency on the atmospheric stability. Neutral conditions lead to higher power output for the same rotor speed than stable conditions. This behaviour might be explained due to the higher fluctuations caused by higher TI

Table 4.7: Comparison of the equivalent load range Δ_{eq} of the simulation results (10 min interval), according to Eq. (4.3) with $m = 10$ for blade loads and $m = 4$ for tower loads.

Load	Δ_{eq} [kNm]	
	stable	neutral
Blade root bending in plane	1579	1578
Blade root bending out of plane	687	717
	$\Delta_{eq}/10^5$ [kNm]	
Tower top fore–aft bending	70.6	132.7
Tower top side-to-side bending	1.1	8.9
Tower top torsion	82.0	154.3
Tower base fore–aft bending	910.0	7623.8
Tower base side-to-side bending	373.6	963.7

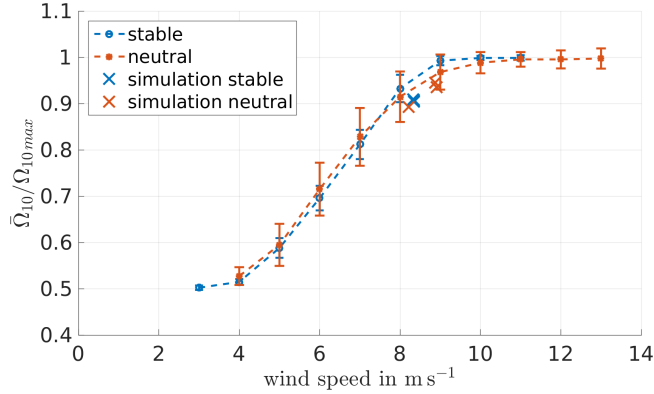


Figure 4.20: Relation between the rotor speed Ω , normalised with the maximum measured rotor speed with an added offset, with respect to the wind speed determined using the measurement data in comparison to the simulation data (\times).

and the therefore higher energy content in the wind. However, the simulations did not reproduce the same dependency, which might be explained by the limited variability of the TI in comparison to the measurement data. As can be seen in Fig. 4.13 the simulations cover the lower limit of the TI in the respective wind speed.

4.3 Conclusion

This study demonstrates the feasibility of coupling the LES tool PALM with the aeroelastic model FAST to simulate wind turbine behavior under various atmospheric conditions for a single turbine. The coupling provides a powerful framework by combining the high-resolution simulation of atmospheric flows using PALM with the detailed turbine response calculations performed by FAST.

The approach was validated in two steps. First, a comparison was made with the generic NREL

5 MW turbine to evaluate the coupling’s computational efficiency and power output accuracy. The results showed excellent agreement in terms of power output, with computational time savings of up to 89% compared to a comparable ALM-based coupling.

Second, the enhanced coupling was validated against measurement data from the eno114 3.5 MW turbine. The simulated power output closely matched the measured data, largely due to the use of wind speed sampling in front of the turbine rather than at the rotor area, which avoids overestimating power. Additionally, the standard deviation of power output, which reflects turbulence effects and stability, aligned well with the measurements. Despite the idealized simulations—homogeneous roughness length and absence of topography—the results showed good agreement with reality.

Blade and tower load predictions were generally representative of the measurements. Some deviations were attributed to differences in aeroelastic modeling parameters, such as tower eigenfrequency, rotor imbalance, controller settings, and wind speed inputs. However, the overall load spectra and variations due to atmospheric stability were well captured, demonstrating that the PALM–FAST coupling is suitable for investigating the influence of different atmospheric conditions on turbine behavior.

Although the frozen wind field assumption (e.g., Taylor’s frozen turbulence hypothesis) did not affect the outcomes in this study, it may introduce limitations in scenarios involving temporally varying wind fields or changing wind directions. Similarly, a turbine operating in a wake remains an area requiring further exploration, as wake recovery under the frozen wind field assumption was not addressed. Future work should include comparisons with measurement data in more complex scenarios, such as unstable atmospheric stratification or turbine wake interactions, to further validate the method.

Despite these limitations, the reduced computational time of the PALM–FAST coupling makes it highly suitable for performing load analyses of single turbines in wind farms. This is a notable improvement over traditional approaches using ADM or ADMR, as ALM is often too computationally expensive for large model domains.

Additionally, the time-efficient nature of the coupling opens up a range of applications. Beyond load analyses for wind farms, it can be used to study the relationship between environmental conditions and turbine performance in footprint analyses or to investigate atmospheric phenomena such as low-level jets and their impact on turbine loads. Furthermore, the coupling provides a valuable tool for examining turbine behavior in more complex scenarios, such as a turbine operating in the wake of another, enabling insights into wake effects and their influence on turbine performance and loads.

Appendix

A.1 Blade elements in the NREL 5 MW turbine laminar case

The following plots show the dynamic pressure, the angle of attack, and the lift and drag coefficients for the NREL 5 MW turbine in the laminar case.

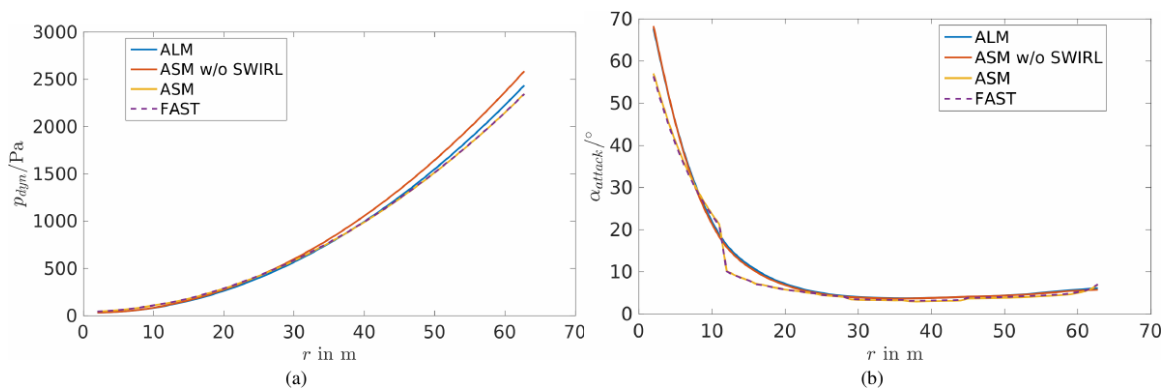


Figure 21: Dynamic pressure (a) and angle of attack (b) along the blade nodes in the laminar case of the NREL 5 MW turbine.

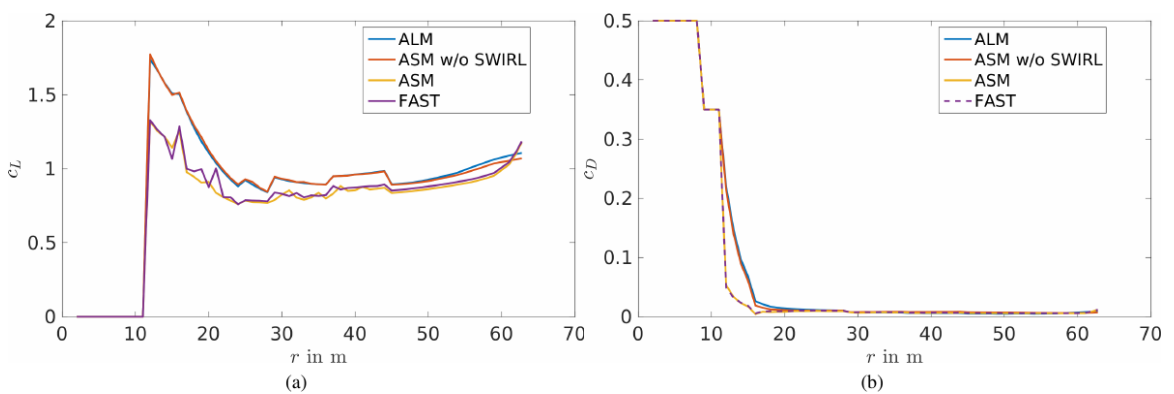


Figure 22: Lift (a) and drag (b) coefficient along the blade nodes in the laminar case of the NREL 5 MW turbine.

A.2 Spectra of the loads for the neutral case

The following plots show the blade and tower load spectra for the neutral case.

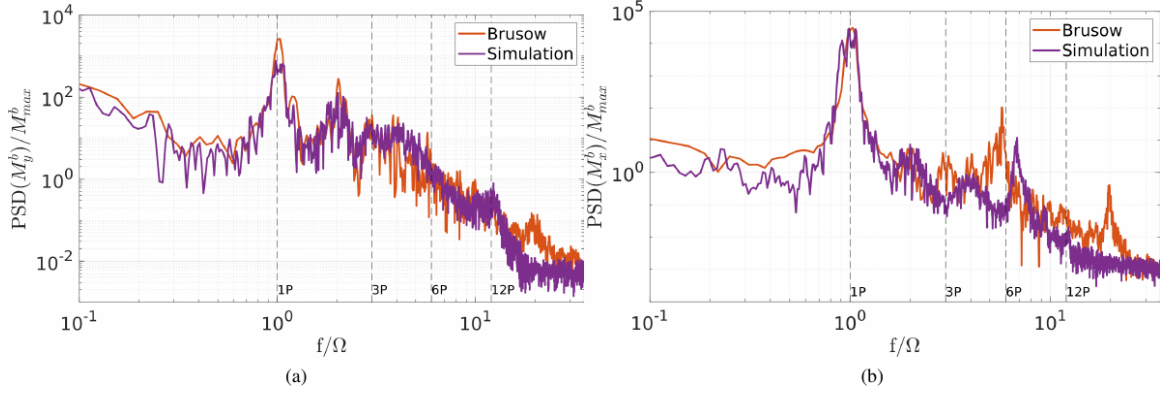


Figure 23: Spectrum of the blade root bending moment (a) out of plane M_y^b and (b) in plane M_x^b in comparison to the simulation results (neutral). The data are normalised by the maximum value of the blade root bending moments, and the frequency is normalised by the rotor speed.

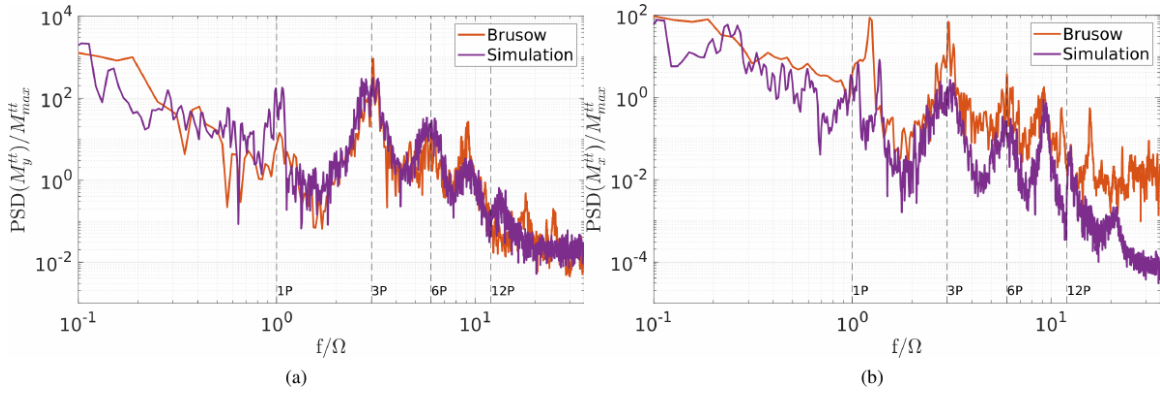


Figure 24: Spectrum of the tower top bending moment in (a) the fore-to-aft direction M_y^{tt} and (b) the side-to-side direction M_x^{tt} ; comparison of the measurement data to the simulation results (neutral). The data are normalised by the maximum value of the tower base bending moments, and the frequency is normalised by the rotor speed.

A.3. Wind profile comparison for the stable case

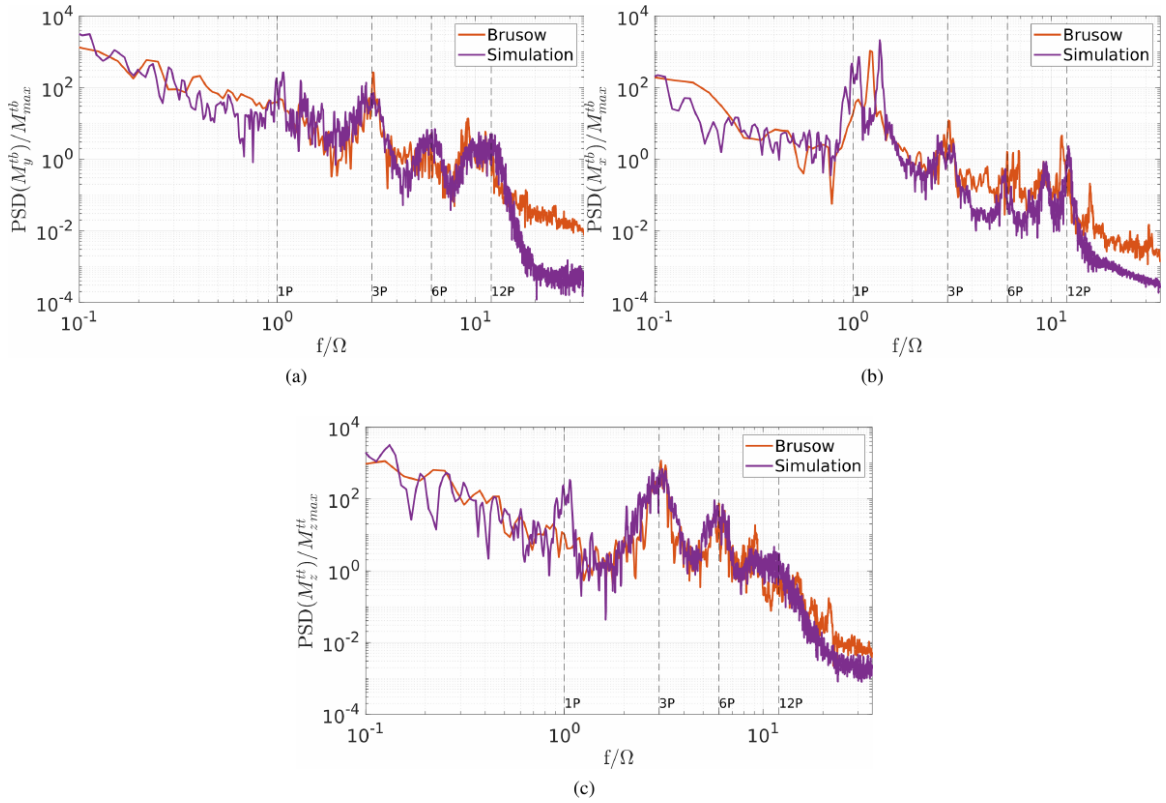


Figure 25: Spectrum of the tower moments: **(a)** the tower base bending moment in the fore-to-aft direction M_y^{tb} , **(b)** the tower base bending moment in the side-to-side direction M_x^{tb} and **(c)** the tower top torsion moment M_z^{tt} ; comparison of the measurement data to the simulation results (neutral). The data are normalised by the maximum value of the tower top torsion moment, and the frequency is normalised by the rotor speed.

A.3 Wind profile comparison for the stable case

Here, the comparison of the wind profiles for the stable case is shown.

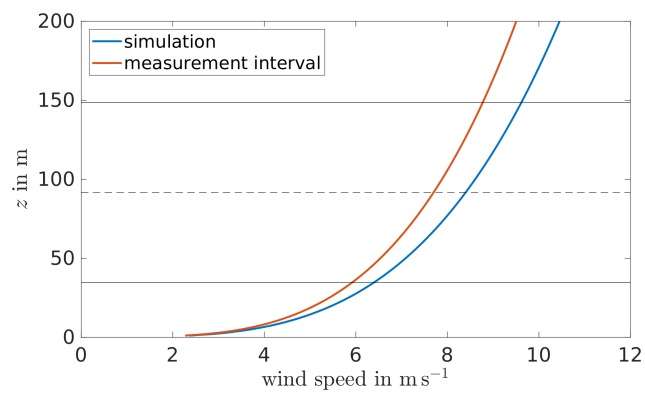


Figure 26: Wind profiles, calculated by the shear and wind speed, of the measurement interval and the simulation data used in the comparison of the loads for the stable case. The black lines indicate the rotor area, and the dashed line indicates the hub height.

Chapter 5

Improved coupling between an atmospheric LES and an aeroelastic code for the simulation of wind turbines in turbulent flows

The content of this chapter was submitted at Wind Energy Science: Steinbrück, S., Eilers, T., Vollmer, L., Avila, K., and Steinfeld, G.: Improved coupling between an atmospheric LES and an aeroelastic code for the simulation of wind turbines under heterogeneous inflow, *Wind Energ. Sci. Discuss.* [preprint], <https://doi.org/10.5194/wes-2024-146>, 2024. Following the referees' suggestions, we withdrew the manuscript and will submit it to a technical journal that better suits the depth of the methodological descriptions.

Contributions: I guided the implementation of the NWC into an ALM within the PALM-FAST coupling as a second reviewer for a Master's thesis. Subsequently, I developed a new variant of the ASM to facilitate the integration of the NWC into the ASM coupling framework. I tested the framework and performed simulations to compare the generated data with measurements, as well as conducted model-to-model comparisons. I analyzed the results, and created figures to effectively present the findings. I wrote the first draft and integrated corrections based on both linguistic and content-related feedback.

In Chapter 4, a model framework is introduced that couples the aeroelastic code FAST with the LES tool PALM. This framework employs a sector-shaped representation on the LES side while retaining the blade element approach within FAST. The combination facilitates efficient calculations with high resolution and accurate turbine output. A key advantage of this coupling is its significantly higher computational speed compared to an ALM in a similar setup. For example, an 89% reduction in computational time for a sample case was seen in the results shown in Chapter 4. To avoid inaccuracies in turbine force calculations when using rotor-area wind speeds, the proposed framework relies on undisturbed inflow wind speeds outside the rotor's induction zone, unaffected by turbine influence. To account for the influence of the rotor on the undisturbed wind speed and calculate the actual wind speed at the rotor area, the SWIRL induction model in FAST is used. This model calculates wind speeds along the rotor line, assuming the applicability of Taylor's frozen eddy hypothesis [Taylor, 1938, Moriarty and Hansen, 2005]. The coupling described in Chapter 4, referred to as ASM SWIRL from now on, was validated using simulation data from the generic

NREL 5 MW turbine [Jonkman et al., 2009b] and measurements from an eno1143.5 MW turbine. The results showed strong agreement between the modeled and measured load spectra and power output. Furthermore, the method was benchmarked against other models of varying fidelity in a free inflow scenario [Doubrawa et al., 2020], confirming its reliability.

However, the SWIRL induction model’s assumptions break down when the upstream flow is temporally or spatially heterogeneous, such as in the wake of another turbine. Moreover, ASM SWIRL introduces a time offset by using wind speeds upstream of the rotor to compute turbine properties, such as power, at the rotor plane. For cases with varying inflow conditions, avoiding this time offset requires using wind speeds within the rotor area, which necessitates corrections to mitigate potential errors. Interpolation of wind speeds to blade positions can also lead to inaccuracies, depending on the grid resolution. As outlined in Chapter 1.2, the correction by Meyer Forsting et al. [2020] shows promise in enhancing turbine output and should therefore be integrated into the PALM-FAST coupling. Originally developed for an ALM with stiff blades, this correction must be adapted for use with an ASM. Mohammadi et al. [2024a] demonstrated that this adaptation yields favorable results in a laminar flow case. On the other hand, transitioning from ALM to ASM and applying NWC introduces uncertainties regarding result fidelity. The spatial simplifications inherent in ASM can lead to deviations from reality, particularly in turbulent flows. While steady turbulent flows are relatively straightforward, the complexity increases in scenarios such as turbine wake regions, where turbulence evolves with distance from the upstream turbine. Under such challenging conditions, models like ASM SWIRL may encounter limitations, and the behavior of ASM with NWC in these scenarios remains untested. The following sections will focus on addressing these uncertainties and assessing the applicability of ASM with NWC in turbulent flow scenarios.

5.1 Methodology: Extension of the PALM-FAST coupling to include NWC

In simulations using an ALM, the Gaussian force smearing incorporates the Lamb-Oseen viscous core, which is present in both bound and trailed vorticity. The presence of the viscous core in the vortex leads to lower induced velocities near the vortex center when compared to the inviscid solution of the lifting line theory, which serves as the theoretical foundation for the ALM. As a result, the trailed vorticity induced by an ALM results in larger angle of attacks and increased forces at the blades. To address and recover this missing induction, the NWC method combines a near-wake model of the trailed vorticity with the Lamb-Oseen viscous core model. This is achieved by utilizing the correlation between the smearing length scale ε and the radius of the viscous core. For each trailed vortex between blade elements, its distance to all elements on the blade is determined in each time step, and the correction value is calculated based on its circulation strength and viscous core size. The induced velocities of such vortices change at each time step due to blade rotation, flow convection, and dissipation caused by the viscous core. The correction process is iterative and affects the circulation at the blade elements and the evolution of trailed vortices.

The NWC is implemented in three versions of the PALM-FAST coupling: an ALM and two ASM variations, as listed in table 5.1. As the NWC was developed for an ALM, the first implementation in the PALM-FAST coupling is carried out for the model of an identical time step in FAST and PALM, i.e. an ALM.

Table 5.1: Overview of the different models and their key differences.

	ALM (NWC)	ASM SWIRL	ASM-CL (NWC)	ASM-SL (NWC)
wind speed	wind speed in rotor area	wind speed in front of turbine + SWIRL	wind speed in rotor area	wind speed in rotor area
blade shape	lines	sector	sector	sector
method	FAST: blade element approach	per line in sector, transfer of wind speeds to FAST cf. Fig. 5.2a, correction by SWIRL FAST: BEM	per line in sector, transfer of wind speeds to FAST cf. Fig. 5.2a FAST: blade element approach	only wind speeds of first line is used cf. Fig. 5.2b FAST: blade element approach

The original code for the NWC corrects the wind speeds and calculates the corrected forces at the blades. It was developed for stiff blades without deflection. In our case, the calculation of the forces is done by FAST and should remain there, since the extensive output of FAST, including deflections, is desired. Therefore, the NWC is implemented in such a way, that the wind speeds are being corrected and the corrected wind speeds are passed on to FAST. This means that the part of the NWC that corrects the wind speeds is called for each FAST time step on the PALM side. The calculation of the forces within the code of [Meyer Forsting et al. \[2020\]](#) is not used here. The corrected wind speeds are then sent from PALM to FAST as the current wind speed at the respective blade node positions.

Furthermore, the NWC is implemented in a sector method based on ASM SWIRL. A schematic of the working principle can be seen in Fig. 5.1. The ASM, instead of the ALM, on the PALM side is implemented to decouple the time stepping of FAST from PALM in order to make it computationally less expensive. While FAST is calculating usually with a time step smaller than an ALM model, i.e. ensuring that the chosen sampling rate covers the key frequencies of the system, the PALM time step is larger and set internally by PALM, determined either by the Courant–Friedrichs–Levy (CFL) criterion or the diffusion criterion, enabling the most efficient running of the LES code. The sector size is determined by the PALM time step, which is calculated first, and the rotor speed transmitted by FAST. The number of lines per sector (see Fig. 5.2) corresponds to the blade positions that FAST executes until it has caught up with the previous PALM time step ($t_{\text{FAST}} \leq t_{\text{PALM}}$), where t denotes the respective simulation time. The number of lines per sector can be expressed as: $n = \lfloor \frac{\Delta t_P}{\Delta t_F} \rfloor$, which reflects the relationship between the respective time steps, rounded down.

PALM provides the wind speed information that FAST needs by using a frozen wind field. This approach entails that PALM temporarily halts its calculations until the FAST time aligns with the PALM simulation time. During this pause, the wind speeds from the most recently computed PALM time step are transmitted to FAST. These wind speeds correspond to the current blade positions calculated by FAST. Using this data, FAST computes the forces acting on the blades. The forces are then projected onto the positions where the wind speeds were sampled, as illustrated in Fig. 5.2.

5. Improved coupling between an atmospheric LES and an aeroelastic code for the simulation of wind turbines in turbulent flows

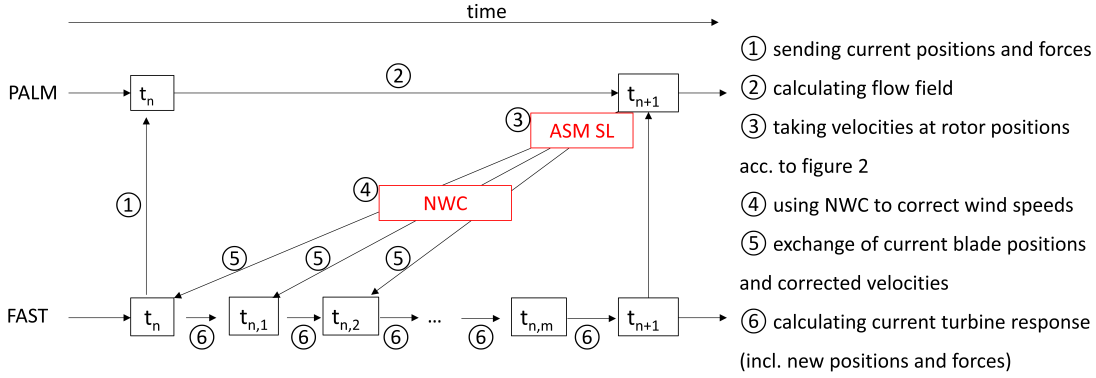


Figure 5.1: Schematic of the operation mode of the proposed coupling ASM-SL, the red fields show the points of change in comparison to ASM SWIRL, see also table 5.1 for explanation of the methods.

These forces are smoothed with a polynomial that generates a Gaussian distribution, enabling them to be distributed across the area surrounding the rotor blade in all three spatial directions [Sørensen and Shen, 2002]:

$$\eta = \frac{1}{\varepsilon^3 \pi^{3/2}} \cdot \exp \left[- \left(\frac{r}{\varepsilon} \right)^2 \right] \quad (5.1)$$

Here, η represents the regularization function applied at the grid nodes within a specific vicinity of the turbine. The variable r denotes the distance between the respective node and the blade element from which the force originates. The parameter ε is a factor related to the grid size, typically, and in this context as well, set to $\varepsilon = 2\Delta$ [Trolborg, 2008], where Δ is the grid size.

Consequently, the new wind speeds are taken adjacent to the applied forces, at the edge of the Gaussian force distribution. As a result, the first line of the new time step is most significantly affected by the previously imposed forces, with this influence diminishing as the distance from the previous sector increases. In general, there are two options for velocity sampling in ALM setups. The second option is to take the velocities at the positions of the maximum force smearing, see e.g. Martínez-Tossas et al. [2017]. In our work, based on our existing ALM code, the velocities are taken at the new blade position, i.e. at the tails of the force smearing. Applied to the ASM, this means that the wind speeds at the first position of the new sector are most similar to the principle of the ALM. In Mohammadi et al. [2024a] both approaches have been tested, revealing that, depending on the wind speed sampling method used, different velocity sampling positions within the sector are necessary to achieve results comparable to the ALM. Our approach aims to select a position that aligns technically with the ALM principle, providing robustness and minimizing dependence on changes in sector size. Given that PALM employs a variable time step, resulting in a variable sector size, it is crucial for the velocity sampling methodology to be as independent of this variability as possible.

In ASM SWIRL the wind speed information is instead obtained from the free inflow in front of the turbine at the corresponding blade element positions in combination with using the FAST induction model SWIRL. Due to using wind speeds of the free inflow, the results obtained from this method include at least a temporal offset. This is because the wind speeds used for calculations

reach the actual turbine at a later time.

Certain adjustments were necessary to successfully implement the NWC, the resulting variations are denoted as ASM-CL and ASM-SL. In the method proposed here, the wind speeds are taken in the rotor area and the induction model SWIRL is switched off. But the principle of the sector remains i.e. the wind field in PALM, which computes with a larger time step, is frozen, while FAST receives the wind speeds at the required positions from the frozen wind field until the simulation time of FAST reaches the ahead-running PALM time.

The distinction between ASM-CL and ASM-SL lies in the positions of where the wind speeds are extracted. The principle of ASM-CL is shown in Fig. 5.2a, where the new positions of the blades move away from the previously smeared forces in PALM until the current time in PALM is reached and a new wind field is computed. The previous sector, which is the area that the blade covers over one PALM time step, is indicated as light red. In this area and the surrounding grid points the forces have been smeared using a Gaussian shape for each line in the sector. The influence of the introduced forces are highest close to this sector, meaning the blade position where the wind speed U_n is denoted. At increasing distances from the previous smearing, the influence of the forces reduces, as the thrust force of the turbine decreases with distance to the smearing, and therefore, wind speeds are not reduced. Consequently, this results in too high wind speeds and also an overestimation of the turbine power. Thus, as the distance to the smearing from the previous time step increases, the influence of the previous forces on the wind speeds diminishes, leading to even higher wind speeds compared to the ALM without NWC. Further corrections would be necessary to counteract the increased wind speeds due to the lack of influence of the forces, which is not pursued here.

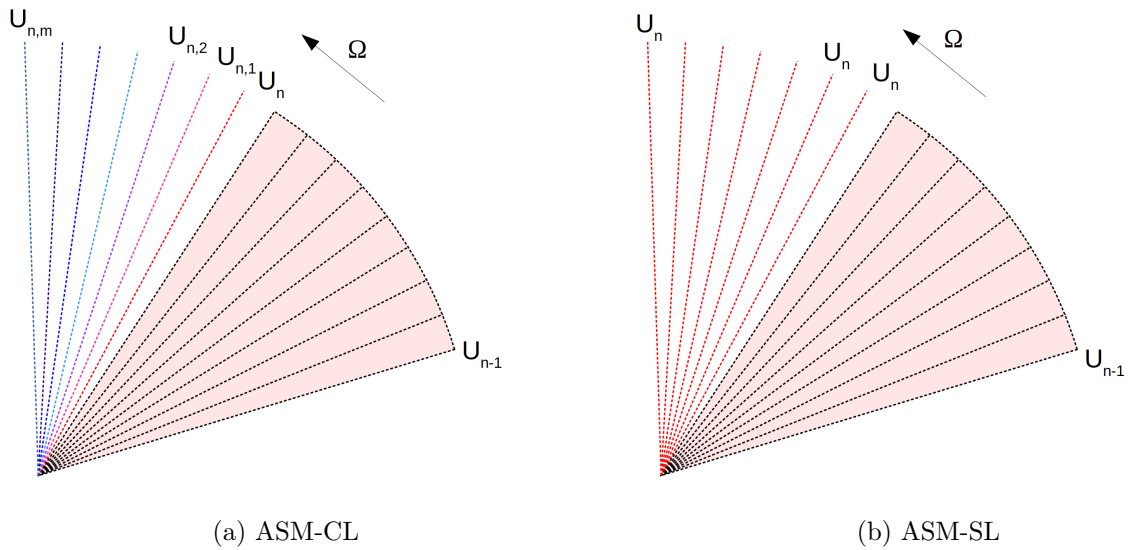


Figure 5.2: Schematic of the two working principles of the described sector methods. (a) ASM-CL: Wind speeds U are taken at every blade position within the frozen wind field. The varying colours of $U_{n,m}$ represent different wind speeds, with reddish colours indicating a stronger influence from the previous time step and blue indicating a greater distance and therefore less influence from the previous time step. The previous PALM time step (= sector) is indicated in light red. (b) ASM-SL: Wind speeds U_n are taken at the first blade position with respect to the previous sector (light red) and used for all blade positions in the current sector.

The alternative approach, denoted as ASM-SL, is to use the wind speed positions where the previous force smearing has an influence (see Fig. 5.2b), meaning, that just the wind speeds are taken at the blade positions of the first FAST time step within a PALM time step, closest to the previously smeared forces and used for all the blade positions within the current sector. This was not necessary in the ASM SWIRL method, as the increasing distance to the previously projected forces was not a problem because the induction for the respective position was added using the SWIRL method.

For the simulations described here, revision 4901 of PALM and FAST v8 was used. In FAST, the modules ElastoDyn, AeroDyn, and ServoDyn were utilized. The degrees of freedom for the blade and tower were enabled, while the rotor teeter and yaw flags were disabled. All platform degrees of freedom were neglected, i.e. set to false. The time step for all modules was consistently set to $\Delta t = 0.01$ s. In AeroDyn, the Beddoes–Leishman dynamic stall model, as proposed by [Leishman and Beddoes \[1989\]](#), was selected along with the “Dynin” option. Additionally, the tip-loss and hub-loss models were activated, utilizing the Prandtl tip-loss model [[Prandtl and Betz, 1927](#)], in the cases FAST and ASM SWIRL. Additionally, in the models ASM SWIRL and FAST, the SWIRL induction model is enabled for use, thereby applying BEM theory. [Moriarty and Hansen \[2005\]](#) describes the AeroDyn model in FAST, which utilizes BEM theory for induction calculations. The induction factors derived from the SWIRL model are based on the research by [Harman \[1994\]](#).

5.2 Investigation of the NWC method in ALM and ASM

5.2.1 Model verification in laminar flow

A laminar and homogeneous case with a constant wind speed of 8 ms^{-1} is considered, comparable to the simulations from [[Meyer Forsting et al., 2019, 2020](#)]. In addition to the simulations with the described model framework, a standalone simulation of FAST, without coupling to PALM, is conducted and serves as a reference.

For the PALM simulation a resolution of 5 m and a grid size of 384×192 grid points in the horizontal direction and 192 with stretching of the grid in vertical direction is used and the boundary conditions are set to cyclic. More details of the set-up and the test case are provided in [[Krüger et al., 2022](#)].

The laminar case was simulated using different model variations: simulations of an ALM with and without NWC, the ASM-CL with and without NWC and the ASM-SL with and without NWC were performed. In Fig. 5.3 the results of the power output after the initial turbine spin-up are shown. The first 100 s of the simulations show the spin-up of the turbine, which depends in all methods on the initialization values in FAST and is not considered of interest in this study. The simulation, denoted as FAST, which serves here as a reference, coincides well with the published value of 1876 kW for the NREL 5 MW turbine at 8 ms^{-1} [[Jonkman et al., 2009b](#)]. The ASM-CL (NWC) simulations were terminated early due to unpromising results, specifically a significant overestimation of power output, even with the NWC applied. In the ASM-CL method, the influence of forces from the previous time step decreases as the current PALM time step progresses. Consequently, wind speeds are sampled that exceed those actually experienced by the rotor blade, leading to an overestimation of power output.

Similarly, the ALM simulations were halted early for the same reason: an overestimation of power output. FAST yields a power output of 1855 kW after the turbine has fully adapted to the flow and its characteristics have reached a stationary state. The ALM without correction leads to a power

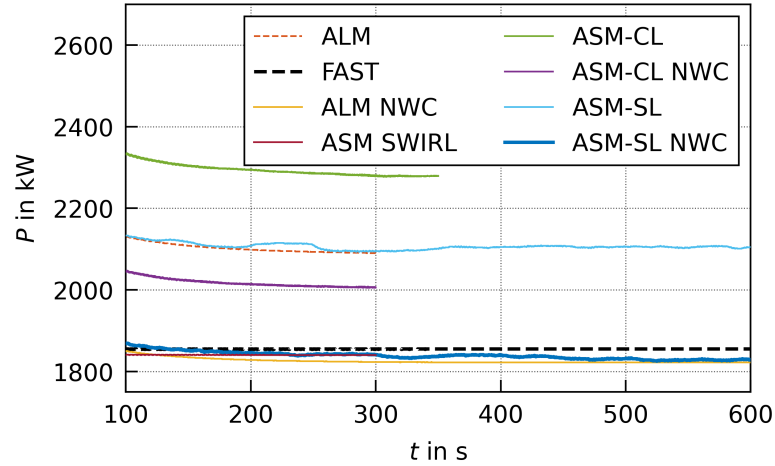


Figure 5.3: Comparison of ALM, ALM with NWC and ASM with NWC for the power output of the 5 MW NREL turbine in laminar conditions with 8 ms^{-1} .

value of 2090 kW, which is an overestimation of 13%. Using the NWC for the ALM lowers the power output.

The model ASM SWIRL [Krüger et al., 2022] reaches a good result compared to FAST. The power output of the ASM-CL is observed to be excessively high, primarily attributable to two factors. Firstly, the model partly lacks the influence of forces from the previous time step, thereby overestimating the wind speed, see e.g. Fig. 5.2a. Additionally, no correction for the missing induction is implemented. Using the NWC the power output can be lowered, yet it remains high due to the increasing distance from the forces exerted during the previous time step.

The power output of the ASM-SL coincides with the overestimated power output of the ALM. This is expected for the laminar case, as the distance between previous forces and new positions is the same in both models and both equally lack a further correction of the wind speeds. The ASM-SL (NWC) simulations seem to enhance small fluctuations of the power (see Fig. 5.3). This may be caused by the new method of extracting wind speeds from the frozen wind field (see Fig. 5.2b). It is possible that this method amplifies conditions, like structures in the wind field, that are already present in the wind speeds near the previous time step, as these wind speeds are used multiple times in FAST during one PALM time step. However, the variance remains small compared to the mean value. Simulations using the ASM-SL with NWC, denoted as ASM-SL NWC, agree well with the FAST reference curve and the mean power produced by the ALM NWC.

Displaying the parameters along the blade, as shown in Fig. 5.4a to Fig. 5.4d, motivated a deeper investigation into the relevance of the blade resolution, i.e. the number of blade elements. The findings can be found in Appendix A.1, showing a strong dependency of the results on the resolution specifically of the tip. Figures 5.4a to 5.4d shows the angle of attack, the forces and the lift coefficient across the blade, averaged from 200 s until the end of the simulations.

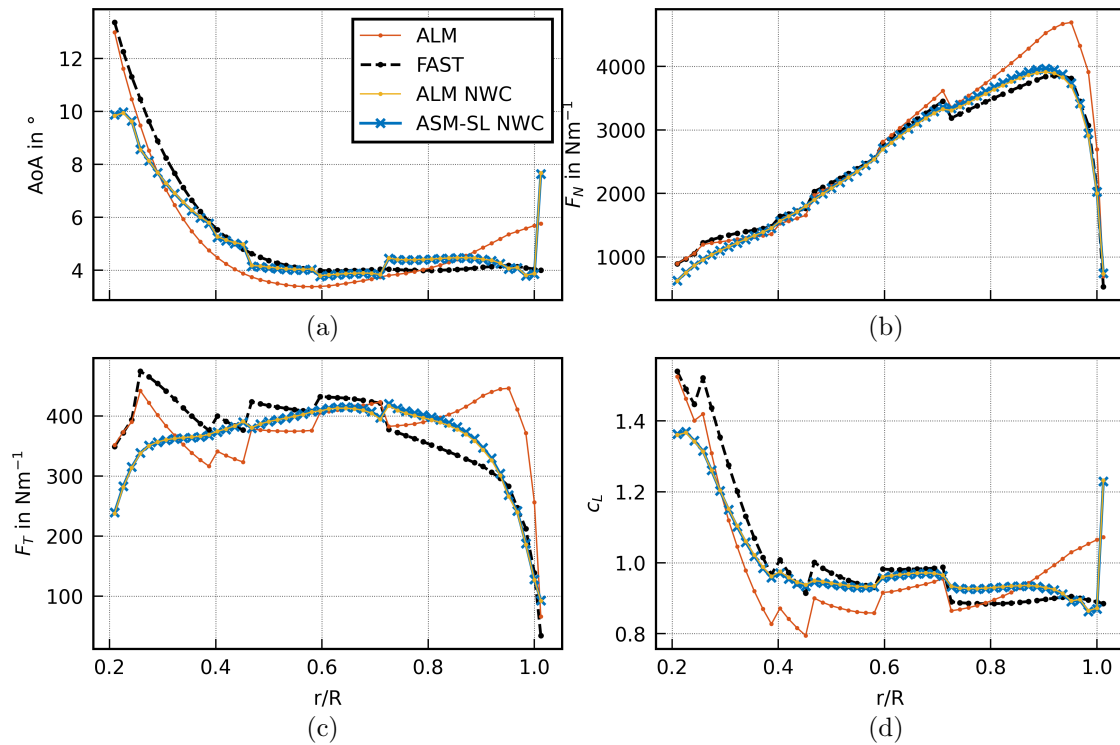


Figure 5.4: Comparison of (a) the angle of attack (b) the normal force along the blade normalized by the blade element width (c) the tangential force along the blade normalized by the blade element width and (d) the lift coefficient, averaged from 200s until the end of the simulations, for an ALM without any correction, FAST, ALM with NWC and the ASM-SL with NWC.

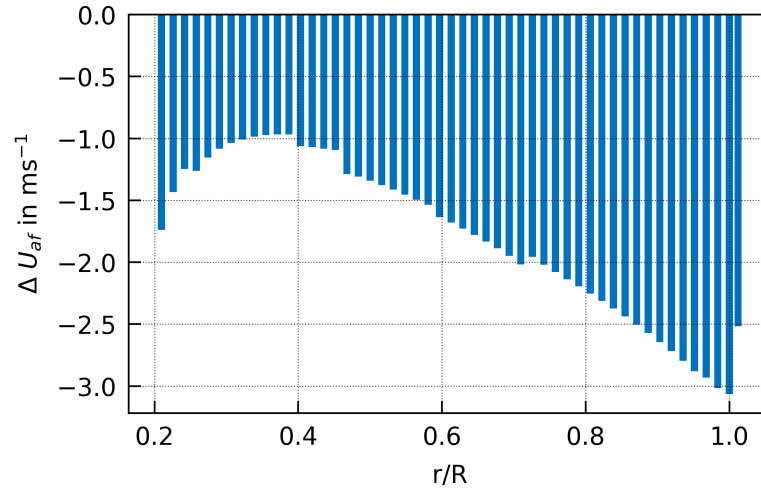


Figure 5.5: Wind speed difference between ASM-SL with and without NWC, averaged from 200 s until the end of the simulations.

Overall, the results of the ASM-SL NWC resemble the ones of the ALM NWC with the corresponding 62 nodes very closely. Figures 5.4b and 5.4c show the normal and tangential forces acting along the blade in comparison for ALM, FAST, ALM NWC and ASM-SL NWC. The more smoothed curve of the forces of the corrected model variations in comparison to the ALM, correspond to the observations by Meyer Forsting et al. [2019] for the corrected ALM. For ALM and FAST, it is observed that the angle of attack has a smooth curve, while the forces and lift coefficient have a ragged curve. However, when the NWC is used, the forces show smoother curves and the angle of attack becomes ragged. This is likely related to the turbine model and the airfoil data, specifically the lift and drag coefficients. The NWC incorporates the same airfoil information, so that it is considered not only in FAST, but also in PALM in the calculations. The additional use of airfoil information in PALM within the NWC could amplify issues and inconsistencies in the data, potentially altering the quality of the NWC. This behavior could probably be improved by using a different interpolation method for the airfoil information, but it does not impact the quality of the presented results and is therefore not further investigated in this study. Additionally, Fig. 5.4d shows the lift coefficient, which is also influenced greatly by the NWC. In Appendix A.1 similar plots for the dynamic pressure and the drag coefficients can be seen.

In Fig. 5.5 the effect of the NWC on the wind speeds along the blade is illustrated. The wind speed is reduced up to 3 ms^{-1} at the tip at a mean free stream velocity of 8 ms^{-1} .

For the laminar inflow condition, we conclude, that the ASM-SL NWC resembles the results of the ALM NWC. Both models show results, that coincide well with the reference value of FAST on its own.

5.2.2 Model verification in turbulent flow

A key challenge for modelling an ASM in turbulent flows are the varying wind speeds within a computed sector. To evaluate the model's performance, a turbulent test case was simulated using LES, with an average wind speed of 7.4 ms^{-1} at hub height. With a resolution of 4 m and $1200 \times$

480 grid points in the horizontal directions and set to a neutral flow, meaning a constant potential temperature over height. For verification of the ASM-SL NWC, the ASM SWIRL model results serve as a reference and are plotted as a bold red line in Fig. 5.6.

Figure 5.6 shows that the obtained power time series of the ASM-SL concurs roughly with the course of the ALM. This is interesting in terms of the deficit that the ASM-SL might have due to using the same wind speeds multiple times within one sector, in contrast to the ALM, where new wind speeds are communicated for every FAST time step.

When using the NWC in case of the ASM-SL the power output is reduced and is similar to the power output of the ASM SWIRL, which has shown good results in comparison to measurement data. Therefore, it can be concluded that the ASM-SL NWC results in a reasonable power output even in a turbulent flow and is worth further testing and comparing to measurement data.

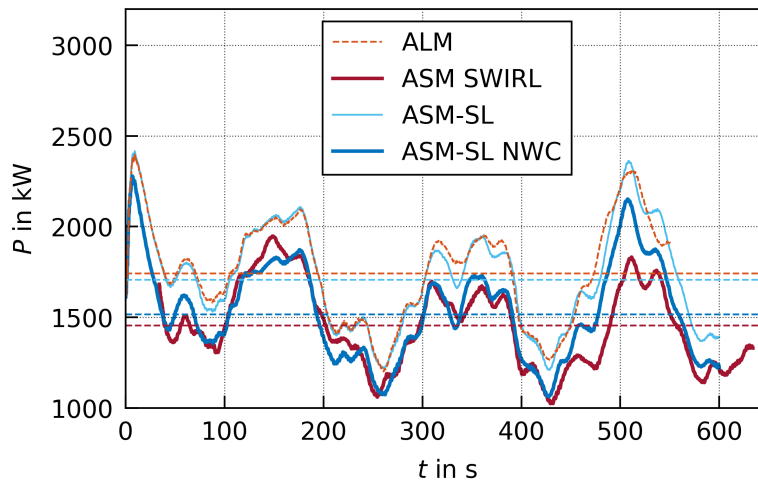


Figure 5.6: Comparison of different model variations for the power output of the 5 MW NREL turbine in turbulent conditions.

5.2.3 Verification of the ASM-SL NWC in the wake of another turbine

In horizontally heterogeneous wind conditions the assumptions of the ASM SWIRL, using Taylor's frozen eddy hypothesis, are not valid anymore. As an example, a wake situation is simulated involving two eno114 3.5 MW turbines (denoted as: upstream T1, downstream T2) positioned in a straight line in the main wind direction. This situation is simulated both with the ASM SWIRL and with the ASM-SL NWC, whereby both turbines are simulated with the same model for each simulation. A turbine spacing of four rotor diameters is tested as well as eight rotor diameters, resulting in a total of four simulations. The flow in the LES was set to a neutral boundary layer, for more details see the case NBL in the section 5.3.

In this wake situation the model ASM SWIRL uses wind speeds from within the wake of T1, upstream of turbine T2, while the wake recovers until it reaches T2. This wake recovery is not taken into account in Taylor's frozen eddy hypothesis, leading to potentially too low wind speeds at the downstream turbine T2. As verification data, the PALM wind field at the position of T2 is extracted

and used in combination with FAST, labeled as PALM wnd in Fig. 5.7a and Fig. 5.7b. For this, the wind fields at the position of T2 from simulations where only T1 is present are extracted and converted into a format suitable for input into a FAST simulation. This is a decoupled version of using PALM and FAST, there is no feedback from FAST to PALM and therefore no information about the downstream turbine in the wind field.

Figures 5.7a and 5.7b show the time series of the power output for the turbines T1 and T2 for the models ASM SWIRL, ASM-SL NWC and the reference PALM wnd. The time series for ASM SWIRL is time-shifted in the plot to make it comparable to the other methods. The time shift was calculated based on the wind speed at hub height and the distance between the velocity sampling point and the turbine. This adjustment accounts for wind speeds being taken in front of the turbine, causing the wind field structures to appear to reach the turbine earlier than in the actual wind field. It can be seen that the upstream turbine T1 (solid lines) react very similar to the inflow in both ASM models, which is consistent with the previously made observations (see section 5.2.2). The power output of the downstream turbine T2 (dashed lines) differs substantially, especially in the case of the narrow spacing. In the narrow turbine spacing, the wake recovery is less advanced before reaching the downstream turbines [Yang et al., 2015], highlighting the relevance to capture such effects in models.

It can also be observed that at T2, the differences between ASM SWIRL and the reference PALM wnd are greater than those between ASM-SL NWC and the reference. This result is plausible given the assumptions in ASM SWIRL and leads to the conclusion that the ASM-SL NWC model is better suited for delivering results in a wake situation.

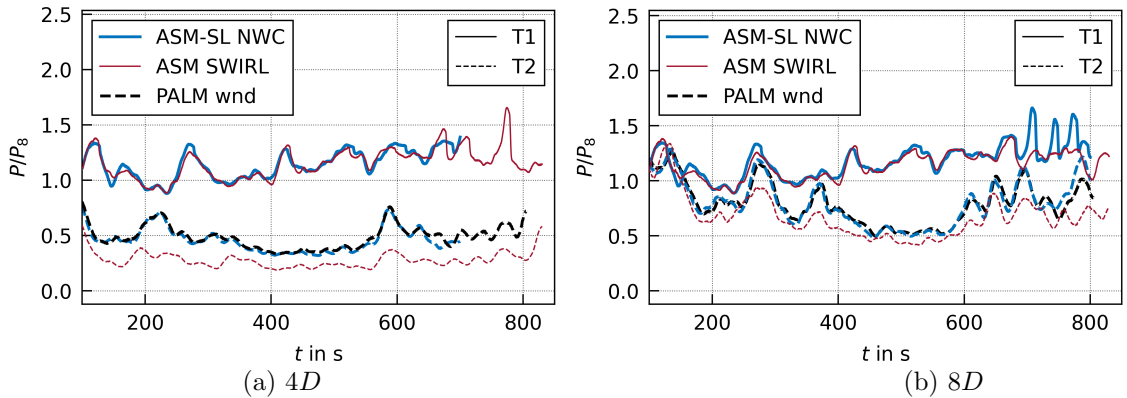


Figure 5.7: Comparison of power output for a wake situation with (a) a distance of $4D$ and (b) a distance of $8D$, the solid lines show the result of the upstream turbine T1, the dashed lines the downstream turbine T2. Additionally to the results of the sector models, results of a FAST simulation for T2 using an inflow field generated from the PALM wind field is shown in black.

Figure 5.8 compares the power output statistics over a 600-second interval, starting at 100s of simulation time. To ensure a fair comparison of the turbine reaction, for the calculation of the ASM SWIRL statistics the shifted time series is used, as it is also plotted in Fig. 5.7a and Fig. 5.7b. In addition to a difference in the means of the power output, there is also a difference in the standard deviation, which is an indicator of the turbulence intensity TI. The shape and magnitude of the ASM-SL NWC plot align well with the reference PALM wnd, indicating that a similar wind speed

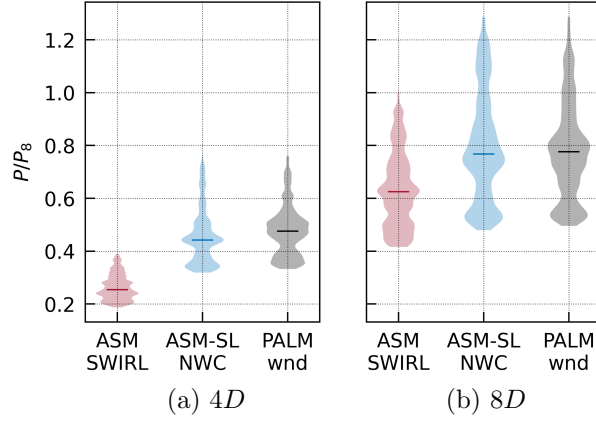


Figure 5.8: Comparison of the statistics of the normalized power time series of ASM SWIRL, ASM-SL NWC and PALM wnd for the turbine spacing of (a) $4D$ and (b) $8D$. Shown is the median and spread of the values of the above mentioned simulations.

and TI were used to calculate the turbine power. However, the statistics of the ASM SWIRL differ from those of the PALM wnd. This discrepancy is due to not only the lower wind speed used in the calculation, which results in underestimated power, but also differences in other turbulence structures.

The reference PALM wind data, which represents the wind conditions and turbine response at position T2, closely matches the results of the ASM-SL NWC. Therefore, it can be concluded that the ASM-SL NWC is well-suited for modeling wake situations.

5.3 Validation with measurement data of a single eno114 3.5 MW turbine

This section compares the proposed modelling framework with measurements under free inflow conditions. This comparison with measurements is intended to determine whether the validation from Krüger et al. [2022] is transferable and also valid for the modelling framework presented here.

Table 5.2: Setup of the precursor simulations: Size of the model domain in streamwise x , spanwise y and vertical z direction, grid size Δ , cooling rate $\Delta\Theta/\Delta t$, geostrophic wind speed components at the surface in x - and y -direction u_g , v_g and total simulated time t_{end} .

	x	y	z	Δ	$\Delta\Theta/\Delta t$	u_g	v_g	t_{end}
	[m]	[m]	[m]	[m]	[K h ⁻¹]	[m s ⁻¹]	[m s ⁻¹]	[s]
NBL	5184	2304	2928	4	0	10.0	-4.25	93600
SBL	1440	960	616	4	-0.25	9.5	-5.17	46800

In [Krüger et al., 2022], the presented coupling ASM SWIRL was compared to measurement data from an eno114 3.5 MW turbine located in northern Germany. The same simulation set-up is here used again to investigate how the ASM-SL NWC compares to the measurement data. For further

Table 5.3: Resulting flow parameters after reaching a stationary state in the precursor simulations, averaged over 3600s: The magnitude of the wind speed at hub height averaged over the model domain U_{92m} , turbulence intensity calculated at one position in 92 m height TI_{92m} , shear parameter α (based on the power law $u_2 = u_1 \left(\frac{z_2}{z_1}\right)^\alpha$ for the relation of wind speeds at different heights), Obukhov length L in a height of 2.3 m (height is chosen for comparison to the eddy-covariance data at the measurement site) and boundary layer height z_i .

	U_{92m}	TI_{92m}	α	L	z_i
	[m s^{-1}]	[%]	[]	[m]	[m]
NBL	8.6	10.1	0.15	1228698	550
SBL	8.4	5.6	0.28	102	180

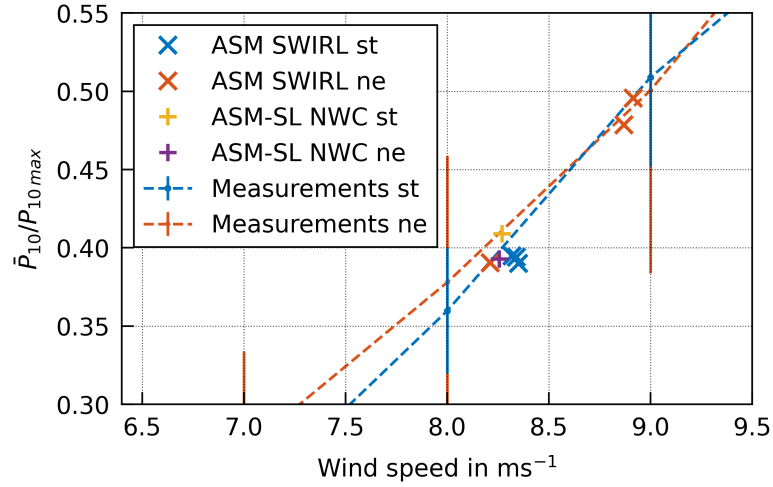


Figure 5.9: Extract of the power curve, normalised by the maximum 10 min power, determined from the measurement data, divided into stable (st) and neutral (ne) conditions. Comparison of the measurement data, the simulation data of ASM SWIRL and the new version ASM-SL NWC. The measurement and ASM SWIRL data are sourced from Krüger et al. [2022].

information concerning the atmospheric conditions at the measurement site, how the simulations compare to them, and the comparability of the simulations with the selected time interval of the measurement data, please refer to [Krüger et al., 2022]. Idealized simulations were performed to match the prevailing inflow conditions of the eno114 3.5 MW turbine based on the measured data. One case with neutral and one case with stable stratification were simulated. The set-up of the precursor simulations is detailed in Table 5.2 and Table 5.3 shows the resulting atmospheric conditions. The precursor simulations are calculated with cyclic boundary conditions and no turbine in order to reach a stationary flow that can serve as a starting point for the simulations including a turbine.

In Fig. 5.9 the result of two simulations of the ASM-SL NWC can be seen in comparison to ASM SWIRL and the measurement data. No large deviations can be observed between the model versions. The stable case shows a slight increase in the power output of ASM-SL NWC compared to

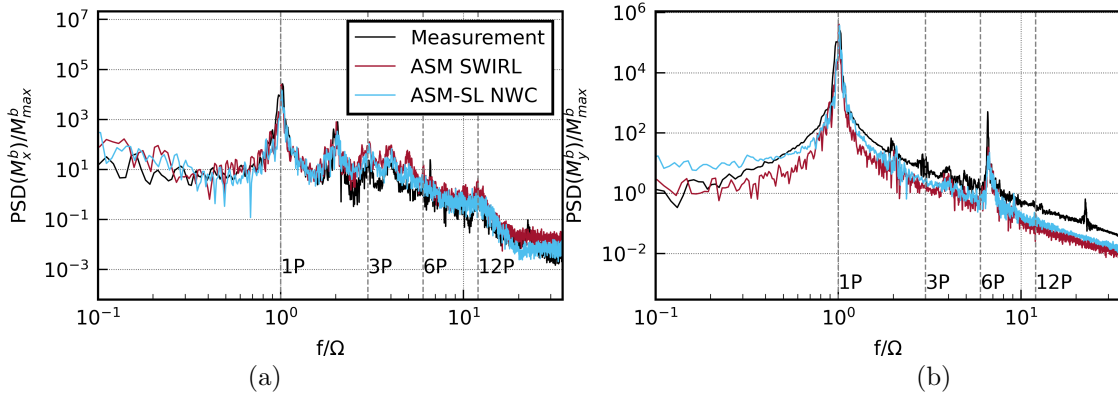


Figure 5.10: Spectrum of (a) the blade root bending moment out-of-plane M_x^b and (b) the blade root bending moment in-plane M_y^b . Comparison of measurement data and simulations of the models ASM SWIRL and ASM-SL NWC. The data are normalised by the maximum value of the blade root bending moment. The frequency is normalised by the rotor speed. The measurement and ASM SWIRL data are sourced from Krüger et al. [2022].

the simulations of the ASM SWIRL. This could be caused by the reduced mixing within a sector, which might have an effect due to the method of retrieving the wind speeds (c.f. Fig. 5.2a and b). However, the difference to the measurement data remains the same. Additionally, the performance of the new model version was analyzed using load data, with the blade loads illustrated in Fig. 5.10 as an example.

Overall, the ASM-SL NWC shows the same quality of performance as the ASM SWIRL for the selected case and a good agreement in comparison to the measurement data. For a more detailed analysis of the load spectra, please refer to Krüger et al. [2022]. In summary, the existing differences in the spectra can be attributed to variations in the turbine model, such as a fixed blade imbalance and pitch offset between the blades in FAST, as well as discrepancies between the tower model and actual tower behaviour. Additionally, the 6P peak is significantly influenced by the shear over the rotor area, which varies slightly between the measurements and the simulations (see Appendix Krüger et al. [2022]). It can be concluded, that the validation of the simulation in Krüger et al. [2022] can be extended for the proposed method ASM-SL NWC.

5.4 Conclusions

A modeling framework has been developed to simulate atmospheric flows while providing detailed wind turbine dynamics and loads in a computationally efficient way. This framework combines the ASM presented in Krüger et al. [2022] with the NWC correction method proposed by Meyer Forsting et al. [2020]. Previous studies, such as Mohammadi et al. [2024a], have demonstrated that the ASM can achieve results comparable to an ALM. In this study, the framework integrating an ASM with NWC and an aeroelastic code has been validated, demonstrating high-quality results under realistic flow conditions.

To implement this framework, the NWC method was first examined within the ALM PALM-FAST coupling, which involves a coupled time step between FAST and PALM. Subsequently, an extension of

the ASM was developed and evaluated to enable the use of NWC within this model. This extension, referred to as ASM-SL NWC, was compared to other models and validated using measured data from an eno114 3.5 MW turbine. Additionally, wake scenarios with varying distances between turbines were investigated to assess the effectiveness of the new coupling method.

The developed framework delivers accurate results for both laminar and turbulent test cases when compared to reference models. The NWC applied in the ASM-SL NWC effectively corrects wind speeds that would otherwise be too high, preventing overestimated power output. The framework's strong performance in turbulent test cases confirms the validity of the spatial simplifications introduced by the sector-based approach.

In wake scenarios, the ASM-SL NWC demonstrates superior performance compared to the earlier coupling method ASM SWIRL, making it a reliable tool for studying detailed turbine performance, including blade and tower loads, across a wide range of atmospheric flow conditions. Comparisons between the ASM-SL NWC and reference simulations show favorable results, and validation with measurement data confirms its reliability in representing both power output and turbine loads. While the NWC is sensitive to flow conditions when applied to flexible blades [Hodgson et al., 2022], the results remain robust and consistent.

The resolution of the blade has been identified as a critical parameter influencing the quality of the simulation, as demonstrated during investigations of the NWC in the ALM coupling. Higher resolution at the blade tip yields better results, whereas resolution in the blade's middle section and near the hub has less impact on accuracy.

Thus far, the framework has been tested primarily under mid-range wind speed conditions. Future research should expand testing to include scenarios with both lower and higher wind speeds, as such conditions may involve different turbine control strategies. Further exploration is also needed to technically evaluate the coupling, including the implementation and assessment of a second velocity sampling option. Sensitivity analyzes concerning grid resolution and varying TSR values are essential to confirm the generalizability of the framework.

On the technical front, an upgrade from FAST v8 to OpenFAST and AeroDyn v15 is planned, as this transition is expected to further enhance the accuracy of the aerodynamic calculations.

Appendix

A.1 Investigation of the effect of the blade resolution of the NREL 5 MW turbine

When analysing the implementation of the NWC in the ALM, it was noticed that the course of the angle of attack along the blade in particular does not correspond to that in [Meyer Forsting et al. \[2019\]](#). The main difference in the set-ups of [Meyer Forsting et al. \[2019\]](#) and the ALM in this study is the resolution of the blade. For calculation of the forces and vortices along the blade, the turbine model needs to be set-up, dividing the blade into elements. Depending on the number of elements per blade, the resolution is higher or lower. To study the impact of the blade resolution, we tested two additional resolutions. In addition to the 62 node blade used in the previous sections for the NREL 5 MW turbine, we investigated a coarser resolution of 17 nodes and one of 19 nodes. The case of 19 nodes is constructed, to test the importance of the resolution at particular the blade tip. As a basis, the blade with 17 nodes is utilized as the coarsest available set-up. To enhance the resolution at the blade tip, two additional elements are added, following the definition provided in the 62 blade nodes set-up. This results in a blade containing 19 blade nodes, however, this does not correspond to the used resolution of 19 nodes in [Meyer Forsting et al. \[2019\]](#), which was equally distributed along the blade.

The tested resolutions of 17, 19 and 62 nodes result in a power output of 1912 kW, 1846 kW and 1822 kW (see Table 4). These results lay close to the reference of the FAST simulation, i.e. an overestimation of 3.1% and an underestimation of 0.5% and 1.8% compared to the FAST reference simulation. The main differences lie at the tip, where the higher resolved blade, e.g. 62 nodes, captures more of the effects than the lower resolved blade, e.g. 17 nodes. The Fig. 11a to Fig. 11d show the angle of attack, forces and lift coefficient along the blade. The plots reflect the high impact of the NWC towards the blade tips, underlining also the importance the resolution at the blade tip.

The stand-alone FAST simulations were calculated with a resolution of 62 nodes per blade. The other resolutions of 17 and 19 nodes per blade were tested as well to determine the effect on the simulation which is regarded as the reference. The influence of the resolution can also be seen here, 17 nodes per blade yields a power of 1874 kW and 19 nodes per blade 1876 kW (see Fig. 13 in the Appendix). The difference between 17 and 19 nodes in comparison to 62 nodes per blade lie at about 1%. This should be kept in mind when regarding this as a reference, nevertheless the magnitude of the FAST stand-alone simulation can serve as a good indicator for the quality of the tested models. Since all simulations in [Krüger et al. \[2022\]](#) were carried out with a resolution of 62 blade nodes, the model with 62 nodes is also used in this study, in the ASM as well as in FAST, to ensure comparable simulations.

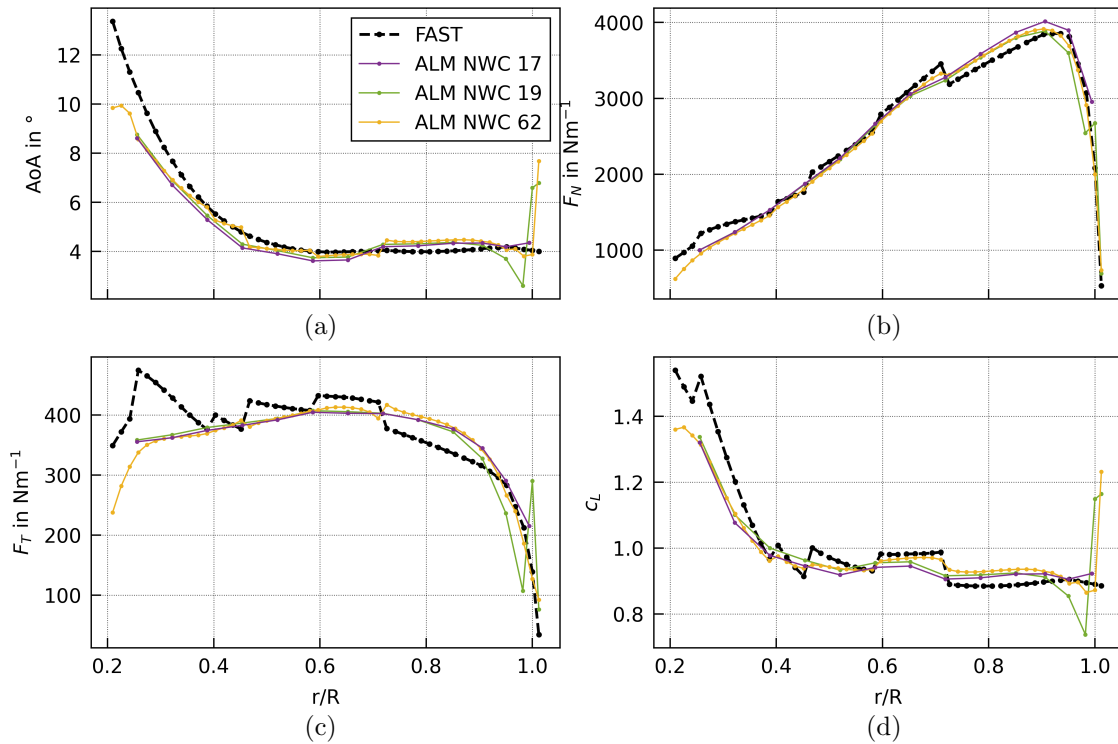


Figure 11: Comparison of (a) the angle of attack (b) the normal force along the blade normalized by the blade element width (c) the tangential force along the blade normalized by the blade element width and (d) the lift coefficient, averaged from 200s until the end of the simulations, for FAST and the ALM NWC with the blade resolutions of 17, 19 and 62 nodes.

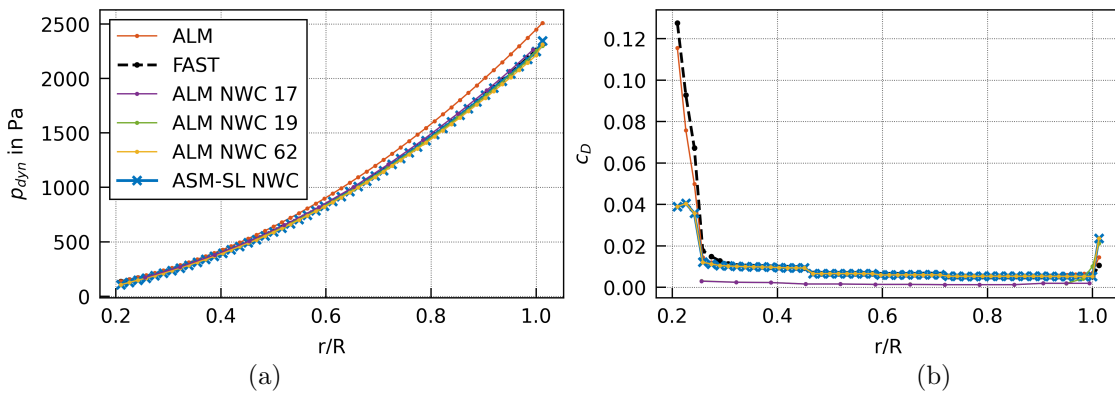


Figure 12: Comparison of (a) the dynamic pressure and (b) the drag coefficient, averaged from 200s until the end of the simulations, for ALM, FAST and the ALM NWC with the blade resolutions of 17, 19 and 62 nodes, as well as ASM-SL NWC.

Table 4: Summary of the blade resolutions used in [Meyer Forsting et al. \[2019\]](#), denoted with M-F, and here, as well as their corresponding power output for a laminar case of 8 ms^{-1} .

Resolution	Description	Power at 8 ms^{-1} in kW
M-F 9	equally distributed along the blade	2130
M-F 19	equally distributed along the blade	1980
17	equally distributed along the blade	1912
19	17 nodes as basis, higher resolution at tip	1846
62	equally distributed along the blade	1822
FAST	using 62 equally distributed nodes	1855

A.2 Power output of FAST depending on the blade resolution of the NREL 5 MW turbine

The following plots show the comparison of the FAST stand-alone simulations as well as the dynamic pressure and the drag coefficients along the blade in case of the laminar case described in section 5.2.

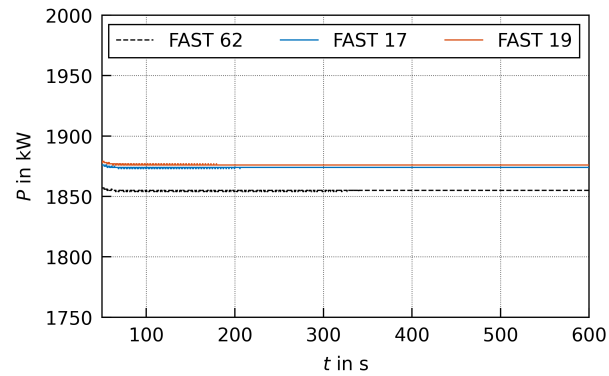


Figure 13: Power time series of the FAST stand-alone simulations with steady wind inflow conditions for the blade resolutions of 62, 17 and 19 nodes per blade.

Chapter 6

Structures in flows downstream of surface heterogeneities and their effect on wind turbines

This chapter will soon be submitted to a peer-reviewed journal for publication.

Contributions: I conducted a series of idealized simulations that excluded turbines, as well as all simulations that included turbine dynamics. These simulations incorporated changes in surface roughness and temperature within the model domain, necessitating careful integration into the LES code. I successfully modified the code to accommodate these adjustments. I adapted the PALM-FAST model chain to the IEA-15-240-RWT turbine. I conducted the simulations and carried out a comprehensive analysis of the results. I wrote the first draft and generated the figures.

This chapter aims to investigate the impact of coastal heterogeneities on wind flow and their effects on wind turbines. Using LES, idealized coastal transitions are systematically modeled to study the formation of lateral gradients in wind speed and turbulence. These gradients manifest as alternating stripes of increased or decreased wind speeds, depending on the surface conditions. The persistence and extent of these gradients vary: changes in roughness or temperature alone tend to dissipate after a few kilometers, whereas combined effects, such as a warm, smooth surface adjacent to a cool, rough surface, can produce gradients visible over tens of kilometers. These heterogeneities also drive circulations that transport flow properties between different vertical layers, further influencing the downstream flow.

Additionally, simulations using the PALM-FAST coupling variant ASM-SL NWC as described in Chapter 5 were performed to investigate the impact on wind turbine dynamics. These coupled simulations reveal that localized variations in turbulence intensity (TI) and vertical wind speed can significantly affect turbine behavior, emphasizing the necessity of considering coastal influences in wind farm planning and operation.

6.1 Numerical Setup and Methodology for Turbine Calculations

For this study the LES model PALM [Maronga et al., 2020] was used to simulate the flow over idealized surface heterogeneities, see subsection 6.1.1. To be able to understand the effect on wind

turbines a coupled set-up of PALM with the aeroelastic model FAST [Jonkman and Buhl Jr., 2005] was utilized, see subsection 6.1.2.

6.1.1 LES Model PALM General Setup

In order to obtain a stationary turbulent flow as the inflow of the heterogeneities, a preliminary simulation was conducted using cyclic boundary conditions without heterogeneities. This preliminary run utilized a grid size of 10 m and encompassed a model area of $x = 1024$, $y = 512$ and $z = 256$ grid points, where x represents the main flow direction, y is perpendicular to x , and z denotes the height (see also Table 6.1 for the geostrophic wind values and other simulation settings). The grid height remained constant up to 1200 m, after which a stretching was applied, reaching a maximum grid height of 80 m. The roughness length was set to 0.1 m and the ground temperature was uniformly set to 290.0 K, with a surface heat flux of $0.0000001 \text{ K ms}^{-1}$. No vertical temperature gradient was set up to a height of 900 m; above this, a piece-wise temperature gradient of $2 \text{ K}/100 \text{ m}$ was applied from 900 m to 1000 m, followed by a gradient of $0.35 \text{ K}/100 \text{ m}$ above 1000 m. These settings, combined with the geostrophic forcing, resulted in the development of a turbulent flow suitable for the subsequent simulation of surface heterogeneities.

The main-run utilizes non-cyclic boundary conditions in the main flow direction, in order to not feed structures, that appear at the outflow back into the inflow. The turbulence recycling method in PALM was used to contain a turbulent inflow, see Maronga et al. [2015, 2020]. The turbulent recycling method utilizes an inflow area to sustain turbulent flow. For this purpose, a recycling plane is defined at which the turbulent signal is extracted and added to the mean flow. The recycling plane needs to have a sufficient distance to the inflow for the turbulent flow to develop, at the same time a distance to the heterogeneities needs to be kept, so that they do not influence the turbulence signal at this position. Perpendicular to the main flow direction cyclic boundary conditions were used. The model domain of the main run, see Fig. 6.1, containing the surface heterogeneity, has a resolution of 10 m, while having 6144 grid points in the x -direction, which is the main flow direction. Perpendicular to that, in y -direction the domain has 1280 grid points and in vertical direction (z) 256 grid points, see also table 6.1. In z -direction a vertical grid stretching is employed starting at the height of 1200 m, having a maximum cell height of 80 m. The temperature gradient was set according to the one of the preliminary run. Looking from the inflow in x -direction, the first 22 km is a zone of higher roughness length ($z_0 = 0.1 \text{ m}$), representing an onshore area. Within this inflow zone the turbulence recycling plane is positioned at $x = 10 \text{ km}$, to use for the inflow. The size of the area upstream of the heterogeneities was selected to ensure that the flow has sufficient space to fully develop and that the precursor run area can be accommodated. Additionally, the recycling plane should not be located in an area that is influenced by the heterogeneities, but far enough from the inflow for turbulence structures to develop.

Along the x -direction, the next 10 km contain areas of heterogeneity, referred to as patches, with varying widths. These patches are defined as rectangular areas that are homogeneous within each rectangle but differ in surface roughness lengths and surface temperatures from each other. The patches alternate in the y -direction, creating a pattern of varying surface properties. The width in the y -direction was chosen so that different numbers and widths of heterogeneities are possible. This allows for the repeated introduction of patches that are the size of the boundary layer height within the area. But also, it is possible to prescribe surface patches that have a width which is

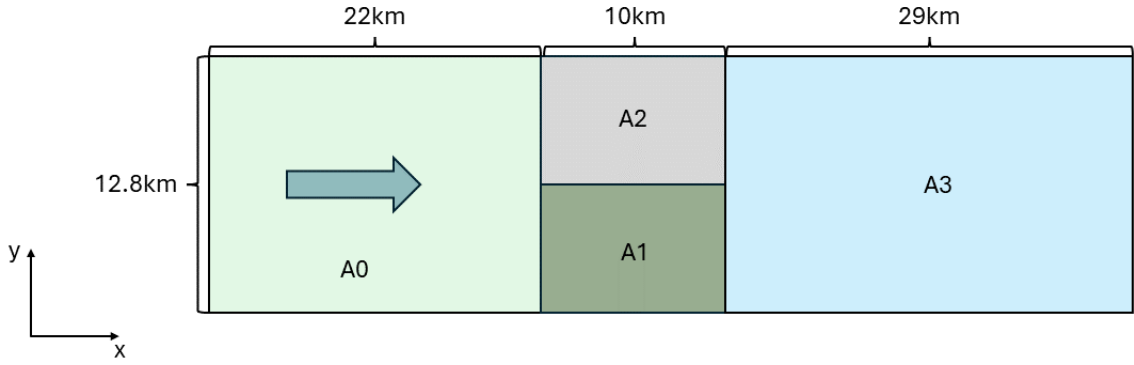


Figure 6.1: Setup of the model domain having idealized surface heterogeneities. The inflow area A0 has the roughness length $z_0 = 0.1$ m, the area behind the heterogeneity patches A3 has the roughness length $z_0 = 0.0002$ m. The roughness length and surface temperature vary in the areas A1 and A2.

a multiple of the boundary layer height. Behind these patches an area of lower surface roughness begins ($z_0 = 0.0002$ m), representing an offshore region. It covers nearly 30 km of downstream model area, which is sufficiently large to encompass offshore regions typically used for wind farms.

Table 6.1: Setup of the simulations: Size of the model domain in streamwise x , spanwise y and vertical z direction, grid size Δ , geostrophic wind speed components at the surface in x - and y -direction u_g , v_g and total simulated time t_{end} . All simulations were performed at latitude setting 54.5° .

	x	y	z	Δ	u_g	v_g	t_{end}
	[]	[]	[]	[m]	[m s^{-1}]	[m s^{-1}]	[s]
PR	1024	512	256	10	9.961	-2.908	216000
MR	6144	1280	256	10	9.961	-2.908	14400

Simulated cases

A number of different main runs were carried out, for an overview see table 6.2. Varying mainly in different distributions of surface temperature and the width of the heterogeneities. These adjustments to the surface properties are made in the dynamics and surface module of PALM.

The tested widths of the heterogeneities are based on the boundary layer height ($z_i=900$ m), so patches with a significantly smaller width (320 m), patches slightly larger than the boundary layer height (1280 m) and patches with a significantly greater width (6400 m) were selected. The choice of roughness length represent a typical transition from land to sea with a roughness length of 0.1 m in the inflow area, indicative of agricultural use or sparse tree cover. The heterogeneities differ in a rougher and a smoother area, which corresponds, for example, to urban use and flat grassland. The temperature differences are a conservative approach of 2 K difference, so that it can be investigated whether even a small difference causes an effect. To illustrate the influence on the turbines more clearly, two cases featuring more significant temperature differences of 5 K (128wc5K and 640wc5K) are tested. In this case, the temperature deviations are not symmetrically distributed across the

patches; A1 is 0.5 K warmer, while A2 is 4.5 K colder than the inflow region. This approach simulates a more realistic scenario compared to a symmetrical distribution. These scenarios are discussed in section 6.3.

Table 6.2: Summary of the performed simulations. The abbreviation for each run consists of the width of the patches in grid cells and further distinguishing letters (b: base, c: cold, w: warm, st: stable, us: unstable, T: temperature, l: long).

Name	A0		A1		A2		A3
	width/m	T_{surf}	z_0	T_{surf}	z_0	T_{surf}	T_{surf}
	[m]	[K]	[m]	[K]	[m]	[K]	[K]
32wc	320	290.109	0.01	290.609	1.0	289.609	290.109
128b	1280	prerun	0.01	prerun	1.0	prerun	prerun
128cw	1280	290.109	0.01	289.609	1.0	290.609	290.109
128wc	1280	290.109	0.01	290.609	1.0	289.609	290.109
128wc5K	1280	290.109	0.01	290.609	1.0	285.609	290.109
640b	6400	prerun	0.01	prerun	1.0	prerun	prerun
640cw	6400	290.109	0.01	289.609	1.0	290.609	290.109
640wc	6400	290.109	0.01	290.609	1.0	289.609	290.109
640wc5K	6400	290.109	0.01	290.609	1.0	285.609	290.109
640wcT	6400	290.109	0.01	290.609	0.01	289.609	290.109

6.1.2 Turbine simulations – PALM-FAST coupling

In order to investigate the influence of the resulting flow structures on wind turbines, a model system was selected that represents both the atmospheric conditions and the turbines well. A turbine output that is as extensive as possible is also desired, so that the power output, but also various loads can be analyzed. The PALM-FAST model framework was therefore selected, in the version ASM-SL NWC described in Chapter 5.

Specifications for this study

Due to the resolution of 10 m within the simulations of this study, and the typical application of offshore turbines up to 15 MW today, the generic 15 MW IEA 15-240 RWT [Gaertner et al., 2020] turbine was selected to be used for the simulations here. However, as this turbine is normally used in combination with FAST’s Aerodyn15 and here, within the model framework, Aerodyn14 is being used, some modifications had to be made. Based on the work in Maas [2023] a turbine model was set up in FAST consisting of airfoils that are also distributed along the blade of the NREL 5 MW turbine [Jonkman et al., 2009b]. These airfoils are also arranged along the blade of the 15 MW IEA 15-240 RWT turbine to mimic its aerodynamic properties. The controller used here is also based on that of the NREL 5 MW turbine, adapted with the data from the IEA 15 MW turbine.

The simulations containing the wind turbines is an extension of the mainrun setup. Meaning,

that once the structures in the flow are stationary after 14400 s, a subsequent simulation with the additional wind turbines is started. The turbine data is analyzed after a spin-up of the turbines of 200 s.

6.2 Downstream Effects of Systematic Heterogeneity Variations

The results of the systematic variations in heterogeneities are presented below. The first subsection focuses on all cases with a maximum temperature difference of 2 K, as shown in table 6.2. Subsequently, two specific cases are examined in greater detail.

6.2.1 Results

The flow moves downstream over different surface roughnesses in combination with different temperatures. A higher surface roughness as well as a higher temperature than the upstream surface leads to an increase in turbulence. A reduction in temperature leads to a stable stratification. A combination of properties can lead to different effects downstream. To illustrate the effects of the heterogeneities on the flow, the wind speed, its components and the potential temperature is considered and visualized in the following in various ways.

Figures 6.2 to 6.5 shows the wind speed perpendicular to the main wind direction at the coastline and at specific downstream positions, using data at a height of $z = 145$ m, which is a typical hubheight of offshore wind turbines. In the lateral direction, the y direction, the plots are normalized by the patch width, in order to consider the resulting flow localized and limited to one heterogeneity patch.

At the coastline the influence of the surface heterogeneities can be observed very clearly for almost all simulations. The simulation without a change in roughness length (640wcT, Figure 6.5) shows the smallest influence at this position, only a deviation of below 5% from the mean wind speed along y occurs (see table 5 for wind speed values in the Appendix).

Figures 6.2 to 6.5 show the wind speed alongside the horizontal wind speed component v and the vertical component w . It can be seen that the peaks in the wind speed are accompanied by peaks in v and w . The strength of the peaks in v and w differs with increasing distance from the coastline. The wind speed shows the greatest gradient directly at the coast, while the gradients of v and w develop with increasing distance from the coast. In cases 128b and 640b (see Fig. 6.2), the effects on v and w are the smallest and the gradients of the wind speed also tend to decrease faster with distance from the coastline than in the cases with additional temperature change.

The order of the temperature change, i.e. which patch is cold and which is warm, influences the effect downstream. The comparison is presented separately in Figures 6.3 and 6.4 for patch widths of 1280 m and 6400 m, respectively. A direct comparison of the 6400 m wide patches is depicted in Figure 6.5. In the wc configuration, the warmer patch has a lower roughness length, i.e. the trends are opposed at the coastline: low roughness does not lead to more turbulence, but the temperature increase leads to rising air masses and an unstable stratification. In the case of the cw setup, the warmer area has a higher roughness length, i.e. there are reinforcing trends at the coastline: higher roughness increases turbulence, and the increase in temperature also brings rising air masses. As a result, the wind speed gradients are in the cw case most pronounced at the coastline, while in the wc

case the effects at the coastline is not as pronounced, but with distance to the coastline a significant gradient in the wind speed is visible (see table 5 in the Appendix). With a patch width of 6400 m, the gradient at 20 km downstream is more pronounced for wc than for cw. However, with a smaller patch width of 1280 m, it is challenging to differentiate between the two at 20 km downstream. Particularly in cases 128cw and 128wc, a lateral shift of the peaks with increasing distance from the coastline can be observed. In the comparison between 128wc and 128cw, this lateral movement is larger for the 128cw case. To illustrate the lateral movement Fig. 16 in the Appendix shows the positions of the maxima at a height of 145 m along y direction with increasing distance to the coastline. It displays the actual lateral distances of up to 1550 m in a distance of 25 km distance to the coastline, for the case 640wc, with the 128cw and 640cw cases demonstrating the most significant lateral movement.

In the case of patches smaller than the boundary layer height here, 320 m, (Fig. 6.3) the influence downstream reduces quickly with the distance to the coast. At a distance of 10 km no distinguishing of peaks corresponding to the patches' width can be made. In cases where the patch width is in the range of or greater than the boundary layer height, it depends on the additional conditions how far the patch width is visible at the height 145 m in the wind speed. With a pure difference in roughness (Fig. 6.2), there is no clear influence of the patches visible at a distance of 20 km from the coast for the narrower patches, and minimal influence can be seen for patches of 6400 m. The plots for both 128b and 640b exhibit similar shapes across all displayed coastal distances, suggesting that there seems to be no significant dependence on the patch width.

The scenario is similar in the cw case (Fig. 6.4, where the trends, reinforce themselves, as described above. At the coastline, the gradients for 128cw and 640cw are nearly identical, indicating that the patch width has no significant impact in this case. It is only with increasing distance from the coast that slight differences in lateral wind speed start to emerge. In the 640cw case, the v -component exhibits strong gradients with increasing distance from the coast, indicating more pronounced lateral movement compared to the narrower patch case, 128cw.

The scenario differs in the case of wc. The wind speed, as depicted in Fig. 6.3, shows that a patch width below the boundary layer height (32wc) results in a single peak spanning half the normalized y -width. Conversely, larger patch widths (128wc and 640wc) yield two peaks at the patch boundaries behind the warmer patch. An adaptation to the patch conditions can be discerned between the peaks, with this effect being more pronounced at the widest tested width of 6400 m. As the distance from the coast increases, the peaks at the patch boundaries downstream of the warmer patch converge. This is already observable after 10 km in the case of 128wc, where only a single peak is evident. The wider 6400 m patch forms peaks that remain distinct up until the end of the modelled area. These peaks are also reflected in the vertical wind speed w . Figure 6.3 illustrates that the wind speed component v , directed along the y -axis, exhibits lateral movement until the peaks, that are visible in the wind speed and w have merged. In the 32wc and 128wc cases, this phenomenon predominantly occurs near the coast, whereas in the 640wc case, the lateral movement intensifies with increasing distance from the coast.

The comparison of cases 640 in 6.5 shows the different influence of pure roughness change (640b), pure temperature change (640wcT) and the two cases with roughness and temperature change (640wc, 640cw), whereby the influence of the different patch widths is disregarded. It can be clearly seen that a pure temperature change (640wcT) does not cause any strong gradients in the wind speed at a height of 145 m. Only the component v shows a stronger gradient with increasing distance from the coastline. There are no gradients in the horizontal wind speed component w for 640wcT and

640b, which is why they are not shown in this plot for better visualization of 640wc and 640cw. The w -component in cases 640wc and 640cw exhibits gradients that align with the wind speed gradients and those of the v -component.

To better understand the mechanisms behind the observed horizontal flow patterns, Fig. 6.6 shows a section in y - z -direction at the position 10 km downstream from the coastline of the wind speed component u for all simulations. The arrows show the vertical wind speed component w and illustrates the vertical transport in the flow. It can be seen that in the cases 128cw, 128wc, 640cw and 640wc the influence of the patches result in stripes of low wind speed reaching up to 500 m. In cases 128cw and 128wc, the w component shows an upward direction in regions of low u and a downward direction in areas of higher u . This pattern is not observed in smaller patches (32b) or in the case with only differences in roughness length (128b). Wider patches of 6400 m develop the area of low u at the edges of the colder patch and in the centre of the warm patch. The vertical movement does not exhibit a clear trend but an upward movement can be observed in the smaller stripes, that develop at the edges of the cold patch. A plot of the vertical wind speed w is provided in the appendix, illustrating this phenomenon without the additional depiction of u .

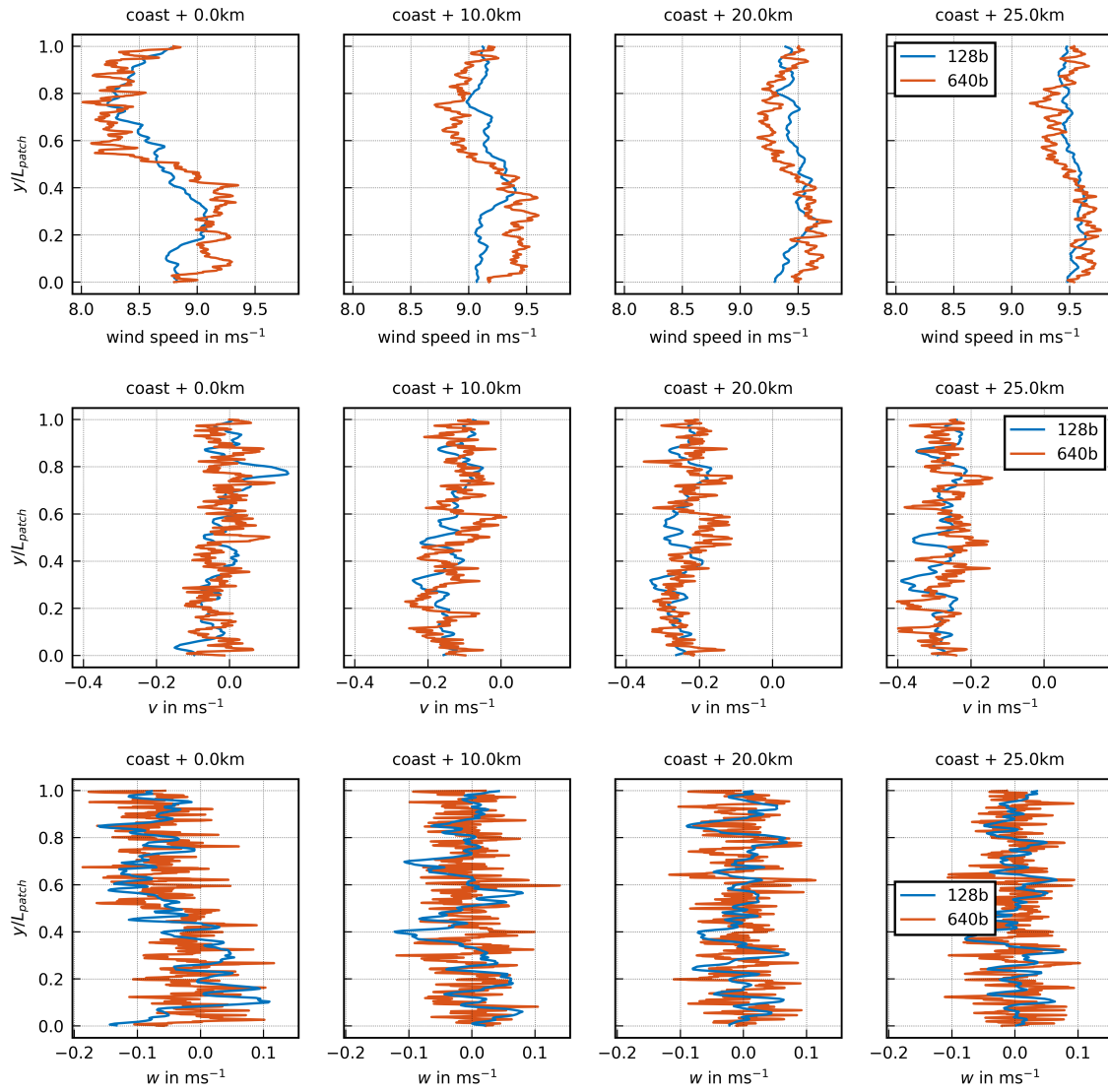


Figure 6.2: 1-hour averaged wind speed and wind speed components v and w at a height of $z = 145$ m, perpendicular to the main flow direction, taken at various positions behind the coastline for the cases 128b and 640b, containing roughness changes but no temperature gradients.

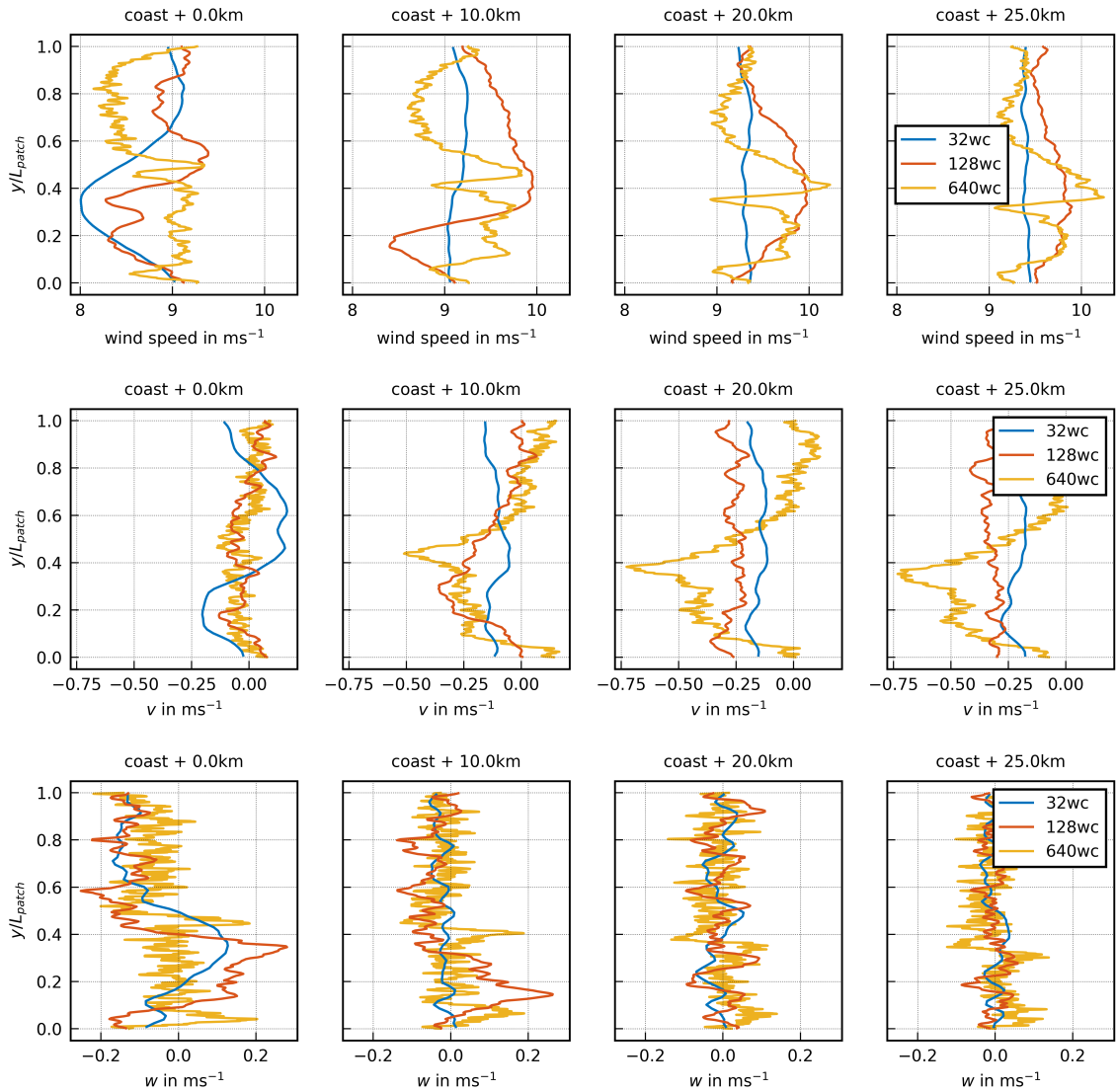


Figure 6.3: 1-hour averaged wind speed and wind speed components v and w at a height of $z = 145$ m, perpendicular to the main flow direction, taken at various positions behind the coastline for the cases 32wc, 128wc and 640wc, containing roughness changes and temperature changes.

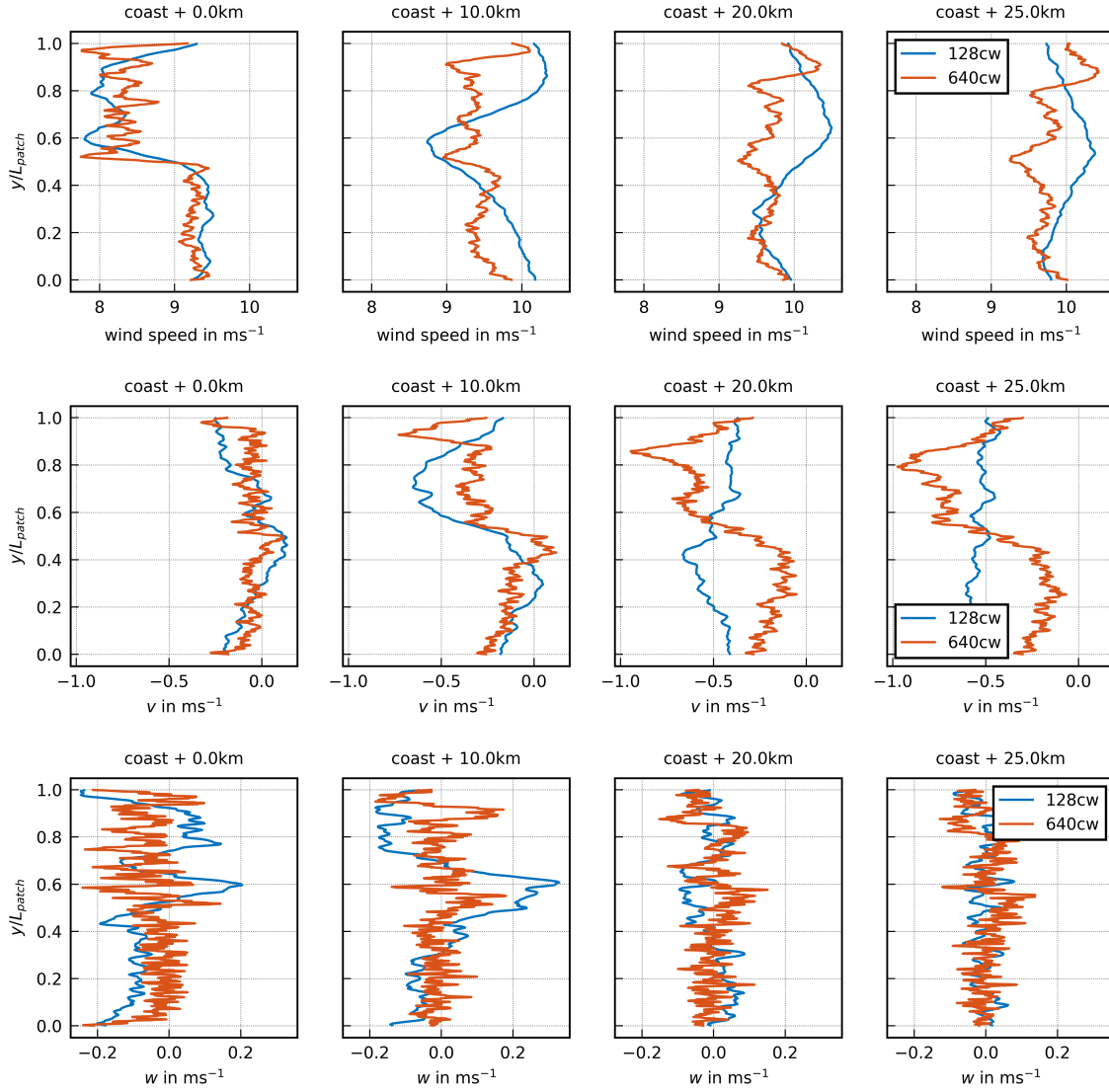


Figure 6.4: 1-hour averaged wind speed and wind speed components v and w at a height of $z = 145$ m, perpendicular to the main flow direction, taken at various positions behind the coastline for the cases 128cw and 640cw, containing roughness changes and temperature changes.

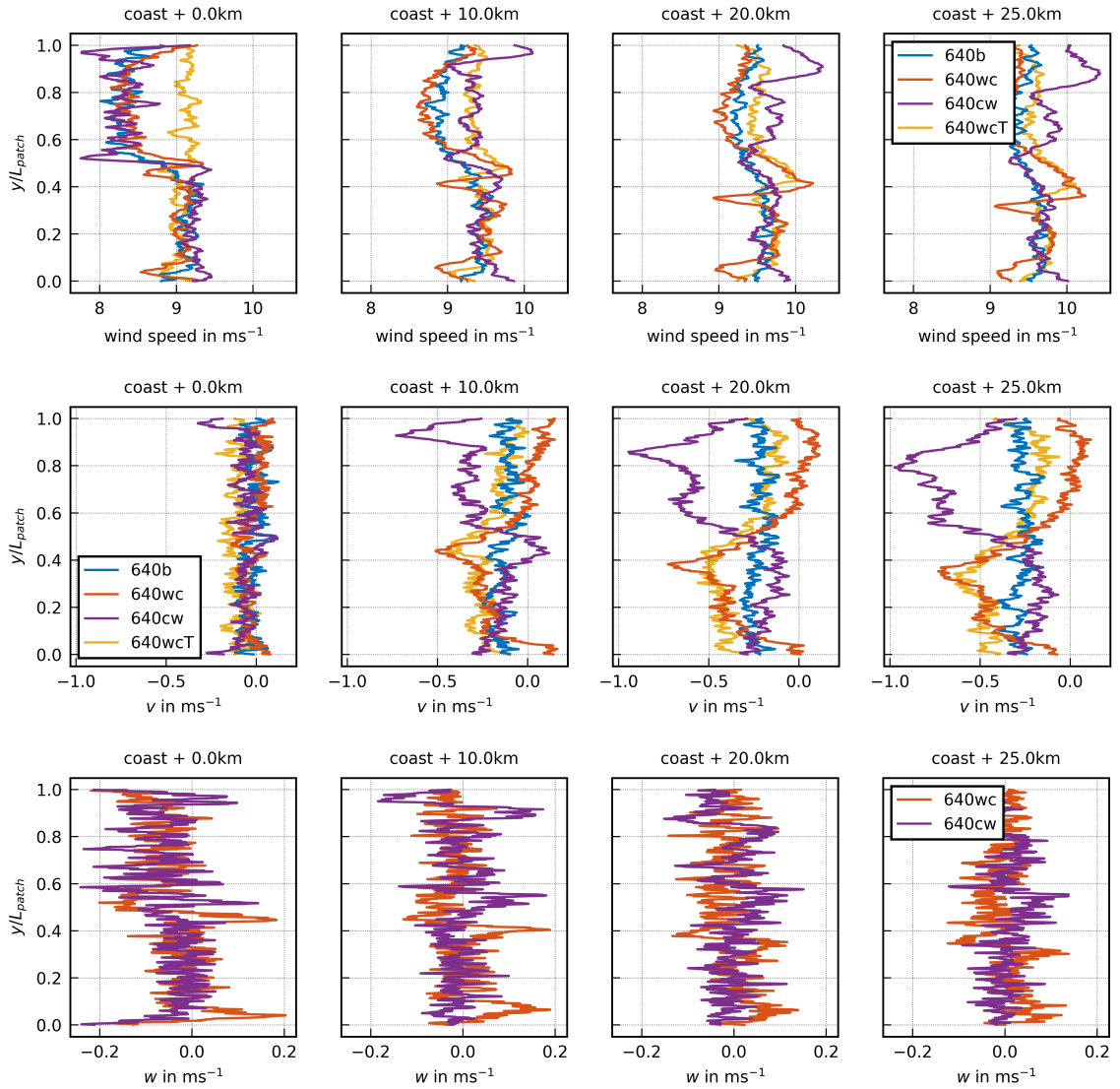


Figure 6.5: 1-hour averaged wind speed and wind speed components v and w at a height of $z = 145$ m, perpendicular to the main flow direction, taken at various positions behind the coastline for the cases 640b, 640wc, 640cw and 640wcT, containing roughness changes and temperature changes. For better visibility the cases 640b and 640wcT are omitted in the plot of the vertical wind speed component w .

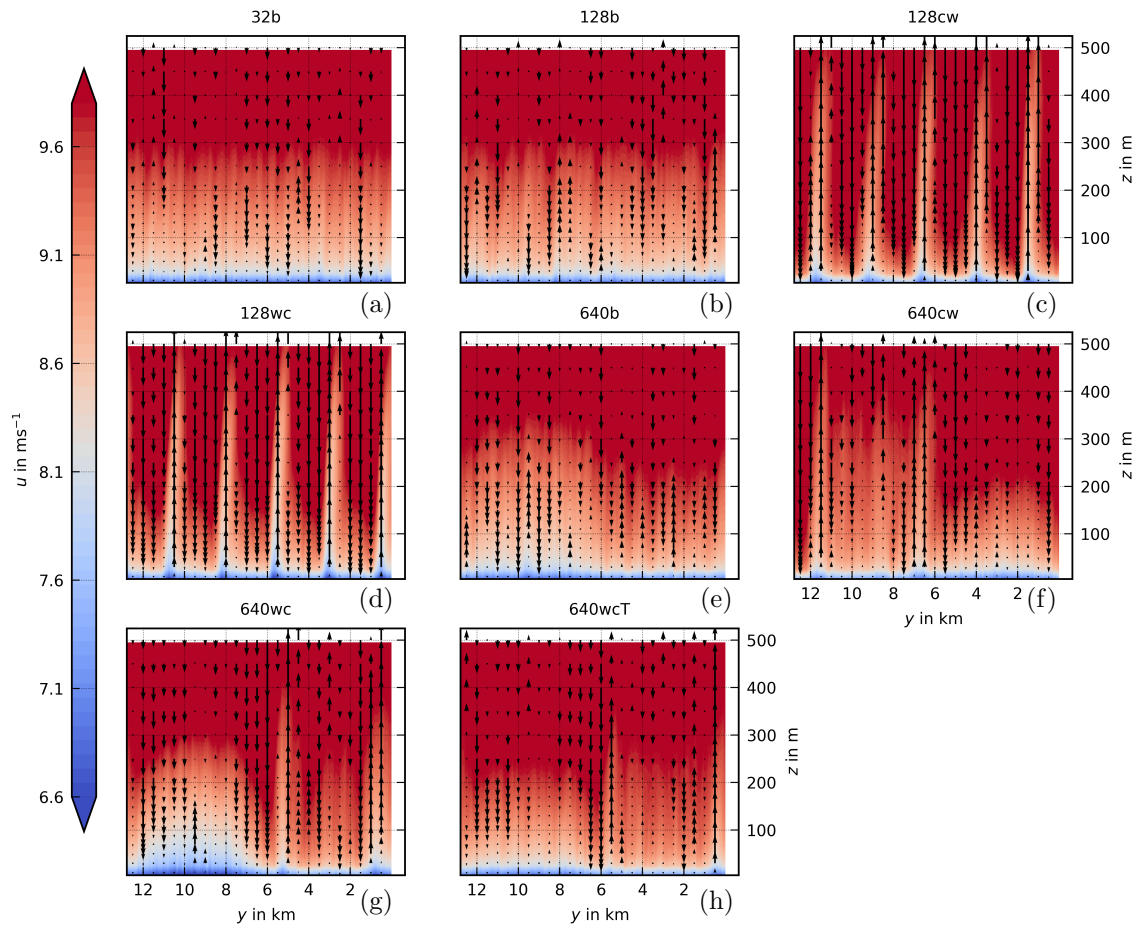


Figure 6.6: Cross-section in the yz -plane, in 10 km distance to the coastline, illustrating the horizontal wind speed component u in color, with vectors representing the vertical component w . Data is averaged over a 1-hour period.

6.2.2 Closer look at 128wc and 640wc

Figure 6.3 shows that the cases with a combination of a warm patch with a short roughness length and a cooler patch with a longer roughness length have the strongest effects in the wider patch size of 6400 m. Consequently, this case (640wc) is examined more closely. Additionally, Fig. 6.6 shows that the 1280 m wide patches result in streaks of low wind speed reaching high altitudes, meriting a detailed examination of the case 128wc.

In Fig. 6.7, a yz -cross section of these cases is presented. The horizontal wind speed component, u , is depicted using color, while the components v and w are represented by streamlines. A vertical component of the circulation can be observed, especially in the case of 128wc, which is limited in the upper area by the boundary layer. The limitation due to the boundary layer height is also recognisable in case 640wc. Here, the circulation is particularly evident in and around the area of reduced wind speed at the edges of the stripe behind the cold patch. The intensity of the vertical movement is highest close to the surface.

In Fig. 6.8 the turbulence intensity (TI) is shown for the same position as Fig. 6.7. The impact of the heterogeneities is also evident in the turbulence, exhibiting a pattern similar to that of wind speed. The increase in TI, akin to the reduction in wind speed, is unevenly distributed across the width of the stripes, with its peak occurring on the left side. This pattern is similar to the wind farm wake development described in Maas [2023]. This results in differences in TI of up to 3.3% at a height of 145 m, see Fig. 17 in the Appendix of this chapter, which shows the TI at 145 m along y direction.

Figure 6.9 shows the development of the flow with increasing distance from the coast. At the coastline it can be seen in Fig. 6.9a for the 640wc case, that the highest reduction of the wind speed occurs and the heterogeneities have an effect in the flow up to an altitude of 330 m. At a distance of 10 km from the coastline, this effect extends to an altitude of 500 m. At 25 km distance, streaks of reduced wind speed remain visible below an altitude of 200 m.

For case 128wc in Fig. 6.9b, the highest wind speed reduction is observed along the coastline, with the reduction decreasing progressively with distance from the coast. In 25 km distance the influence of the patches is still visible as horizontal wind speed gradients in y -direction. As could be observed in Fig. 6.7b the centre of the stripes show a minimal vertical movement, while the edges of the stripes show a vertical transport of the flow. In Fig. 6.9b the edges of the stripes are visible in the vertical component w , but also in the horizontal component u . The position of these areas move closer together with increasing distance from the coast.

Figure 6.10 illustrate the potential temperature as a color gradient and the v component of wind speed at varying distances from the coastline. The plots indicate that the flow moves from areas of lower temperature to higher temperature, adding to the previously described horizontal movement. Furthermore, a difference in potential temperature along the y -axis is still evident even at a distance of 25 km, particularly in the 640wc case (Fig. 6.10b), but also observable in the 128wc case (Fig. 6.10a).

Figure 6.13 shows a xy section of 640wc and illustrates how the stripe at $y=6400$ m moves in a clockwise direction towards the stripe at lower y -values.

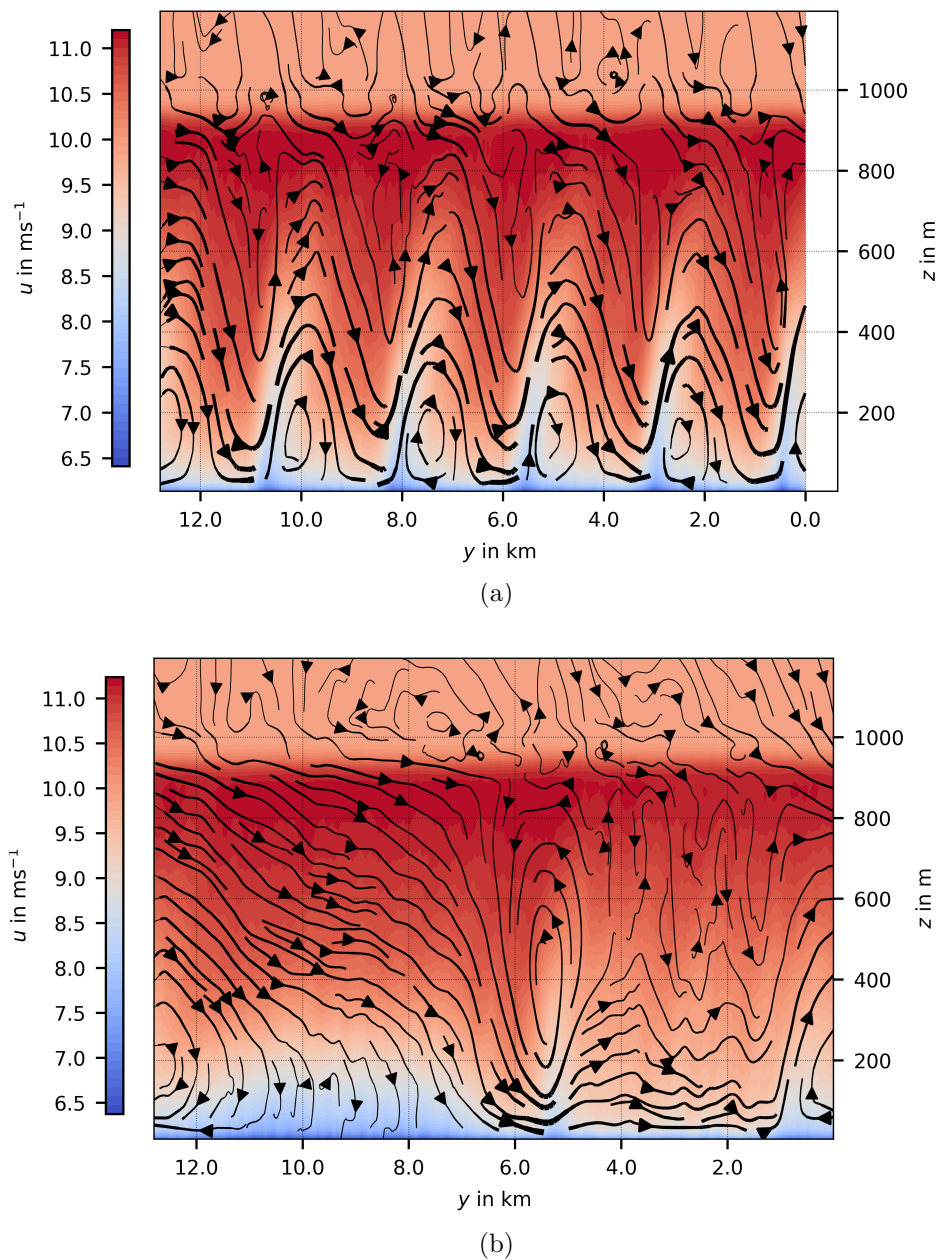
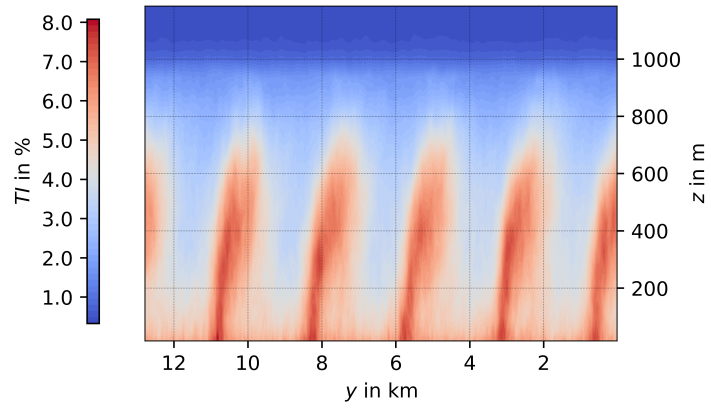
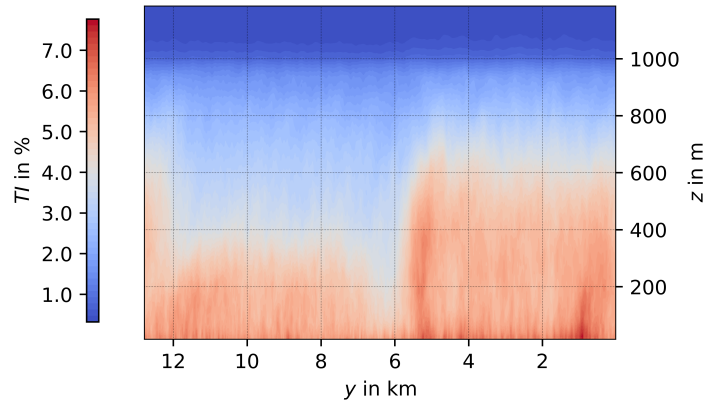


Figure 6.7: Cross-section in the yz -plane, in 10 km distance to the coastline, illustrating the horizontal wind speed component u in color, with streamlines representing the components v and w . Data is averaged over a 1-hour period and the inflow components of v and w are subtracted for each height level. (a) for the case 128wc and (b) for 640wc.



(a)



(b)

Figure 6.8: Cross-section in the yz -plane, in 10 km distance to the coastline, illustrating the turbulence intensity TI. Data is averaged over a 1-hour period. (a) for the case 128wc and (b) for 640wc.

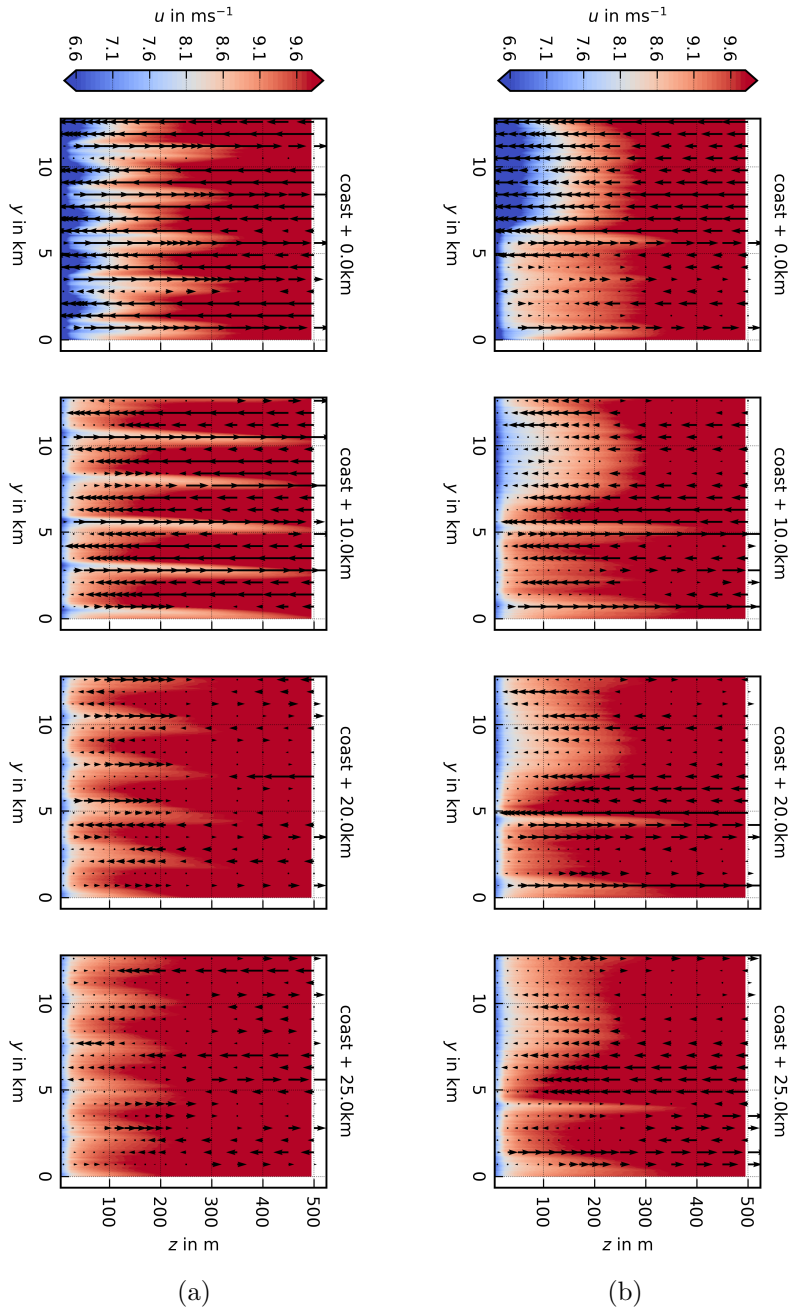


Figure 6.9: Cross-section in the yz -plane in streamwise direction for the cases (a) 128wc and (b) 640wc at subsequent x -positions downstream of the coastline, illustrating the horizontal wind speed component u in color, with vectors representing the vertical component w . Data is averaged over a 1-hour period.

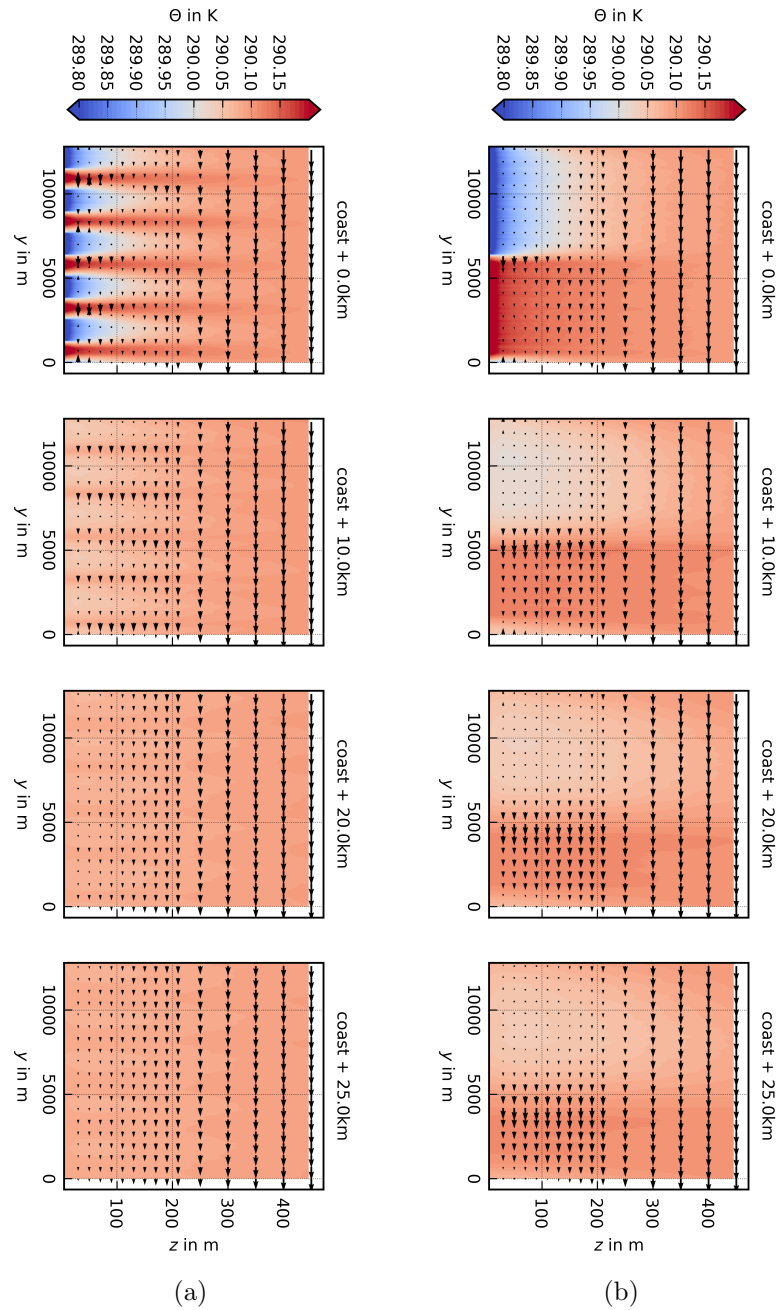


Figure 6.10: Cross-section in the yz -plane in streamwise direction for the cases (a) 128wc and (b) 640wc at subsequent x -positions downstream of the coastline, illustrating the potential temperature θ in color, with vectors representing the horizontal component v . Data is averaged over a 1-hour period and the inflow v component is subtracted for each height level.

6.3 Turbine power output and loads in flows downstream of inhomogeneous surfaces

The simulations conducted to analyze the effects of heterogeneities on downstream wind turbines are detailed below, followed by the presentation and discussion of the results.

6.3.1 Description of the simulations performed

As detailed in Section 6.1, the turbine model has been adjusted to utilize the IEA-15-240-RWT. These adjustments are examined to ensure the power output is within the correct order of magnitude. A laminar simulation with a wind speed of 8 ms^{-1} is conducted using the PALM-FAST framework. For reference, a FAST simulation with a steady wind inflow of 8 ms^{-1} is performed using AeroDyn15. The power output is averaged after the initial turbine spin-up, starting at 200 s. This results in a mean power output of 6584 kW for FAST and 6744 kW for the PALM-FAST framework. This indicates that the PALM-FAST framework overestimates the power output by 2.42% compared to the reference. Therefore, it can be concluded, that the PALM-FAST setup, utilizing AeroDyn14, achieves performance within a realistic order of magnitude for the investigated wind speed range. Since the turbine output in this study is compared within the results of the PALM-FAST framework, this level of accuracy is considered satisfactory.

A greater temperature difference was selected for the cases 128wc and 640wc to examine the influence of the resulting structures on wind turbines. According to Ellison et al. [2017], this surface temperature difference is realistic due to different land uses. Figure 6.11 shows the flow downstream of the heterogeneities with 5 K difference without turbines present. In comparison to Fig. 6.9 the effect of the increased temperature difference is visible. Compared to 640wc, case 640wc5K is more stable along the coastline due to the larger temperature difference, with a more pronounced vertical velocity gradient and the merging of low-speed streaks occurring over a shorter distance to the coastline, resulting in low-speed streaks being present at higher altitudes than in 640wc, even at a distance of 25 km from the coastline. In case 128wc5K, the low wind speed streaks near the coastline are more pronounced than in 128wc due to the stronger temperature difference, and their altitude is higher at the coastline compared to 128wc. However, the altitude decreases more rapidly with distance, so that further from the coastline, the streaks in 128wc reach higher altitudes than in 128wc5K.

This is also evident in the direct comparison of the cases shown in Fig. 6.12. The differences between 640wc and 640wc5K are illustrated in Fig. 6.12b. In the 640wc5K case, patch A1 ($y/L_{\text{patch}} = [0.0, 0.5]$) is 0.5 K warmer than the inflow A0, while patch A2 ($y/L_{\text{patch}} = [0.5, 1.0]$) exhibits a steeper temperature change of 4.5 K in comparison to the inflow. This leads to a highly stable stratification after A2, evident in the minimal change in wind speed with increasing distance from the coast. Clear differences are also recognizable when comparing 128wc and 128wc5K (Fig. 6.12a). The wind speed gradient is more pronounced for 128wc5K at the coast, but decreases faster with increasing distance from the coast than for 128wc.

Figure 6.13 shows an xy -plane cross-section comparing 640wc and 640wc5K. It is evident that, in the case of 640wc5K, the low wind speed streaks converge, whereas no such convergence is observed within the model domain for 640wc. The stronger lateral temperature gradient in the 640wc5K case results in a more pronounced lateral movement of the streak near $y = 0 \text{ km}$, leading to the convergence of the low wind speed stripes.

To test scenarios that differ significantly within the resulting structures for the wind turbines, turbine positions are selected based on wind speed and the vertical component w . A minimum and maximum of the wind speed are chosen, typically corresponding to a significant gradient in the vertical component, as illustrated in Fig. 6.14.

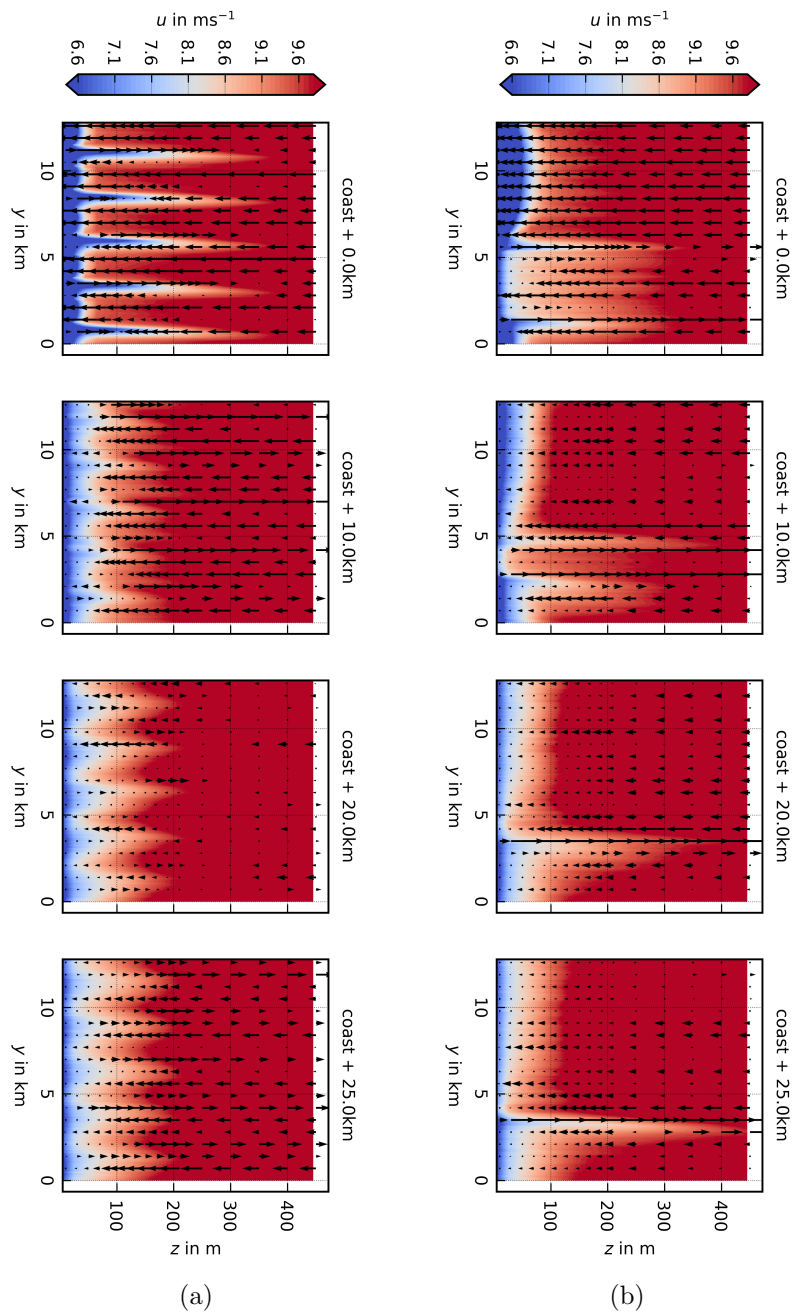


Figure 6.11: Cross-section in the yz -plane for the cases (a) 128wc5K and (b) 640wc5K at subsequent x -positions downstream of the coastline, illustrating the horizontal wind speed component u in color, with vectors representing the vertical component w . Data is averaged over a 1-hour period.

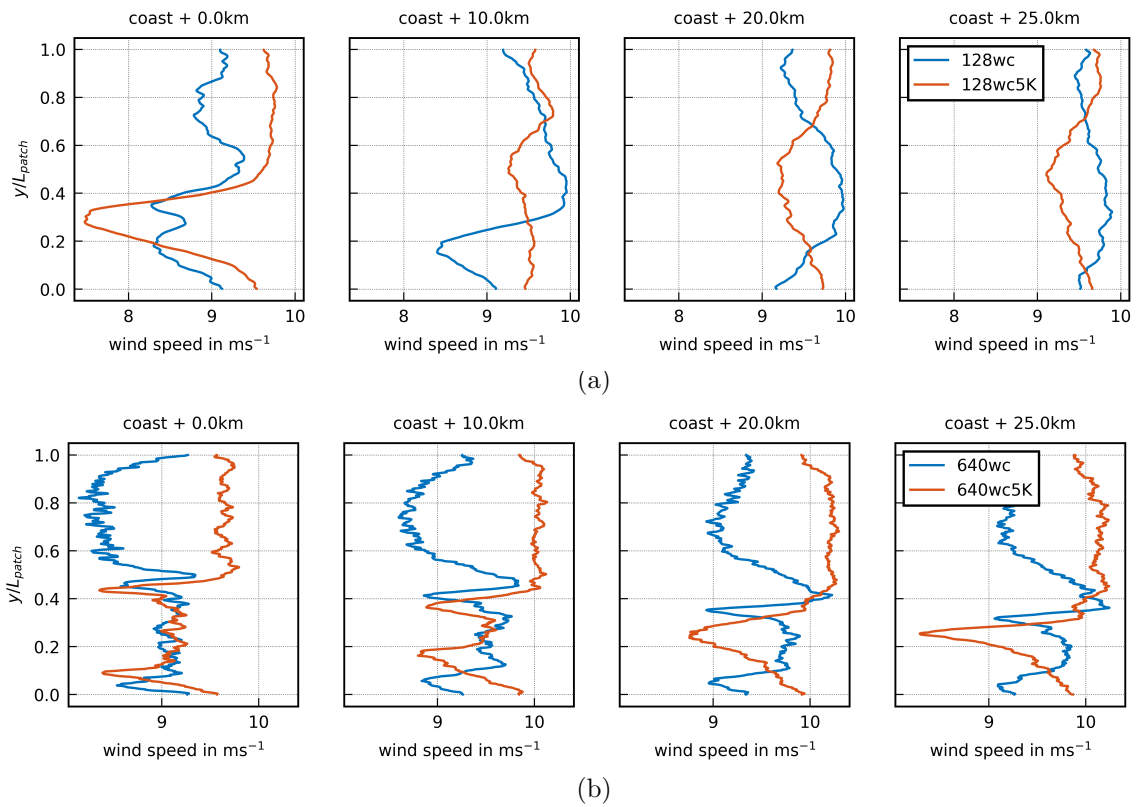


Figure 6.12: Average wind speed at a height of $z = 145$ m, perpendicular to the main flow direction, taken at various positions behind the coastline for the cases (a) 128wc and 128wc5K and (b) 640wc and 640wc5K. The data are averaged over a duration of 1 h.

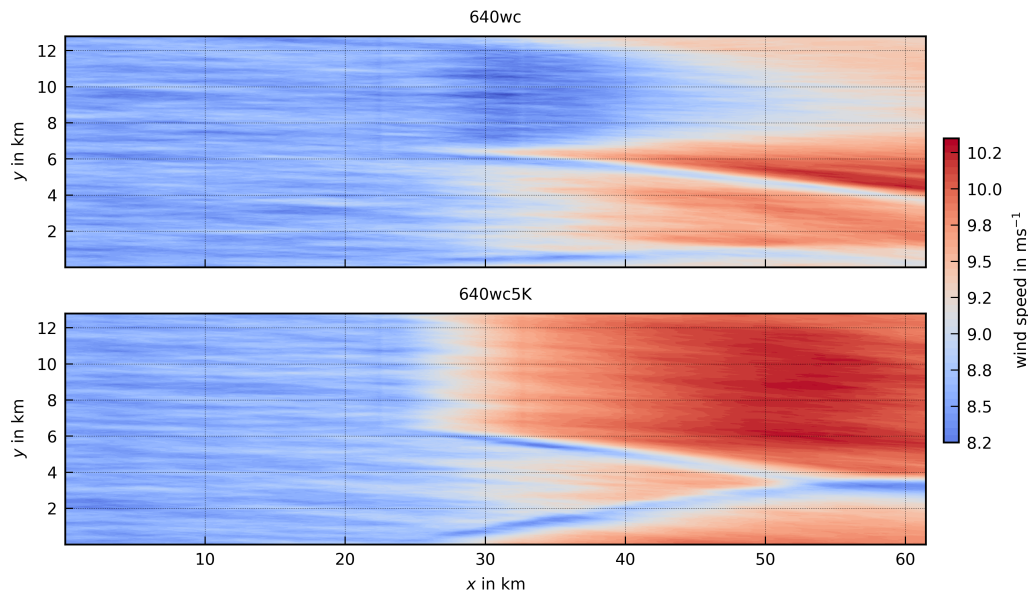


Figure 6.13: Cross-section in the xy -plane for the case 640wc and 640wc5K. Data is averaged over a 1-hour period.

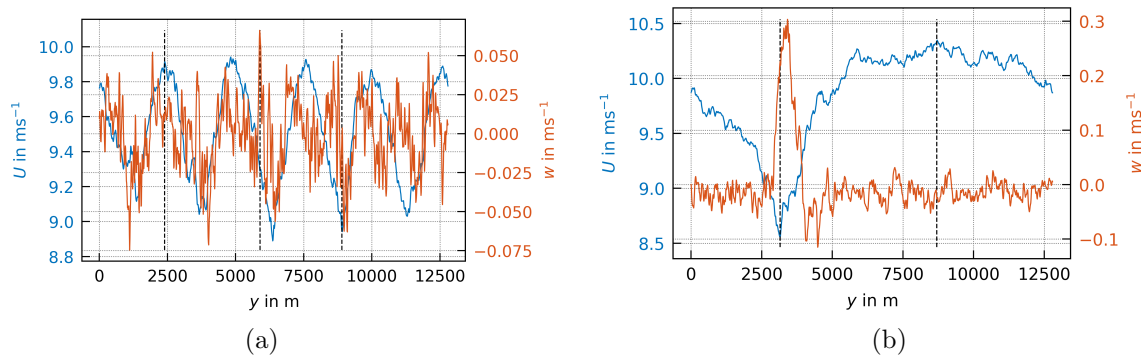


Figure 6.14: Wind speed U and vertical wind speed component w along y at a distance of 20 km downstream of the coastline at 145 m height for the cases (a) 128wc5K and (b) 640wc5K. The dashed vertical lines show the proposed turbine positions.

6.3.2 Results

As anticipated, the turbines produce different power outputs based on wind speed, as illustrated in the time series data (Fig. 6.15) and in Table 6.3, which presents the average power output along with its standard deviation. The standard deviation of the power serves as an indicator of the TI at the turbine position.

128wc5K

In the case of 128wc5K, in addition to a high and a low wind speed, the position of a high vertical wind speed component w was also selected, see 6.14a. The wind speed at the 5900 m position is 9.29 ms^{-1} , at the 8900 m position it is 9.10 ms^{-1} , the difference in power is 37.73 kW, while the difference in the standard deviation shows a difference of 132.33 kW. The higher standard deviation of the power can be seen at the 5900 m position, which has the higher vertical wind speed component in comparison to the position 8900 m.

The 2400 m position exhibits the highest power yield among the three tested positions, while its standard deviation in power is comparable to that of the other two positions, coinciding with the low vertical wind speed component. In Fig. 18 in the Appendix the spectra of the blade bending in-plane and out-of-plane are shown. The width and height of the peaks in the spectra vary, reflecting the conditions at each position. For instance, peak width increases with higher TI. However, the differences are relatively small, making them less apparent in the spectra.

640wc5K

In this case, the two positions primarily differ in wind speed and the resulting power output. Additionally, the standard deviation of power varies significantly between the two positions. The TI is higher at the position with the lower wind speed, which is also reflected in the load measurements. The absolute load values shown in Table 6.3 indicate only a small difference despite the variation in wind speed, this is also demonstrated in the spectra shown in Fig. 19 in the Appendix, where the higher TI results in broader peaks at the 3150 m position.

In order to obtain a more accurate picture of the effects on the loads, the equivalent load ranges Δ_{eq} , corresponding to the non-normalized damage equivalent loads (DEL) were calculated from the load time series. The Palmgren-Miner rule (equation 6.1), as described in Vera-Tudela and Kühn [2017], was used for this purpose.

$$\Delta_{eq} = \left(\sum_{k=1}^n N_k \Delta S_k^m / N_{ref} \right)^{1/m}, \quad (6.1)$$

where n represents the number of distinct loading amplitudes, N denotes the total number of cycles, and ΔS is the loading amplitude. Additionally, a Wöhler exponent of $m = 10$ is assumed for the blades, along with a reference number of cycles $N_{ref} = 10^7$.

The results of the calculation of the equivalent load ranges Δ_{eq} are presented in Table 6.4. For the in-plane load M_x , the values show minimal deviations across the cases. However, larger deviations are observed in the out-of-plane loads M_y . The maximum values in case 128wc5K occur at position 5900 m, which, although not exhibiting the maximum power, corresponds to the highest vertical wind speed component among the three tested positions. A similar result is observed in the 640wc5K

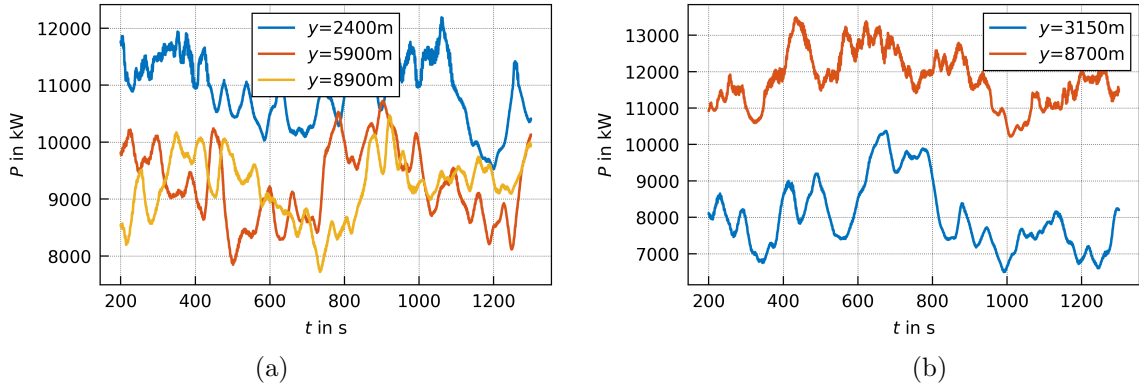


Figure 6.15: Power time series of turbines at y positions (a) $y = 2400\text{ m}$, $y = 5900\text{ m}$ and $y = 8900\text{ m}$ in the case 128wc5K and (b) $y = 3150\text{ m}$ and $y = 8700\text{ m}$ in the case 640wc5K.

case, where the maximum load value in the out-of-plane direction corresponds to the higher vertical wind speed component rather than the case with the higher power.

Table 6.3: Mean \bar{P} and standard deviation σP of the power output, as well as in-plane M_x and out-of-plane M_y moments at the blade root, at two turbine positions. Averaged over 900 s, starting from simulation time 200 s.

	Position	\bar{P} [kW]	σP [kW]	M_x [kN]	M_y [kN]
128					
	2400 m	10882.98	565.75	4608.06	53545.55
	5900 m	9264.78	664.25	4156.22	48800.17
	8900 m	9227.05	531.92	4166.75	48719.47
640					
	3150 m	8022.71	954.93	3771.44	44618.31
	8700 m	11801.12	744.78	4959.36	55456.40

Table 6.4: Equivalent load ranges Δ_{eq} , calculated for the time series of 900 s, starting from simulation time 200 s, for the in-plane M_x and out-of-plane M_y moments at the blade root.

	Position	Δ_{eq} [kNm]	
		M_x	M_y
128			
	2400 m	12423.65	3959.74
	5900 m	12425.76	4182.29
	8900 m	12438.33	4010.63
640			
	3150 m	12198.41	4418.40
	8700 m	12461.28	3859.60

6.4 Discussion

The most pronounced effects of the heterogeneities are observed when there are differences in temperature in addition to differences in roughness length. These conditions can create stripes that extend beyond the modelled area, often exceeding 30 km. The heterogeneities cause a vertical upward movement in the flow, which is constrained by the boundary layer height. This results in a circulation pattern that contains a downward movement.

The heterogeneities influence the resulting downstream flow in different ways. For instance, when looking at a pure roughness difference (see Fig. 6.2), similar gradients in cases 128b and 640b can be observed. This observation suggests that the gradients are not affected by the width of the heterogeneities. Moreover, the fundamental mechanism remains the same regardless of the patch widths tested, provided there is no temperature change.

The scenario is different when additional temperature variations are introduced: The resulting downstream flow varies according to the width of the heterogeneities. In cases 128cw and 640cw, where the heterogeneities' properties mutually amplify, wind speeds at the coast are similar, diverging with increased distance. The most significant downstream wind speed differences, however, are observed in cases 32wc, 128wc, and 640wc. In case 640wc, featuring the broadest heterogeneity of the three cases, the flow seems to adapt to the heterogeneity patches' characteristics when space permits. For case 128wc, this adaptation is partially evident at the coast but diminishes with distance. The adaptation is not apparent in patch width 32wc, which is significantly below the boundary layer height.

Wind speed gradients form at the edges of the heterogeneous patches. When a warmer, smoother patch pairs with a colder, rougher patch, the gradients persist furthest downstream (wc-cases). Conversely, pairing a warmer, rougher patch with a colder, smoother patch (cw-cases) results in the most significant gradients at the coast. However, these gradients diminish over a shorter distance from the coast compared to the wc-cases.

The induced vertical movements in the flow transports the characteristics of the higher-altitude flow to lower levels and also lifts lower wind speeds and turbulence properties from below to higher

altitudes. Consequently, higher wind speeds can descend to lower layers, creating stripes with increased wind speeds. And in order to close the circulation, strips with low wind speeds are created alongside the strips with high wind speeds, which are caused by the upward component of the vertical circulation. Additionally, the wind direction shifts with altitude due to the Ekman spiral effect. As a result, the vertical movements can also alter the wind direction at lower altitudes, imparting a lateral component to the movement of the streaks. This is illustrated in Figures 6.2 to 6.4, where the y -position of the peaks at different distances from the coastline shifts towards lower y -values. This means a movement of the flow in clockwise direction, which coincides with the direction of the geostrophic wind, caused by the Coriolis force. The vertical downward movement thus transports momentum and wind direction of higher layers down to lower layers. In addition, the lateral movement is influenced by the temperature difference, which leads the flow from lower to higher temperatures. This likely accounts for the merging of the stripes of low wind speeds in the 640wc5K case.

Similar behaviour can be found in wind farm wakes, as described in [Lanzilao and Meyers \[2024\]](#). Here, the influence of the boundary layer height and its capping inversion on the wakes of a wind farm is investigated. The case of the boundary layer height of 1000 m in [Lanzilao and Meyers \[2024\]](#) is comparable to the configuration used in this work. Among others the results in [Lanzilao and Meyers \[2024\]](#) show the clockwise movement of the wakes for the cases of higher boundary layer height, such as 1000 m. It was observed that vertical mixing transports faster-moving air from higher layers into the lower layers. This influx of higher momentum enhances the Coriolis force in these lower layers. Additionally, the wind veer is transported deeper, resulting in a clockwise wind direction being carried into the lower layers. These mechanisms can be seen in this study in a similar way.

The test cases with wind turbines show that the turbine is influenced by its position and the local conditions. The cases demonstrate that power production varies with the turbine's position due to differing wind speeds. Furthermore, there are differences in the vertical component of the wind speed and the TI, which do not coincide with the magnitude of the wind speed. This means that a high wind speed does not necessarily mean a high TI and vertical wind speed. These variations in TI and vertical wind speed contribute to differing loads, and can result in relatively high loads even at low wind speeds and low power outputs.

6.5 Conclusions

Various simulations with an idealized geometrical setup were conducted to investigate the influence of surface heterogeneities on the downstream flow. The simulations systematically varied the width of the heterogeneities, as well as the combination and sequence of roughness and temperature differences among the patches, reflecting such combinations as flat grassland next to urban use. Near the coast, the effects of heterogeneities were evident in all cases. Depending on the characteristics of these heterogeneities, influences could still be detected at varying distances. The heterogeneities produced wind speed gradients parallel to the coastline, manifesting as stripes in the wind speed, along with variations in TI and the vertical wind speed component w . The combination of roughness and temperature differences resulted in the most pronounced stripes in the wind speed field, observable at distances exceeding 25 km.

The heterogeneities induce a circulation that persists downstream. This circulation facilitates the downward transport of properties from higher air layers and the upward transport from lower

layers. Consequently, higher wind speeds and a clockwise shift in wind direction from elevated altitudes are transported downwards, resulting in the differences of wind speed and TI and a lateral displacement of wind speed peaks. The strength of the circulation and thus the persistence of stripes of increased or decreased wind speed depends on the heterogeneity upstream. A warmer heterogeneity patch compared to its surroundings, results in an unstable stratification downstream, while a cooler heterogeneity patch leads to a stable stratification downstream. However, sole temperature changes affect flow dynamics only over small areas, with lateral gradients not visible over large distances. If, on the other hand, an additional change in roughness is added, a circulation develops at the boundaries of the patches, due to the differences caused by the heterogeneity patches. These lead to the described mixing of flow properties over height and become visible as stripes in streamwise direction. This study found that the combination of a temperature-reduced patch with high roughness length and a patch with increased temperature and low roughness length exhibited the highest persistence of lateral gradients, being still visible in the elongated model domain after 40 km.

For wind turbines, positioned downstream of heterogeneities, this means that different energy yields are achieved depending on the location. Depending on the width of the heterogeneities, the characteristics of the wind fields can vary greatly even within a few 100 m. These properties with different TI and wind speeds also have an effect on the loads of the wind turbines. Consequently, these effects should be investigated in more detail and be considered in forecasts, yield predictions, and site analyzes, as they influence both the power output and the lifespan of turbines.

The simulations rely on numerous assumptions and there are many other possible variations of the parameters roughness, temperature, heterogeneity size, model domain configuration and initial wind speed that can be done in future studies. Additionally, parameters such as stability and the dependence of roughness on friction velocity over the ocean, as described by [Charnock \[1955\]](#), can also be incorporated, to investigate the effects on the downstream flow. A valuable enhancement to this study would be to validate the results with measurement data. To achieve this, a suitable location with diverse land uses along the coast should be selected. For instance, as demonstrated by [Dörenkämper et al. \[2015\]](#), coastal heterogeneity is expected to impact flow dynamics on the German coast near Rostock. This effect arises primarily from the local combination of urban land use with adjacent low roughness areas, such as farmland and grassland.

Appendix

A.1 Stripes downstream of inhomogeneous surfaces - additional results

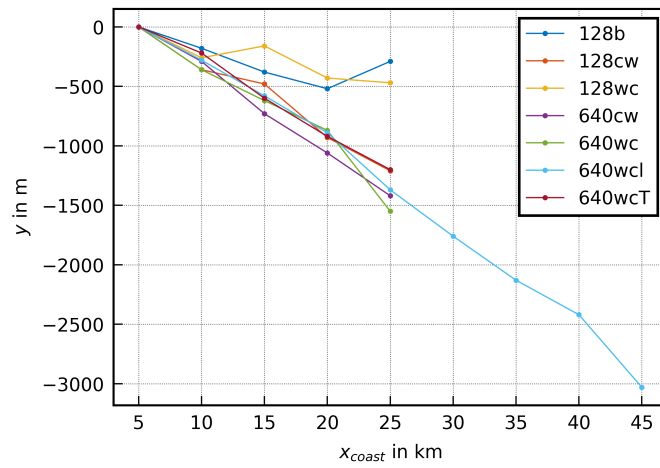


Figure 16: Positions of the maxima in wind speed at 145 m height along y -direction and their lateral movement with distance to the coastline.

A.1.1 Statistics of wind speed along y with distance to coastline

Table 5: Mean wind speed at 145 m height for distances 0km, 5km, and 10km, averaged in y -direction at different distances to the coastline. Additionally, the positive and negative deviation from the mean value are shown in %. The maximum values per distance to coastline are marked in bold.

	0km			5km			10km		
	\bar{U} [ms ⁻¹]	$\Delta-$ [%]	$\Delta+$ [%]	\bar{U} [ms ⁻¹]	$\Delta-$ [%]	$\Delta+$ [%]	\bar{U} [ms ⁻¹]	$\Delta-$ [%]	$\Delta+$ [%]
128b	8.69	6.33	4.67	8.88	4.53	3.50	9.15	2.50	2.76
128cw	8.82	13.86	8.84	9.29	11.06	7.14	9.65	9.90	7.09
128wc	8.84	8.35	6.20	9.07	15.47	7.38	9.38	10.94	6.19
32b	8.75	8.58	6.73	8.89	4.40	4.28	9.12	1.86	1.55
640b	8.72	8.12	7.28	8.91	5.80	6.23	9.18	5.12	4.64
640cw	8.78	11.70	7.80	9.14	8.53	7.87	9.42	4.99	7.22
640wc	8.75	6.48	6.39	8.92	6.73	7.48	9.17	6.25	7.22
640wcT	8.76	6.99	6.72	9.24	4.92	3.32	9.41	4.45	3.91

	15km			20km			25km		
	\bar{U} [ms ⁻¹]	$\Delta-$ [%]	$\Delta+$ [%]	\bar{U} [ms ⁻¹]	$\Delta-$ [%]	$\Delta+$ [%]	\bar{U} [ms ⁻¹]	$\Delta-$ [%]	$\Delta+$ [%]
128b	9.31	2.24	2.34	9.43	2.87	2.48	9.50	2.14	1.91
128cw	9.85	8.46	6.69	9.93	6.35	5.71	9.95	4.50	4.32
128wc	9.51	7.97	5.76	9.58	4.92	4.83	9.62	3.21	2.99
32b	9.24	1.47	1.61	9.33	1.73	1.44	9.39	1.65	1.32
640b	9.33	5.14	4.17	9.44	3.12	3.62	9.51	3.70	2.74
640cw	9.59	4.05	7.35	9.69	4.55	6.80	9.76	5.28	6.85
640wc	9.33	5.85	7.97	9.43	5.31	8.43	9.50	4.63	7.82
640wcT	9.52	5.56	3.97	9.60	3.73	4.85	9.65	4.21	4.80

A.2 Closer look at 128wc and 640wc - additional results

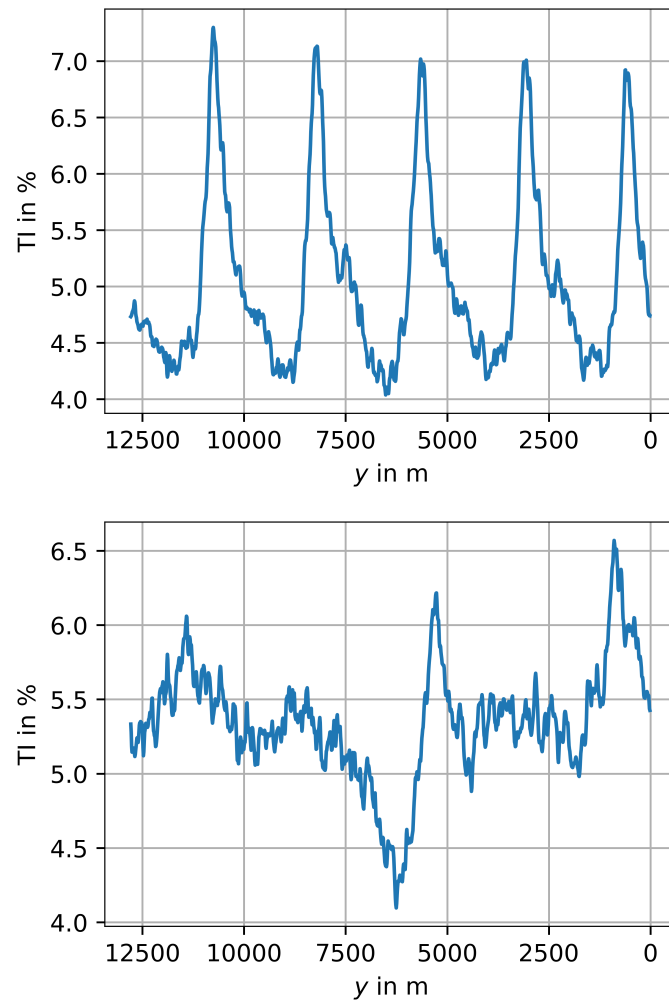


Figure 17: TI along y at hubheight 145 m, in 10 km distance to the coastline. Data is averaged over a 1-hour period. (a) for the case 128wc and (b) for 640wc.

A.3 Turbine loads spectra

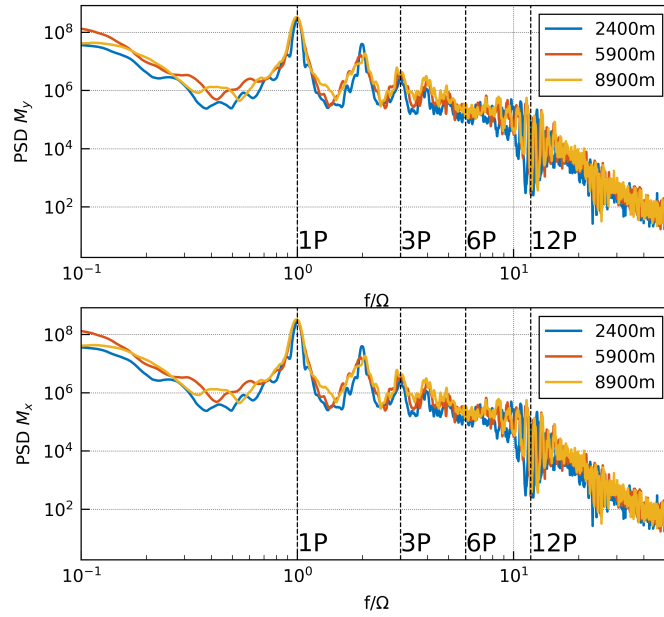


Figure 18: Spectra of the blade root in-plane M_x and out-of-plane M_y bending moments in the case 128wc5K.

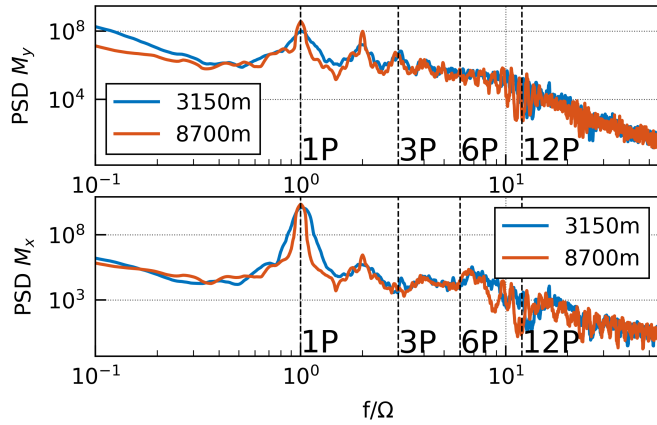


Figure 19: Spectra of the blade root in-plane M_x and out-of-plane M_y bending moments in the case 640wc5K.

Chapter 7

Conclusions and Outlook

7.1 Conclusions

One of the major challenges in wind energy research involves accurately resolving the intricate dynamics of wind turbine systems, particularly in the context of wind farms, across a wide range of length scales, from tens of kilometers down to centimeters. This necessitates a comprehensive understanding of the aerodynamic forces acting on wind turbines, which are essential for predicting their performance and optimizing energy capture in varying atmospheric conditions.

To address these challenges, the advancements and testing of the PALM-FAST model chain presented in this thesis demonstrate significant progress in bridging the gap between large-scale atmospheric simulations and detailed wind turbine dynamics. By integrating the aeroelastic code FAST with the large-eddy simulation tool PALM, this work provides a robust framework for analyzing turbine performance and loads under realistic atmospheric conditions. The successful validation with the generic NREL 5 MW turbine and the eno114 3.5 MW turbine underscores the accuracy and applicability of the developed coupling, while the introduced enhancements—such as wind speed corrections and computational efficiency improvements—highlight its potential for addressing complex and heterogeneous flow scenarios.

The investigation of coastal conditions in this thesis further emphasizes the critical role of surface heterogeneities, such as roughness and temperature variations, in shaping atmospheric flow and their downstream impact on wind turbines. Through large-eddy simulations of idealized coastal transitions, the results reveal how lateral gradients and induced circulations influence turbine performance and loads, providing valuable insights for optimizing offshore wind farm design and operation.

In the following, the research questions outlined in Chapter 1.4 will be revisited and discussed in more detail in light of the findings presented in this thesis.

1. Can the coupling between the LES tool PALM and the aeroelastic model FAST be validated against measurement data for mapping turbine behavior under varying atmospheric conditions?
 - The coupling of the LES tool PALM with the aeroelastic model FAST is feasible for simulating wind turbine behavior under various atmospheric conditions for a single turbine. It combines PALM's high-resolution atmospheric flow simulation with FAST's detailed turbine response modeling, offering a computationally efficient and accurate framework.

- The coupling was validated in two steps: (1) Using the NREL 5 MW turbine, it demonstrated excellent agreement in power output and achieved up to 89% computational time savings compared to the ALM-based coupling. (2) Validation against measurement data from the eno114 3.5 MW turbine showed close alignment in power output and load predictions, with good agreement in turbulence effects and stability impacts.
 - The approach avoids overestimating power by sampling wind speed in front of the turbine rather than at the rotor area. It also captures load variations due to atmospheric stability and provides reliable predictions of overall load spectra, despite some deviations caused by modeling parameters like tower eigenfrequency and rotor imbalance.
 - The method has some limitations, including reliance on idealized conditions (e.g., homogeneous roughness, no topography) and assumptions like frozen wind fields, which may affect results in scenarios with varying wind directions or wake interactions.
 - The reduced computational time and accuracy of the PALM-FAST coupling make it highly suitable for load analyses of single turbines in wind farms. It also has broader applications, such as footprint analyses, studying environmental impacts on turbine performance, and investigating phenomena like low-level jets or wake interactions.
2. How does the PALM-FAST coupling perform in a complex scenario involving one turbine operating in the wake of another?
- The PALM-FAST coupling, extended with the ASM-SL NWC framework, has been verified in scenarios involving one turbine in the wake of another. This includes varying distances between turbines, where the coupling demonstrated strong performance in representing both power output and turbine loads.
 - The ASM-SL NWC has been validated against measurement data, showing reliable and consistent results for turbine performance and loads, even under turbulent flow conditions.
3. How do downstream structures from heterogeneities affect wind turbine performance within the flow?
- Yes, structures downstream of heterogeneities affect wind turbine performance by altering wind speed, turbulence intensity and therefore, the power output and turbine loads.
 - These effects vary with the position in the flow and depend on heterogeneity characteristics like roughness and temperature differences.
 - Such variations in wind speed and turbulence intensity affect the power output and structural loads on wind turbines, leading to performance variability and potential impacts on turbine lifespan.
4. Which parameters influence the strength of downstream flow patterns and lateral gradients due to surface heterogeneities in land-sea transitions and what mechanisms and impacts are observed?
- The strength of downstream flow patterns and lateral gradients is influenced by surface heterogeneity characteristics, such as the roughness contrast between patches, temperature

differences across patches, the width of the heterogeneities, and their specific combination and sequence (e.g., high roughness with low temperature vs. low roughness with high temperature). Initial wind speed, heterogeneity size, and boundary layer height also play significant roles in shaping these patterns.

- Surface heterogeneities create circulation patterns at the boundaries of patches due to differences in roughness and temperature. These circulations facilitate vertical mixing, bringing higher wind speeds from elevated altitudes downward and transporting properties from lower layers upward. Roughness and temperature variations act together to amplify wind speed gradients and TI, resulting in persistent stripes in the flow. Warmer patches destabilize the flow downstream (unstable stratification), while cooler patches stabilize it (stable stratification).
- These flow patterns and gradients extend far downstream, with combined roughness and temperature differences producing the most pronounced and long-lasting effects, visible even 40 km from the coast line.

7.2 Outlook

During the work on this thesis, interest in coupling LES with an aeroelastic tool has grown significantly. While the coupling introduced in Chapter 4 was among the first of its kind, several additional approaches have emerged since then, such as those by [Mohammadi et al. \[2024b\]](#). The strength of these couplings lies in their ability to combine results, offering insights into both atmospheric flow dynamics and detailed turbine behavior. Building on the findings of this work, extending the modeling chain to include additional aspects appears to be a promising idea. For example, couplings between mesoscale models like WRF and LES already exist, enabling the simulation of real-world flow and weather events. These couplings are often focused on urban simulations [[Wyszogrodzki et al., 2012](#), [Lin et al., 2021](#), [Vogel et al., 2022](#)], which operate at smaller spatial scales than those typically relevant for wind energy.

In the context of wind energy, extending these approaches to coarser resolutions with larger grid spacing is necessary, which introduces the challenge of accurately representing turbines in low-resolution grids. A potential solution involves using nesting approaches, where the grid is refined around the turbine while maintaining coarser resolution in the surrounding flow. Another approach recently published is the Actuator Farm model (AFM), which uses a single actuator point at the center of the rotor and requires only two to three grid cells across the rotor diameter, offering a simplified yet computationally efficient way to model the effects of wind turbines and wind farms in mesoscale models [[Stipa et al., 2024](#)].

Combining these suggested couplings into a flexible modeling chain, dynamically integrating tools like WRF, PALM and FAST, would represent a comprehensive framework for addressing a wide range of research and practical needs in wind energy applications.

Bibliography

- U. Arakawa and V.R. Lamb. Computational design of the basic dynamical processes of the UCLA general circulation model. in: General Circulation Models of the Atmosphere. *Methods in Computational Physics*, 17:173–265, 1977.
- R. Avissar and T. Schmidt. An Evaluation of the Scale at which Ground-Surface Heat Flux Patchiness Affects the Convective Boundary Layer Using Large-Eddy Simulations, 1997.
- M. Baldauf. Stability analysis for linear discretisations of the advection equation with Runge-Kutta time integration. *Journal of Computational Physics*, 227:6638–6659, 2008.
- R. J. Beare et al. An Intercomparison of Large-Eddy Simulations of the stable Boundary Layer. *Boundary-Layer Meteorology*, 118:247–272, 2006.
- M. Bock, A. Fuchs, J. Friedrich, and J. Peinke. The use of les to analyse higher-order moments of two-point statistics. *Journal of Physics: Conference Series*, 2767(9):092080, jun 2024. doi: 10.1088/1742-6596/2767/9/092080. URL <https://dx.doi.org/10.1088/1742-6596/2767/9/092080>.
- M. Bromm, L. Vollmer, and M. Kühn. Numerical investigation of wind turbine wake development in directionally sheared inflow. *Wind Energy*, 20(3):381–395, 2017.
- M. L. Buhl Jr. A New Empirical Relationship between Thrust Coefficient and Induction Factor for the Turbulent Windmill State. Technical Report NREL/TP-500-36834, National Renewable Energy Laboratory, 2004.
- T. Burton, D. Sharpe, N. Jenkins, and E. Bossanyi. *Wind Energy Handbook*. Wiley & Sons, 2001.
- M. Calaf, C. Meneveau, and J. Meyers. Large eddy simulation study of fully developed wind-turbine array boundary layers. *Physics of Fluids*, 22(1), 2010. ISSN 1070-6631. doi: 10.1063/1.3291077.
- H. Charnock. Wind stress on a water surface. *Quarterly Journal of the Royal Meteorological Society*, 81(350):639–640, 1955. ISSN 0035-9009. doi: 10.1002/qj.49708135027.
- M. Churchfield, S. Lee, J. Michalakes, and P. J. Moriarty. A numerical study of the effects of atmospheric and wake turbulence on wind turbine dynamics. *Journal of Turbulence*, 13(14):1–32, 2012.
- M. Churchfield, S. Schreck, L. Martínez-Tossas, C. Meneveau, and P. R. Spalart. An Advanced Actuator Line Method for Wind Energy Applications and Beyond. In *Proceedings of the 35th Wind Energy Symposium*, San Diego, CA, January 2017. American Institute of Aeronautics and Astronautics.

- K.O. Dag. *Combined pseudo-spectral/actuator line model for wind turbine applications*. PhD thesis, DTU Wind Energy, 2017.
- J. W. Deardorff. Stratocumulus-capped mixed layers derived from a three-dimensional model. *Boundary-Layer Meteorology*, 18:495–527, 1980.
- DNV GL. Wind Turbine Design Software Bladed, 2020. URL <https://www.dnvgl.com/services/wind-turbine-design-software-bladed-3775>.
- S. Domino. *Sierra Low Mach Module: Nalu Theory Manual 1.0*, sand2015-3107w edition, 2015. Sandia National Laboratories Unclassified Unlimited Release (UUR).
- M. Dörenkämper, M. Optis, A. Monahan, and G. Steinfeld. On the Offshore Advection of Boundary-Layer Structures and the Influence on Offshore Wind Conditions. *Boundary-Layer Meteorology*, 155(3):459–482, 2015. ISSN 00068314. doi: 10.1007/s10546-015-0008-x.
- P. Doubrawa, M. J. Churchfield, M. Godvik, and S. Srinivas. Load response of a floating wind turbine to turbulent atmospheric flow. *Applied Energy*, 242:1588–1599, 2019.
- P. Doubrawa et al. Multimodel validation of single wakes in neutral and stratified atmospheric conditions. *Wind Energy*, 23:2027–2055, 2020. doi: <https://doi.org/10.1002/we.2543>.
- P. Drobinski, P. Carlotti, J.-L. Redelsperger, R.M. Banta, V. Masson, and R.K. Newsom. Numerical and Experimental Investigation of the Neutral Atmospheric Surface Layer. *American Meteorological Society*, 64:137–156, 2007.
- M. Dörenkämper, J. Tambke, G. Steinfeld, D. Heinemann, and M. Kühn. Atmospheric Impacts on Power Curves of Multi-Megawatt Offshore Wind Turbines. *Journal of Physics: Conference Series*, 555, 2014.
- D. Ellison, C. E. Morris, B. Locatelli, D. Sheil, J. Cohen, D. Murdiyarso, V. Gutierrez, M. van Noordwijk, I. F. Creed, J. Pokorný, D. Gaveau, D. V. Spracklen, A. B. Tobella, U. Ilstedt, A. J. Teuling, S. G. Gebrehiwot, D. C. Sands, B. Muys, B. Verbist, E. Springgay, Y. Sugandi, and C. A. Sullivan. Trees, forests and water: Cool insights for a hot world. *Global Environmental Change*, 43:51–61, 2017. ISSN 09593780. doi: 10.1016/j.gloenvcha.2017.01.002.
- eno energy. eno114 3.5, 2019. URL https://www.eno-energy.com/fileadmin/downloads/datenblatt/ENO_114_ENG_Datenblatt_AS.pdf.
- E. Gaertner, J. Rinker, L. Sethuraman, F. Zahle, B. Anderson, G. Barter, N. Abbas, F. Meng, P. Bortolotti, W. Skrzypinski, G. Scott, R. Feil, H. Bredmose, K. Dykes, M. Shields, C. Allen, and A. Viselli. Definition of the IEA 15-Megawatt Offshore Reference Wind Turbine, 2020. URL <https://www.nrel.gov/docs/fy20osti/75698.pdf>.
- H. Glauert. The Analysis of Experimental Results in the Windmill Brake and Vortex Ring States of an AircREW. Technical Report R&M No. 1026, Aeronautical Research Committee, London, 1926a.
- H. Glauert. A General Theory of the Autogyro. Technical Report R&M No. 1111, Aeronautical Research Committee, London, 1926b.

BIBLIOGRAPHY

- H. Glauert. Airplane Propellers. In W. F. Durand, editor, *Aerodynamic Theory*, number Div. L, Chapter XI. Springer Verlag, Berlin, 1935.
- F.H. Harlow and J.E. Welch. Numerical calculation of time-dependent viscous incompressible flow of fluid with free surface. *The Physics of Fluids*, 8:2182–2189, 1965.
- C.R. Harman. PROPX: Definitions, Derivations, and Data Flow, 1994.
- E. L. Hodgson, C. Grinderslev, A. R. Meyer Forsting, N. Troldborg, N. N. Sørensen, J. N. Sørensen, and S. J. Andersen. Validation of aeroelastic actuator line for wind turbine modelling in complex flows. *Frontiers in Energy Research*, 10, 5 2022. ISSN 2296598X. doi: 10.3389/fenrg.2022.864645.
- M. C. Holtslag, W. A. A. M. Bierbooms, and G. J. W. van Bussel. Wind turbine fatigue loads as a function of atmospheric conditions offshore. *Wind Energy*, 19:1917–1932, 2016.
- IEC. Wind turbines – Part 1: Design requirements, IEC/61400-1, 2005.
- P. K. Jha, M. J. Churchfield, P. J. Moriarty, and S. Schmitz. Guidelines for Volume Force Distributions Within Actuator Line Modeling of Wind Turbines on Large-Eddy Simulation-Type Grids. *Journal of Solar Energy Engineering*, 136(3), 01 2014. ISSN ISSN 0199-6231. doi: 10.1115/1.4026252. URL <https://www.osti.gov/biblio/1122303>.
- A. Jimenez, A. Crespo, E. Migoya, and J. Garcia. Large-eddy simulation of spectral coherence in a wind turbine wake. *Environmental Research Letters*, 3(1):015004, 2008. doi: 10.1088/1748-9326/3/1/015004.
- B. J. Jonkman. TurbSim User’s Guide: Version 1.50. Technical Report NREL/TP-500-46198, National Renewable Energy Laboratory, 2009a.
- J. Jonkman, S. Butterfield, W. Musial, and G. Scott. Definition of a 5-MW Reference Wind Turbine for Offshore System Development. Technical Report NREL/TP-500-38060, National Renewable Energy Laboratory, 2009b.
- J. M. Jonkman and M. L. Buhl Jr. FAST User’s Guide. Technical Report NREL/EL-500-38230, National Renewable Energy Laboratory, 2005.
- J.M. Jonkman. The new modularization framework for the fast wind turbine cae tool. In *Proceedings of the 51st AIAA Aerospace Sciences Meeting including the New Horizons Forum and Aerospace Exposition*, January 2013.
- J. C. Kaimal, J. C. Wyngaard, Y. Izumi, and O. R. Coté. Spectral characteristics of surface-layer turbulence. *Quarterly Journal of the Royal Meteorological Society*, 98(417):563–589, 1972.
- N. N. Kethavath and N. S. Ghaisas. Effect of an abrupt rough-to-smooth surface roughness transition on wind farm wakes: An LES and analytical modeling study. *Journal of Renewable and Sustainable Energy*, 16(3), 2024. doi: 10.1063/5.0202733.
- B. Kosović and J. A. Curry. A Large Eddy Simulation Study of a Quasi-Steady, Stably Stratified Atmospheric Boundary Layer. *Journal of the Atmospheric Sciences*, 57:1052–1068, 1998.

- S. Krüger, G. Steinfeld, M. Kraft, and L.J. Lukassen. Validation of a coupled atmospheric-aeroelastic model system for wind turbine power and load calculations. *Wind Energ. Sci.*, 7:323–344, 2022. doi: <https://doi.org/10.5194/wes-7-323-2022>.
- H. Lamb. *Hydrodynamics*. Cambridge University Press, 1932.
- L. Lanzilao and J. Meyers. Wind-farm wake recovery mechanisms in conventionally neutral boundary layers, 2024. URL <http://arxiv.org/pdf/2407.17198v1>.
- S. Lee, M. Churchfield, P. Moriarty, J. Jonkman, and J. Michalakes. Atmospheric and Wake Turbulence Impacts on Wind Turbine Fatigue Loading - Preprint. In *Proceedings of the 50th AIAA Aerospace Sciences Meeting including the New Horizons Forum and Aerospace Exposition*, number NREL/CP-5000-53567. National Renewable Energy Laboratory, 2012.
- J.G. Leishman. Principles of Helicopter Aerodynamics. *Cambridge University Press*, pages 78–127, 2000.
- J.G. Leishman and T.S. Beddoes. A Semi-Empirical Model for Dynamic Stall. *Journal of the American Helicopter Society*, 34(3):3–17, 1989.
- M. O. Letzel and S. Raasch. Large Eddy Simulation of Thermally Induced Oscillations in the Convective Boundary Layer, 2003.
- D. Lin, B. Khan, M. Katurji, L. Bird, R. Faria, and L. E. Revell. WRF4PALM v1.0: a mesoscale dynamical driver for the microscale PALM model system 6.0. *Geoscientific Model Development*, 14(5):2503–2524, 2021. doi: 10.5194/gmd-14-2503-2021. URL <https://gmd.copernicus.org/articles/14/2503/2021/>.
- H. Lübcke, S. Schmidt, T. Rung, and F. Thiele. Comparison of LES and RANS in bluff-body flows. *Journal of Wind Engineering and Industrial Aerodynamics*, 89:1471–1485, 2001.
- O. Maas. Large-eddy simulation of a 15 GW wind farm: Flow effects, energy budgets and comparison with wake models. *Frontiers in Mechanical Engineering*, 9, 2023. doi: 10.3389/fmech.2023.1108180.
- J. Mann. Wind Field Simulation. *Probabilistic Engineering Mechanics*, 13(4):269–282, 1998.
- B. Maronga and S. Raasch. Large-Eddy Simulations of Surface Heterogeneity Effects on the Convective Boundary Layer During the LITFASS-2003 Experiment. *Boundary-Layer Meteorology*, 146(1): 17–44, 2013. ISSN 00068314. doi: 10.1007/s10546-012-9748-z.
- B. Maronga, S. Banzhaf, C. Burmeister, T. Esch, R. Forkel, D. Fröhlich, V. Fuka, K. F. Gehrke, J. Geletić, S. Giersch, T. Gronemeier, G. Groß, W. Heldens, A. Hellsten, F. Hoffmann, A. Inagaki, E. Kadasch, F. Kanani-Sühring, K. Ketelsen, B. A. Khan, C. Knigge, H. Knoop, P. Krč, M. Kurppa, H. Maamari, A. Matzarakis, M. Mauder, M. Pallasch, D. Pavlik, J. Pfafferoth, J. Resler, S. Rissmann, E. Russo, M. Salim, M. Schrempf, J. Schwenkel, G. Seckmeyer, S. Schubert, M. Sühring, R. V. Tils, L. Vollmer, S. Ward, B. Witha, H. Wurps, J. Zeidler, and S. Raasch. Overview of the PALM model system 6.0. *Geoscientific Model Development*, 13(3):1335–1372, 2020. ISSN 19919603. doi: 10.5194/gmd-13-1335-2020.

BIBLIOGRAPHY

- B. Maronga et al. The Parallelized Large-Eddy Simulation Model (PALM) Version 4.0 for Atmospheric and Oceanic Flows: Model Formulation, Recent Developments, and Future Perspectives. *Geosci. Model Dev.*, 8:2515–2551, 2015.
- L. A. Martínez-Tossas, M. J. Churchfield, and S. Leonardi. Large eddy simulations of the flow past wind turbines: actuator line and disk modeling. *Wind Energy*, 18:1047–1060, 2015.
- L. A. Martínez-Tossas, M. J. Churchfield, and C. Meneveau. Optimal smoothing length scale for Actuator line models of wind turbine blades based on Gaussian body force distribution. *Wind Energ.*, 20:1083–1096, 2017.
- M. Mauder and T. Foken. *Documentation and Instruction Manual of the Eddy-Covariance Software Package TK3 (update)*. University of Bayreuth, 2015.
- A.R. Meyer Forsting, G.R. Pirrung, and N. Ramos-García. A vortex-based tip/smearing correction for the actuator line. *Wind Energ. Sci.*, 4:369–383, 2019. doi: <https://doi.org/10.5194/wes-4-369-2019>.
- A.R. Meyer Forsting, G.R. Pirrung, and N. Ramos-García. Brief communication: A fast vortex-based smearing correction for the actuator line. *Wind Energ. Sci.*, 5:349–353, 2020. doi: <https://doi.org/10.5194/wes-5-349-2020>.
- R. Mikkelsen. *Actuator Disc Methods Applied to Wind Turbines*. PhD thesis, Technical University of Denmark, 2003.
- A. Mittal, K. Sreenivas, L. K. Taylor, and L. Hereth. Improvements to the Actuator Line Modeling for Wind Turbines. *33rd Wind Energy Symposium*, 2015.
- N. Mittelmeier, J. Allin, T. Blodau, D. Trabucchi, G. Steinfeld, A. Rott, and M. Kühn. An analysis of offshore wind farm SCADA measurements to identify key parameters influencing the magnitude of wake effects. *Wind Energy Science*, 2:477–490, 2017.
- C.H. Moeng and J. C. Wyngaard. Spectral analysis of large-eddy simulations of the convective boundary layer. *Journal of the Atmospheric Sciences*, 45:3573–3587, 1988.
- M.M. Mohammadi, H. Olivares-Espinosa, G. P. Navarro Diaz, and S. Ivanell. An actuator sector model for wind power applications: a parametric study. *Wind Energy Science*, 9:1305–1321, 6 2024a. ISSN 2366-7451. doi: 10.5194/wes-9-1305-2024.
- M.M. Mohammadi, W. Chanprasert, H. Olivares-Espinosa, and S. Ivanell. An aeroelastic coupling of an actuator sector model with OpenFAST in atmospheric flows. *Journal of Physics: Conference Series*, 2767:022037, 6 2024b. ISSN 1742-6588. doi: 10.1088/1742-6588/2767/2/022037.
- P. J. Moriarty and A. C. Hansen. AeroDyn Theory Manual. Technical Report NREL/TP-500-36881, National Renewable Energy Laboratory, 2005.
- T. Mücke, D. Kleinhans, and J. Peinke. Atmospheric turbulence and its Influence on the alternating loads on wind turbines. *Wind Energy*, 14:301–316, 2011.
- National Renewable Energy Laboratory. OpenFAST. URL <https://github.com/OpenFAST/openfast>. Last accessed on: 2025-04-29.

- C. W. Oseen. Über Wirbelbewegung in einer reibenden Flüssigkeit. *Arkiv för matematik, astronomi och fysik*, 7:14–21, 1911. doi: ISSN0365-4133.
- S. Paleri, L. Wanner, M. Sühling, A. R. Desai, M. Mauder, and S. Metzger. Impact of surface heterogeneity induced secondary circulations on the atmospheric boundary layer. *Boundary-Layer Meteorology*, 191(1), 2024. ISSN 00068314. doi: 10.1007/s10546-024-00893-7.
- A. Peña, S.-E. Gryning, and C. B. Hasager. Measurements and Modelling of the Wind Speed Profile in the Marine Atmospheric Boundary Layer. *Boundary-Layer Meteorology*, 129:497–495, 2008.
- G. Pirrung, H. A. Madsen, T. Kim, and J. Heinz. A coupled near and far wake model for wind turbine aerodynamics. *Wind Energ.*, 19:2053–2069, 2016. doi: <https://doi.org/10.1002/we.1969>.
- G. Pirrung, V. Riziotis, H. A. Madsen, M. Hansen, and T. Kim. Comparison of a coupled near- and far-wake model with a free-wake vortex code. *Wind Energ. Sci.*, 2:15–33, 2017a. doi: <https://doi.org/10.5194/wes-2-15-2017>.
- G. Pirrung, H. A. Madsen, and S. Schreck. Trailed vorticity modeling for aeroelastic wind turbine simulations in standstill. *Wind Energ. Sci.*, 2:521–532, 2017b. doi: <https://doi.org/10.5194/wes-2-521-2017>.
- D. M. Pitt and D. A. Peters. Theoretical Prediction of Dynamic-Inflow Derivatives. *Vertica*, 5(1), 1981.
- F. Porté-Agel, Y.-T. Wu, H. Lu, and R. J. Conzemius. Large-eddy simulation of atmospheric boundary layer flow through wind turbines and wind farms. *Journal of Wind Engineering and Industrial Aerodynamics*, 99:154–168, 2011.
- J. Powers, J. Klemp, W. Skamarock, C. Davis, J. Dudhia, D. Gill, J. Coen, D. Gochis, R. Ahmadov, S. Peckham, G. Grell, J. Michalakes, S. Trahan, S. Benjamin, C. Alexander, G. Dimego, W. Wang, C. Schwartz, G. Romine, and M. Duda. The Weather Research and Forecasting (WRF) Model: Overview, System Efforts, and Future Directions. *Bulletin of the American Meteorological Society*, 98, 01 2017. doi: 10.1175/BAMS-D-15-00308.1.
- L Prandtl and A. Betz. Vier Abhandlungen zur Hydrodynamik und Aerodynamik. *Göttinger Nachrichten*, pages 88–92, 1927.
- S. Raasch and G. Harbusch. An Analysis of Secondary Circulations and Their Effects Caused by Small-Scale Surface Inhomogeneities Using Large-Eddy Simulation, 2001.
- S. Raasch and M. Schröter. A large-eddy simulation model performing on massively parallel computers, 2001. URL <https://ams.confex.com/ams/pdfpapers/43503.pdf>.
- E.M. Saiki, C.H. Moeng, and P.P. Sullivan. Large-eddy simulation of the stably stratified planetary boundary layer. *Boundary-Layer Meteorology*, 95:1–30, 2000.
- G. Santo, M. Peeters, W. V. Paepegem, and J. Degroote. Effect of rotor–tower interaction, tilt angle, and yawmisalignment on the aeroelasticity of a large horizontal axiswind turbine with composite blades. *Wind Energy*, 23:1578–1595, 2020.

- A. Sathe, J. Mann, T. Barlas, W. A. A. M. Bierbooms, and G. J. W. van Bussel. Influence of atmospheric stability on wind turbine loads. *Wind Energy*, 16:1013–1032, 2013.
- J. Schulz-Stellenfleth, S. Emeis, M. Dörenkämpfer, J. Bange, B. Cañadillas, T. Neumann, J. Schneemann, I. Weber, K. zum Berge, A. Platis, B. Djath, J. Gottschall, L. Vollmer, T. Rausch, M. Barekzai, J. Hammel, G. Steinfeld, and A. Lampert. Coastal impacts on offshore wind farms – a review focussing on the German Bight area. *Meteorologische Zeitschrift*, 31(4):289–315, 2022. ISSN 0941-2948. doi: 10.1127/metz/2022/1109.
- U. Schumann. Subgrid scale model for finite difference simulations of turbulent flows in plane channels and annuli. *Journal of Computational Physics*, 18(4):376–404, 1975. ISSN 0021-9991. doi: [https://doi.org/10.1016/0021-9991\(75\)90093-5](https://doi.org/10.1016/0021-9991(75)90093-5). URL <https://www.sciencedirect.com/science/article/pii/0021999175900935>.
- B.A.M. Sengers. *The benefit of interpretable data-driven methods for wake steering applications*. PhD thesis, Carl von Ossietzky Universität Oldenburg, 2023.
- M. Shives and C. Crawford. Mesh and load distribution requirements for actuator line CFD simulations. *Wind Energy*, 16(8):1183–1196, 2013. doi: <https://doi.org/10.1002/we.1546>. URL <https://onlinelibrary.wiley.com/doi/abs/10.1002/we.1546>.
- M.A. Sprague, S. Ananthan, A. Vijayakumar, and M. Robinson. ExaWind: A multifidelity modeling and simulation environment for wind energy. *Journal of Physics: Conference Series*, 1452, 2019.
- S. Stipa, A. Ajay, and J. Brinkerhoff. The actuator farm model for large eddy simulation (les) of wind-farm-induced atmospheric gravity waves and farm–farm interaction. *Wind Energy Science*, 9(12):2301–2332, 2024. doi: 10.5194/wes-9-2301-2024. URL <https://wes.copernicus.org/articles/9/2301/2024/>.
- R. C. Storey, S. E. Norris, K. A. Stol, and J. E. Cater. Large eddy simulation of dynamically controlled wind turbines in an offshore environment. *Wind Energy*, 16:845–864, 2013.
- R. C. Storey, S. E. Norris, and J. E. Cater. An actuator sector method for efficient transient wind turbine simulation. *Wind Energy*, 18:699–711, 2015.
- R. B. Stull. *An Introduction to Boundary Layer Meteorology*. Kluwer Academic Publishers, 2003.
- J. N. Sørensen and W. Z. Shen. Numerical modelling of wind turbine wakes. *J. Fluid. Eng.-T. ASME*, 124:393–399, 2002.
- J. N. Sørensen, W. Z. Shen, and X. Munduate. Analysis of Wake States by a Full-field Actuator Disc Model. *Wind Energy*, 1:73–88, 1998.
- G. I. Taylor. The spectrum of turbulence. *Proceedings of the Royal Society A*, 164:476–490, 1938.
- N. Troldborg. *Actuator Line Modelling of Wind Turbine Wakes*. PhD thesis, Technical University of Denmark, 2008.
- J. Uhlenbrock. Entwicklung eines Multigrid-Verfahrens zur Lösung elliptischer Differentialgleichungen auf Massivparallelrechnern und sein Einsatz im LES-Modell PALM. Master’s thesis, Institute of Meteorology and Climatology, Leibniz University Hanover, 2001.

- P. Veers, K. Dykes, E. Lantz, S. Barth, C. L. Bottasso, O. Carlson, A. Clifton, J. Green, P. Green, H. Holttinen, D. Laird, V. Lehtomäki, J. K. Lundquist, J. Manwell, M. Marquis, C. Meneveau, P. Moriarty, X. Munduate, M. Muskulus, J. Naughton, L. Pao, J. Paquette, J. Peinke, A. Robertson, J. Sanz Rodrigo, A. M. Sempreviva, J. C. Smith, A. Tuohy, and R. Wisser. Grand challenges in the science of wind energy. *Science*, 366(6464):eaau2027, 2019. doi: 10.1126/science.aau2027. URL <https://www.science.org/doi/abs/10.1126/science.aau2027>.
- L. Vera-Tudela and M. Kühn. Analysing wind turbine fatigue load prediction: The impact of wind farm flow conditions. *Renewable Energy*, 107:352–360, 2017.
- A. Vitsas and J. Meyers. Multiscale aeroelastic simulations of large wind farms in the atmospheric boundary layer. *Journal of Physics: Conference Series*, 753(082020), 2016.
- J. Vogel, A. Afshari, G. Chockalingam, and S. Stadler. Evaluation of a novel WRF/PALM-4U coupling scheme incorporating a roughness-corrected surface layer representation. *Urban Climate*, 46:101311, 2022. ISSN 2212-0955. doi: <https://doi.org/10.1016/j.uclim.2022.101311>. URL <https://www.sciencedirect.com/science/article/pii/S2212095522002292>.
- L. Vollmer, G. Steinfeld, D. Heinemann, and M. Kühn. Estimating the wake deflection downstream of a wind turbine in different atmospheric stabilities: an LES study. *Wind Energy Science*, 1: 129–141, 2016.
- R. Wagner et al. Rotor equivalent wind speed for power curve measurement – comparative exercise for IEA Wind Annex 32. *Journal of Physics: Conference Series*, 524, 2014.
- S. Wharton and J. K. Lundquist. Atmospheric stability affects wind turbine power collection. *Environmental Research Letters*, 7(014005), 2012.
- L.J. Wicker and W.C. Skamarock. Time-Splitting Methods for Elastic Models Using Forward Time Schemes. *Monthly Weather Review*, 130(8):2088–2097, 2002.
- J. M. Wilczak, S. P. Oncley, and S. A. Stage. Sonic Anemometer Tilt Correction Algorithms. *Boundary-Layer Meteorology*, 99:127–150, 2001.
- J.H. Williamson. Low-storage Runge-Kutta schemes. *Journal of Computational Physics*, 35:48–56, 1980.
- Deutsche WindGuard. Status des Offshore-Windenergieausbaus in Deutschland - Jahr 2024. Technical report, Deutsche WindGuard, 2025a. URL https://www.windguard.de/jahr-2024.html?file=files/cto_layout/img/unternehmen/windenergiestatistik/2024/Jahr/Status%20des%20offshore-Windenergieausbaus_Jahr%202024.pdf. Last accessed on: 2025-04-24.
- Deutsche WindGuard. Status des Windenergieausbaus an Land in Deutschland - Jahr 2024. Technical report, Deutsche WindGuard, 2025b. URL https://www.windguard.de/jahr-2024.html?file=files/cto_layout/img/unternehmen/windenergiestatistik/2024/Jahr/Status%20des%20Windenergieausbaus%20an%20Land_Jahr%202024.pdf. Last accessed on: 2025-04-24.
- B. Witha, G. Steinfeld, and D. Heinemann. High-Resolution Offshore Wake Simulations with the LES Model PALM. *Hölling M., Peinke J., Ivanell S. (eds) Wind Energy - Impact of Turbulence*, 2, 2014. Springer, Berlin, Heidelberg.

BIBLIOGRAPHY

- B. Witha, G. Steinfeld, and D. Heinemann. Advanced turbine parameterizations in offshore les wake simulations. In *Extended Abstracts of the 6th International Symposium on Computational Wind Engineering (CWE) 2014*, Hamburg, Germany, 06 2014b.
- A. A. Wyszogrodzki, S. Miao, and F.n Chen. Evaluation of the coupling between mesoscale-WRF and LES-EULAG models for simulating fine-scale urban dispersion. *Atmospheric Research*, 118: 324–345, 2012. ISSN 0169-8095. doi: <https://doi.org/10.1016/j.atmosres.2012.07.023>. URL <https://www.sciencedirect.com/science/article/pii/S016980951200261X>.
- X. Yang, K.B. Howard, M. Guala, and F. Sotiropoulos. Effects of a three-dimensional hill on the wake characteristics of a model wind turbine. *Physics of Fluids*, 27, 2015. doi: <https://doi.org/10.1063/1.4907685>.
- W. Zhang, X. I. A. Yang, J. Li, and M. Wan. Large-eddy simulation and modeling on the evolution of large-scale secondary vortices in turbulent boundary layer. *Boundary-Layer Meteorology*, 191(3), 2025. ISSN 00068314. doi: 10.1007/s10546-025-00904-1.
- Y. Zhang, M. Cheng, and Z. Chen. Load mitigation of unbalanced wind turbines using PI-R individual pitch control. *IET Renewable Power Generation*, 9(3):262–271, 2015.

Publication list

Peer-reviewed journal articles

- Krüger, S., Steinfeld, G., Kraft, M., & Lukassen, L. J. (2022). Validation of a coupled atmospheric-aeroelastic model system for wind turbine power and load calculations. *Wind Energy Science*, 7(1), 323–344. <https://doi.org/10.5194/wes-7-323-2022>
- Doubrawa, P., Quon, E. W., Martinez-Tossas, L. A., Shaler, K., Debnath, M., Hamilton, N., Herges, T. G., Maniaci, D., Kelley, C. L., Hsieh, A. S., Blaylock, M. L., van der Laan, P., Andersen, S. J., Krueger, S., Cathelain, M., Schlez, W., Jonkman, J., Branlard, E., Steinfeld, G., Schmidt, S., Blondel, F., Lukassen, L. J., & Moriarty, P. (2020). Multimodel validation of single wakes in neutral and stratified atmospheric conditions. *Wind Energy*, 23(11), 2027-2055. <https://doi.org/10.1002/we.2543>

Conference contributions

- Steinbrück, S., Eilers, T., Vollmer, L., Avila, K., & Steinfeld, G. (2024). Improvement of the PALM-FAST coupling for heterogeneous wind fields. In *PALM Model Conference*, Offenbach, Germany, 17-20 September 2024 (online oral presentation).
- Krüger, S., Steinfeld, G., & Bromm, M. (2018). Rechenzeitoptimierte Kopplung von LES und aeroelastischem Code für Studien des atmosphärischen Einflusses auf das WEA-Verhalten. In *5. Fachtagung Energiemeteorologie*, Goslar, Germany, 5–7 Juni 2018 (oral presentation).
- Krüger, S., Witha, B., & Heinemann, D. (2017). Investigation of the Development of Internal Boundary Layers by Means of Large-Eddy Simulation. In *EMS 2017*, Dublin, Ireland, 4–8 September 2017 (oral presentation).

Acknowledgements

I would like to acknowledge my supervisor, Prof. Dr. Kerstin Avila, for her support and guidance during the last years. I also thank Adj. Prof. Dr. Richard Stevens from the University of Twente for agreeing to review my thesis and for his role as a member of the examination committee.

The work presented in this thesis has been carried out within the national research projects “Heterogener Hochleistungsrechner für windenergierelevante Meteorologie- und Strömungsberechnungen” (WIMS-Cluster, FKZ 0324005) and “X-Wakes” (FKZ 03EE3008 A-G), both funded by the Federal Ministry for Economic Affairs and Climate Action (BMWK), as well as within the project “ventus efficiens” (ZN3024) funded by the Ministry for Science and Culture of Lower Saxony. Computing resources were partly provided by the National High Performance Computing (NHR). I am also grateful to eno energy for providing access to measurement and design data of a commercial turbine, which was instrumental in validating my simulations.

I would like to express my gratitude to all the members of EnMet and ForWind Oldenburg for fostering such a friendly and supportive environment. I would like to thank my colleagues at the Fraunhofer Institute for Wind Energy Systems (IWES) for providing a supportive atmosphere, as well as the time and space needed to complete my work during the final phase. I also thank the Fraunhofer Institute for Wind Energy Systems (IWES) for their financial support during this crucial stage.

My sincere appreciation goes to Dr. Gerald Steinfeld for his invaluable support throughout my work on this thesis. His expertise in LES modeling and guidance were instrumental to my research. I am also grateful for the opportunity to work in the collaborative environment of Gerald’s group, where our many discussions and your constructive feedback significantly contributed to the success of this thesis. Additionally, I wish to express my gratitude to Lukas Vollmer for his guidance and feedback during the final phase of my work at IWES.

I would like to acknowledge the following (former) colleagues from ForWind and IWES for all their help and engaging discussions over the past years: Hauke Wurps, Wilke Trei, Johanna Borowski, Luuk Sengers, Martin Dörenkämper, Bernhard Stoevesandt, Paul Hulsmann, Martin Kraft, Anna Mehrens, Bruno Schyska, Marc Bromm, Anantha Kidambi, Renko Buhr, Björn Witha, Dagmar Battermann, Frauke Haunhorst, Irene Meints and Agnes Seeger.

Besonderer Dank gilt meiner Familie und allen Freund*innen, die mich während der Zeit unterstützt und motiviert haben.

Curriculum Vitae

Personal Information

Name: Sonja Steinbrück, née Krüger
Date of Birth: 13.05.1986
Place of Birth: Bielefeld

Education

10/2014 – 12/2016 M.Sc. Engineering Physics
Carl von Ossietzky Universität Oldenburg, Oldenburg

10/2011 – 02/2015 B.Eng. Engineering Physics
Carl von Ossietzky Universität Oldenburg, Oldenburg

09/2006 – 05/2009 Study of Aerospace Engineering
Universität der Bundeswehr München, München

1996 – 2005 High School Diploma (Abitur)
Städtisches Gymnasium am Waldhof, Bielefeld

Scientific experience

11/2022 – now Research Associate
Fraunhofer Institute for Wind Energy Systems IWES, Oldenburg

01/2017 – 10/2022 Research Associate
Energiemeteorologie, ForWind, Oldenburg

08/2015 – 12/2016 Student Research Assistant
Energiemeteorologie, ForWind, Oldenburg